UC San Diego

UC San Diego Electronic Theses and Dissertations

Title

Separation, process and detection of biomolecules using silicon-based optical nanostructures

Permalink

https://escholarship.org/uc/item/7w21h025

Author

Chen, Michelle Ying-Hsuan

Publication Date

2011

Peer reviewed|Thesis/dissertation

eScholarship.org Powered by the California Digital Library
University of California

UNIVERSITY OF CALIFORNIA, SAN DIEGO

SEPARATION, PROCESS AND DETECTION OF BIOMOLECULES USING SILICON-BASED OPTICAL NANOSTRUCTURES

A dissertation submitted in partial satisfaction of the requirements for the degree Doctor of Philosophy

in

Bioengineering

by

Michelle Ying-Hsuan Chen

Committee in charge:

Professor Michael J. Sailor, Chair
Professor Michael J. Heller, Co-Chair
Professor Sadik C. Esener
Professor Xiaohua Huang
Professor Yu-Hwa Lo

2011

Copyright

Michelle Ying-Hsuan Chen, 2011

All rights reserved

The dissertation of Michelle Ying-Hsuan Chen is approved, and it is acceptable in quality and form for publication on microfilm and electronically:

Co-chair

Chair

University of California, San Diego

2011

DEDICATION

To my grandmother

TABLE OF CONTENTS

LIST OF FIGURES

CHAPTER SIX

CHAPTER SEVEN

LIST OF TABLES

ACKNOWLEDGEMENTS

First, I would like to express my sincere gratitude to my advisor, Prof. Michael Sailor, for giving me the opportunity to be a part of "Sailor Group", teaching me how to be a scientist, and converting me into another (MAppleC) user. Thank you for all your encouragement, support, patience, and unlimited supplies of M&Ms. I truly value this experience and everything I have learned from you.

Thanks to my committee members who offered their time and advice throughout these years: Prof. Michael Heller, Prof. Sadik Esener, Prof. Xiaohua Huang, and Prof. Yu-Hwa Lo.

To Dr. Shawn Meade, thank you for being my mentor and getting me started on my first few projects.

I also would like to thank the original main office crew: Manny Orosco, Brian King, Shawn Meade and Luo Gu. It was really fun sitting next to all of you. I will always remember the dirty gym bag from Brian with the odor that counterbalanced with the flowery perfume from Manny, the subway wrapped sugar sandwich from Shawn, and the garlic fries from Red Robin that Manny and I used to eat just after we had worked out. Also, I want to thank my human Wikipedia, Luo, who always gives me an answer faster than I can type my questions into Google.

I also had the opportunity to work with some amazing Postdocs, Matt Kinsella, Jenny Andrew, Tim Kelly, and Wei Jin. Thank you for your valuable suggestions and keeping me on track for the last few months.

To the international visiting scholars/professors, Gordon Miskelly, Frédérique Cunin, Stephanie Pace, Emilie Secret, Beniamino, Matrix, Michela, Linda, and Fengxia: I am very happy that I got to know each of you. To Emilie and Frédérique, thank you for showing me around and taking care of me in France.

To Maggie and Vinh: thank you for pulling through for the last few months. Without your hard work, I will probably still be in lab somewhere.

To all the members in Sailor lab, thank you for your moral support and pep talks: ChiaChen, Adrian, Sara, Anne, Joel, Ji-Ho, Zhengtao, Ling, Danny, Jen and all other current and former group members. Especially, ChiaChen and Liz Wu, thank you for all the coffee cart runs and fun/encouraging conversations.

To my friends, Alice, Lila, Hyun, Anohki, and Saskia, thank you for being there for me throughout this whole process. I am very fortunate to have known each of you.

I especially would like to thank my family: Kenny, James, mom and dad for their constant support and making sure I am sane and healthy. Lastly, I would like to thank George, for his support, love, and patience. I could not have done this without you.

Chapters two, three, four, five, six and seven are, in part or in full, reprints of the following publications:

- **Chen, M.Y.**; Meade, S.O.; Sailor, M.J. "Preparation and Analysis of Porous Silicon Multilayers for Spectral Encoding Applications", *Physica Status Solidi (c)*. 2009, 6(7), 1610-1614

- **Chen, M. Y.**; Sciacca, B.; Miskelly, G. M.; Sailor, M. J. "Temperature and Structure Dependent Thermal Oxidation of pSi" Manuscript in preparation

- Meade, S.O.; **Chen, M. Y**.; Sailor, M. J.; Miskelly, G. M. "Multiplexed DNA Detection Using Spectrally Encoded Porous SiO_2 Photonic Crystal Particles", *Anal. Chem*. 2009, 81,2618-2625

- **Chen, M. Y.**; Diep, V.; Wu, C.; Secret, E.; Cunin, F.; Andrew, J.; Sailor, M. J. "Multistage Insulin Release using Double-Layer Mesoporous Silica Structures" Manuscript in preparation

- **Chen, M. Y.**; Sailor, M. J. "Charge-Gated Transport of Proteins in Nanostructured Optical Films of Mesoporous Silica", *Anal. Chem.,* Submitted

- **Chen, M. Y.**; Klunk, M.; Diep, V.; Sailor, M. J. "Electric Field Assisted Protein Transport, Capture and Interferometric Sensing in Carbonized Porous Silicon Films", *Adv. Mater.*, Accepted

The author of this dissertation was one of the primary authors or co-author on all publications.

VITA

EDUCATION

Sept. 2011	Ph.D., Bioengineering, University of California, San Diego
Dec. 2007	M.S., Bioengineering, University of California, San Diego
Dec. 2004	B.S., Information and Computer Science; Minors: Business Management and Biomedical Engineering, University of California, Irvine

PUBLICATIONS

Chen, M. Y.; Klunk, M.; Diep, V.; Sailor, M. J. "Electric Field Assisted Protein Transport, Capture and Interferometric Sensing in Carbonized Porous Silicon Films" *Adv. Mater.,* Accepted

Chen, M. Y.; Diep, V.; Wu, C.; Secret, E.; Cunin, F.; Andrew, J.; Sailor, M. J. "Multistage Insulin Release using Double-Layer Mesoporous Silica Structures" Manuscript in preparation

Wu, C.; **Chen, M.Y.**; Cunin, F.; Sailor, M. J. "Partition Coefficient Measurement Using Surface Modified Porous Silicon Nanostructure" *Langmuir*, Manuscirpt in preparation

Chen, M. Y.; Sciacca, B.; Miskelly, G. M.; Sailor, M. J. "Temperature and Structure Dependent Thermal Oxidation of pSi" Manuscript in preparation

Chen, M. Y.; Sailor, M. J. "Charge-Gated Transport of Proteins in Nanostructured Optical Films of Mesoporous Silica", *Anal. Chem.,* Submitted

Andrew, J. S.; Anglin, E. J.; Wu, E. C.; **Chen, M. Y.**; Cheng, L; Freeman, W. R.; Sailor, M. J. "Sustained Release of a Monoclonal Antibody from Electrochemically Prepared Mesoporous Silicon Oxide", *Adv. Funct. Mater*. 2010, xx,1-8

Meade, S.O.; **Chen, M. Y**.; Sailor, M. J.; Miskelly, G. M. "Multiplexed DNA Detection Using Spectrally Encoded Porous SiO_2 Photonic Crystal Particles", *Anal. Chem*. 2009, 81,2618-2625

Chen, M.Y.; Meade, S.O.; Sailor, M.J. "Preparation and Analysis of Porous Silicon Multilayers for Spectral Encoding Applications", *Physica Status Solidi (c)*. 2009, 6(7), 1610-1614

ABSTRACT OF THE DISSERTATION

SEPARATION, PROCESS AND DETECTION OF BIOMOLECULES USING SILICON-BASED OPTICAL NANOSTRUCUTURES

by

Michelle Ying-Hsuan Chen

Doctor of Philosophy in Bioengineering
University of California, San Diego, 2011

Professor Michael J. Sailor, Chair
Professor Michael J. Heller, Co-chair

Advancements in the field of optical sensors have resulted in an innovative class of microoptical sensors exhibiting detection capability comparable to those sophisticated analytical laboratory instrumentations. An emerging trend is to integrate these optical sensors/detecting methods into analytical tools with the ability to perform multifunctional tasks (i.e sample filtration, detection, and signal processing etc.) all in one platform. Porous silicon possesses many fascinating features making it an attractive candidate as a spectrally encoded material that is suitable as an identifier/barcode for multi-analyte bioassays and a spatially controlled structure that is

applicable as a chromatography matrix for biomolecule separation. Its high surface to volume ratio and readily tailored surface chemistry also provide additional control for enhancing selectivity. Combining its optical and physical properties together with tailored surface moieties, porous silicon material can be treated as a multifunctional material allowing simultaneous separation and detection, capable of the multiplexed, low-level biodetection necessary to accommodate complex biological mixtures such as urine, whole blood, or serum used for disease diagnosis.

This thesis begins with an overview on current separation techniques and progress in the field of optical sensors and nanomaterials. The second half of the introduction discusses recent development in porous silicon material with the focus on biosensing and molecular filtration applications.

The objective of this thesis is to explore porous silicon as a multifunctional material with the ability to separate, process, and detect biomolecules at low concentration and in real-time with minimal sample preparation. Interrogation of porous silicon material as a multifunctional nanostructure involved three major aspects: 1) manipulation of its optical and spectral information for encoding and signal processing applications, 2) examination of the effect of its physical properties on molecular transport within its porous structure, 3) investigation of analyte-pore surface interaction for enhanced selectivity or better separation based on analyte surface moieties. The last chapter of this thesis provides an example of exploiting porous silicon as a multifunctional matrix that is capable of capturing and concentrating analyte while processing the signal, providing a new strategy for bioanalytics.

CHAPTER ONE

INTRODUCTION TO SEPARATION AND DETECTION TECHNIQUES FOR BIOMOLECULES

1 Introduction To Separation and Detection Techniques for Biomolecules

1.1 Introduction and Motivation

The passage of individual molecules through nano-sized pores is central to many biological processes. However, our understanding of such filtration processes is not as complete as the ubiquity of the phenomena. Standard laboratory techniques for characterizing and separating biomolecules, such as chromatography and gel electrophoresis do not help elucidate these proceses. The main drawbacks of the current laboratory techniques for characterizing and separating biomolecules are analysis time and cost, and more importantly, the lack of molecular information on the how this biological process occurs.[1] Thus a fundamental understanding of the interfacial interaction between biomolecules and nano-sized pores and transport behavior of biomolecules, as well as quantitative descriptions of processing characteristics, remain active areas of research. One of the main obstacles hindering the understanding of molecule-nanostructure interactions was the lack of analytical tools available to elucidate details of these interactions. Recent advancements in nanotechnology have lead to the discovery of numerous exciting new analytical tools including nanopores,[2, 3] nanofluidics,[4] and nanoelectrodes,[5] that may address to the shortcomings associated with current experimental methods.[6-8] In addition to the discovery of new nano-materials, advances in biosensors allow more rapid, sensitive, and selective detections for studying and characterizing biomolecules.[9-11] Miniaturizing and combining these components into a single platform would enable studies in a more relevant size scale for

complex biological samples, providing many attractive benefits such as sample volume reduction, portability, and enhanced throughput. These platforms have great potentials in a variety of areas including point-of-care diagnostics, biomolecular analysis and characterization, drug discovery, and environmental monitoring.[12, 13]

Porous silicon nanostructures attract much interest because of their unique properties including controllable pore dimensions, tunable optical and photoluminescence spectra, and chemically modifiable surfaces. These unique features make porous silicon an attractive candidate, offering new strategies for designing novel analytical platforms. Chemical, physical, and optical properties of porous silicon have been extensively studied and used for many chemical and biological applications including delivery of drugs,[14-18] separation of biomolecules,[19, 20] and detection of toxins,[21] explosives,[22] enzyme activity,[23, 24] and proteins[25].

One of the most promising applications is the use of the spectral and structural properties of porous silicon material to identify and study molecules of interest. For instance, porous silicon has been harnessed as a spectrally encoded identifier for multi-analyte bioassays[26] as well as a structurally controlled nanostucture for biomolecular separation[27] and characterization[19, 28]. However, little data have been presented using porous silicon to study molecule-nanosturcture interaction and molecular transport by combining the separator and sensor into a single material. The concept of using porous silicon as a multifunctional material that can perform separation, characterization, and identification at the material level is a relatively unexplored area. This approach provides a new design of a miniaturized system that can perform multiplexed detection and separation with enhanced selectivity in a biologically relevant length scale.

Previous work in porous silicon leading to current knowledge will be discussed. Current analytical techniques for biomolecular identification, separation, and detection will also be summarized in this chapter.

1.2 Characterization and Separation Techniques for Biomolecules

Chromatography and gel electrophoresis have been the standard techniques for characterizing biomolecules. However, the characterization of these molecules is usually performed using universal calibration curves or standards overlooking the interaction between the sieving material and the analyte. Combing multiple components (separating columns and dectection systems) into a single platform is one of the many approaches during recent years for more accurate and reliable measurements.[29, 30] New separation materials have also been investigated to improve separation and characterization of biomolecules.[31] Another emerging area for molecular sieving and detection is nanotechnology; the interest in nanoscale materials stems from the fact that their versatile properties (optical, chemical, mechanical, etc.) can be tailored based on their size, composition, and structure orders for a wide range of applications such as drug delivery, in vitro diagnostics, and tissue engineering.[32] As pointed out in the previous section, the interaction at the filter-molecule interface demands careful scientific study for more accurate characterization of the molecules and improved selectivity of molecular separation. The main advantage of these nano-materials is their characteristic dimensions comparable to biomolecules allowing a more realistic representation of the membrane phenomena and biological processes. The

small dimensions also reduce sample requirements and improve cost efficiency. The objective of following subsections is to provide a brief overview of currently available biomolecular separation and characterization techniques.

1.2.1 Separation Principles and Techniques for Liquid Chromatography

Chromatography is a technique commonly used for purifying or analyzing a complex mixture of analytes. Figure 1.1 is an example of two different column chromatographic methods, size exclusion and ion exchange chromatography. In addition to the column chromatography, planar chromatography such as paper chromatography, thin-layer chromatography, and different types of electrophoresis (more details will be discussed in the following section) have been studied for bioanalysis and biomolecular separation. The main separation principle of these approaches involves a difference in the equilibrium distribution of a solute between two phases: a stationary phase, where the solute interact with the column/packing material and are immobilized in this phase; and, a mobile phase, where the solvent moves with the samples being extracted or analyzed. Samples are then characterized based on differential migration behaviors in their apparent velocity, residence time, or volume of mobile phase.[33]

Different forces or physicochemical phenomena such as adsorption, ion exchange, extraction, and exclusion, have been studied and exploited to discriminate analytes more selectively and effectively. Based on the mode of retention in the

stationary phase (physicochemical phenomenon), or the type of bed (enclosed or open-bed), chromatography can be classified as follows:[34]

- Column chromatography
- Paper chromatography
- Thin-layer chromatography
- High pressure liquid chromatography
- Ion-exchange chromatography
- Gel-filtration chromatography
- Supercritical fluid chromatography

The choice of the type of bed in combination with eluting solvent for the mobile phase, and discriminating adsorbent for the stationary phase is crucial in the design of more effective chromatographic system. Over the years, materials such as silica gel,[35] alumina,[36] calcium carbonate,[34] and cellulose[37] have been studied and used as adsorbents to improve the system for greater selectivity. In the past decade, porous monolithic materials have received a comprehensive attention as a potential alternative to apply chromatographic separation in micro-scale for applications such as capillary liquid chromatography, capillary electrochromatography, and microfluidic devices. These new materials have been shown to provide better stability, resolution, and sensitivity compared to conventional materials.[31] More recently, scientists have begun to seek new designs of chromatographic separation systems. The following outlines some of current approaches for attaining better discriminating power and maximum information with shorter experimental time and reduced sample requirement.

Current designs focus on the speed of analysis, convenience, sample volume requirement, efficiency, and total run time in addition to the accuracy of the system. In particular, multidimensional chromatographic techniques have been developed for the purpose of enhancing resolving power and increasing efficiency by adapting various separation mechanisms into a single system.[38] Alternatively, a number of chromatographic systems have continued in the area of integrating more sensitive detection systems (i.e. mass spectroscopy and optical detectors) in conjunction with biomolecule characterization and separations to not only improve accuracy but also enable the study of protein interactions.[29] Both approaches have been reported to provide attractive advantages including improved selectivity and efficiency, and less time-consuming analysis over the conventional chromatographic systems.

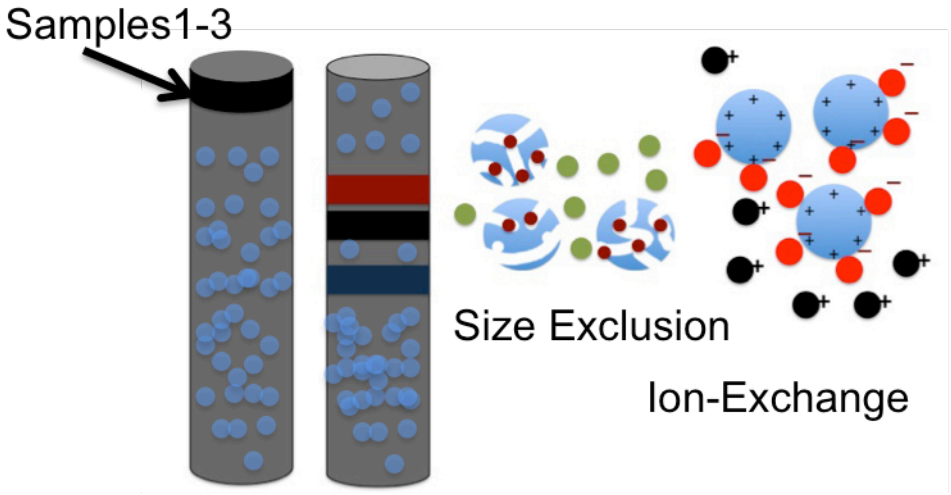

Figure 1.1 Size exclusion and ion exchange chromatography.

1.2.2 Electrophoresis

Electrophoretic methods have been used to separate samples based on their charge-to-mass ratios with an applied electric field. These techniques are routinely used for the characterization and separation of macromolecules such as proteins, nucleic acids and polysaccharides. Electrophoresis was first discovered by a Swedish chemist named Arne Tiselius in the 1930s for the study of serum proteins.[34] Over the next few decades, different types of electrophoresis have been developed including isoelectric focusing,[39] sodium dodecyl sulfate polyacrylamide gel electrophoresis,[40] and free-zone capillary electrophoreses[41]. Similar to chromatography, electrophoresis utilizes physiochemical phenomena to achieve separation. The only difference between the two methods is the type of underlying process (equilibrium or rate) used for separation. For electrophoresis, molecules are segregated based on the differences in their kinetic properties under the influence of an electric field, whereas for most chromatographic methods, molecules are separated based on analyte distribution in two phases after an equilibrium has been reached.

A growing trend in recent years to improve efficiency is miniaturizing existing systems. An example is the capillary electrophoresis that has been demonstrated with smaller volume requirement, non-perturbing sample preparation, and shorter analysis time compared to traditional electrophoresis methods.[42] Coupling capillary electrophoresis to mass spectrometer or into a microfluidic system is one of many promising strategies that is currently under investigation bringing new prospects to the field of bioanalysis and separation.

1.2.3 Nanopores/Nanochannels

An emerging area is the field of nanoscale materials, such as nanopores,[2, 43] nanochannels,[44] and nanotubes,[45] for bioanalysis. The interest in nanotechnology stems from its comparable scale to biological structures, giving rise to many attractive benefits including reduced sample requirements, enhanced selectivity, and increased throughput. These nanoscale pores present new strategies to study biological processes with structures that can be fine-tuned and surfaces that can be modified to mimic biological processes. One of the most commonly studied process is the behavior of membrane proteins and ionic channels.[46, 47] In fact, the first nanopore experiment was inspired by nature, where a membrane protein, α-haemolysin, was used to perform a single molecule transport study.[48] Since then, man-made polymeric,[3] inorganic,[3, 49] and composite[50] nanoscaled pores have been constructed for applications in biosensors,[47, 51] nanofluidic devices,[4] molecular filtration,[52] and many other areas. Now, these artificial nanopores/nanochannels have attracted more attention compared to their biological counterparts, offering better stability and greater flexibility in terms of tunable surface properties, and controllable size and shapes. While this is still an emerging field, recent development of nanopores/nanochannals has already shown exciting opportunities for further enriching our understanding of the molecular filtrating phenomena.

1.2.4 Summary

Until now, electrophoresis and chromatography are still the standard experimental tools for molecular separation and characterization. The analysis, or

estimation rather, involves using a standard neglecting the interaction between the sieving material and the analyte. Samples also undergo stringent preparation steps to achieve necessary resolution, consuming additional time and resources. In recent years, efforts have been focused on alternative strategies involving miniaturizing and combining existing methods to provide more accurate estimates with improved time and cost efficiency. As a result, new separation materials have emerged, and an important theme is the application of nanotechnology to both the molecular sieving and detection processes. The interest in nanoscale materials stems from the fact that their properties (optical, chemical, mechanical, etc.) can be tailored based on size, composition, and structure, and that the characteristic dimensions of nanomaterials are comparable to biomolecules—allowing more realistic representation of natural membrane phenomena. Finally, Table 1.1 displays the different separation techniques and their sample and time requirement. It is interesting to point out that nanopores have been reported with single-molecule sensitivity requiring very short analysis time. Although abiotic nanopore is a relatively young field, it has demonstrated promising attributes that can address some of the drawbacks present in traditional techniques and can provide more detailed, microscopic pictures of molecule-nanostructure interactions.

Table 1.1 Comparisons for separation techniques.

Method	Separation Basis	Sample Requirement	Analysis Time	Reference
Chromatography				
Size-Exclusion	Mol. Weight, Size	mg-g	Good	[34]
Ion Exchange	Ions	mg-g	Good	[34]
Thin-Layer	Physical Interaction	mg-g	Good	[34]
HPLC	Physiochemical	µg	Fast	[53]
Electrophoresis				
Capillary	Physiochemical	ng-µg	Fast	[53]
2D Electrophoresis	Mol. Weight	µg-mg	Good	[54]
Nanomaterials				
Nanopores/Nanochannel	Size, Charge	Single molecule	Very Fast	[2, 55]

1.3 Fundamentals of Biomolecule Identification and Detection

Recent advancements in biosensors have led to more sensitive techniques and analysis tools that are applicable not only to biomedical research but also to a wide range of fields such as healthcare, pharmaceuticals, environmental monitoring, homeland security, and the battlefield.[1, 56, 57] Current designs of these biosensors focus on reducing sample requirement and performing multiplexed detection with high sensitivity and selectivity. Label-free biosensors have presented some desirable features to help attain required sensitivity and selectivity with less sample requirement and perturbation. Some have also shown potentials in multiplexed identification of biomolecules and real-time detection of biological processes. Furthermore, novel strategies using nanomaterials such as gold nanoparticles and nanorods have also been explored to help with these efforts. One of the most appealing benefits is the free-standing nanomaterials with enhanced surface to volume ratio that can eliminate the need for on-chip sensing, facilitating parallel, multiplexed optical detection. With advancements in biomolecular identification, an emerging trend is to combine all the features of a sensor into a single, multiplexed system with the ability to concentrate, separate and analyze complex biological fluids. All these features have led to continued efforts in multiple disciplines and have made biosensing a highly complex field that is at the interface between biology, chemistry, materials science, physics and analytical chemistry.

1.3.1 Types of Biosensors

The two main aspects of biosensor designs involve a bio-recognition element that is specific to the target molecule and a transducer that transforms analyte interaction with the senor into quantifiable signals.[58] The choice of the bio-recognition element depends on the target molecule, and is usually in the form of antibody-antigen pairs for proteins or complmentary oligonucleotides for DNA. Biosensors can be grouped into different categories based on the how the signals are transuded. As displayed in Figure 1.2, transducers are divided into three categories: electrical and electrochemical, optical, and mass-sensitive transducers.[1] As described by the names, signals are transduced based on potential, optical, or mass variation during the sensing event. For the scope of the dissertation, only optical sensors will be discussed.

1.3.2 Optical Biosensors

Optical biosensors, as defined by its name, employ optical principles for transducing a biochemical interaction into appropriate output signal. The light characteristics of the transducer (i.e., intensity, phase, polarization, etc.) modulate in response to the biomolecular interaction on the sensor surface. This optical change can be detected in a number of ways including changes in absorption, fluorescence, luminescence, or refractive index.[59] Figure 1.3 summarizes the optical sensing event described above.

As shown in Figure 1.2, optical label-free transduction methods can be grouped into two categories depending on the detection protocol: fluorescence-based and label-

free. For fluorescence-based biosensors, either target or recognition molecules are conjugated with fluorescent molecules. The signal is measured directed upon a biomolecular interaction. This method faces many challenges such as tedious labeling procedures, interference with the function of the biomolecule, and signal bias due to difficulties in precise control of the number of dyes on each molecule.[59] For label-free biosensors, as the name indicates, detection is performed without the need for extraneous labeling. The signal is measured directly based on the change in the refractive index of the optical medium. The benefit of label-free biosensors is that they allow detection without significantly altering the capture probes or the analyte, providing binding parameters (equilibrium and kinetic binding constants) that are more representative of the native interactions. This type of detection is more sensitive and relatively easy and cheap to perform. It allows in situ quantitative and kinetic measurements for molecular interactions in real-time. Another attractive characteristic is that only a diminutive sample volume (femtoliter to nanoliter) is required, as illustrated in Table 1.2.[56]

Label-free optical sensors are classified further into different categories based on the type of effect (i.e. phase change, coupling effects between waveguide structures, surface plasmon resonance (SPR), grating couplers, interferometry, etc.) generated as a result of the receptor-analyte interaction in the light beam.[59] The basic principle for the effects is similar except for the evanescent field generated in some cases. Here, label-free optical sensors are divided into two groups based on the above distinction.

The two group are optical interferometric methods (such as interferometers[60] and grating couplers[61-63]) and surface plasmon resonance (SPR) methods (such as prism

based[64] (Figure 1.4) and wavelength modulated SPRs[65]). Both methods measure the change in the refractive index in the optical medium with the exception that SPR methods generates an optical phenomenon with a charge density oscillation at the interface of a metal and a dielectric (Figure 1.4). To date, SPR is relatively mature and some have already been commercialized. Although SPR methods have shown good detection limit (Table 1.2) that satisfies most research requirements, there are two limitations that have yet to be overcome: (1) penetration depth (~100 nm) of the evanescent field and (2) single detector configuration. Thus, large target molecules are very difficult to be detected and most SPR sensors are restricted to one analyte per measurement.[56] A potential solution comes from the idea of utilizing plasmonic nanomaterials. Metal nanotstructures with engineered shapes behave like optical antennae by concentrating electromagnetic fields when SPR are excited. Different designs of these metal nanostructures have been shown with enhanced SPR fields, such as nanohole arrarys,[66, 67] nanospheres[68] and bowtie antennae.[69] The underlying concept is similar to the earlier method, where the SPR wavelength and intensity are dependent on the dielectric properties of the surrounding, limited to the local evanescent field at the metal surface. Free-standing metal nanostructures with these properties can enhance surface to volume ratio and eliminate the need for on-chip sensing, facilitating parallel, multiplexed optical detection. The main challenge now is integrating the different elements (i.e. detector, processor, filters, etc.) into a single platform for multiplexed biosensing.

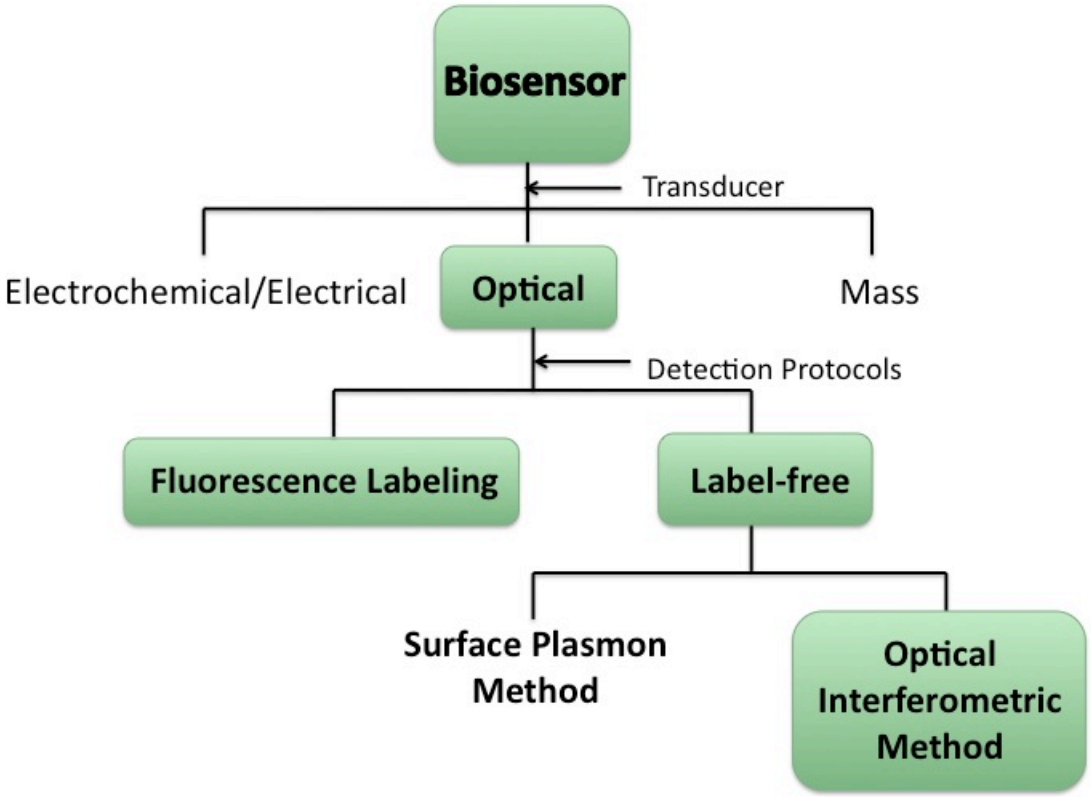

Figure 1.2 Types of biosensors.

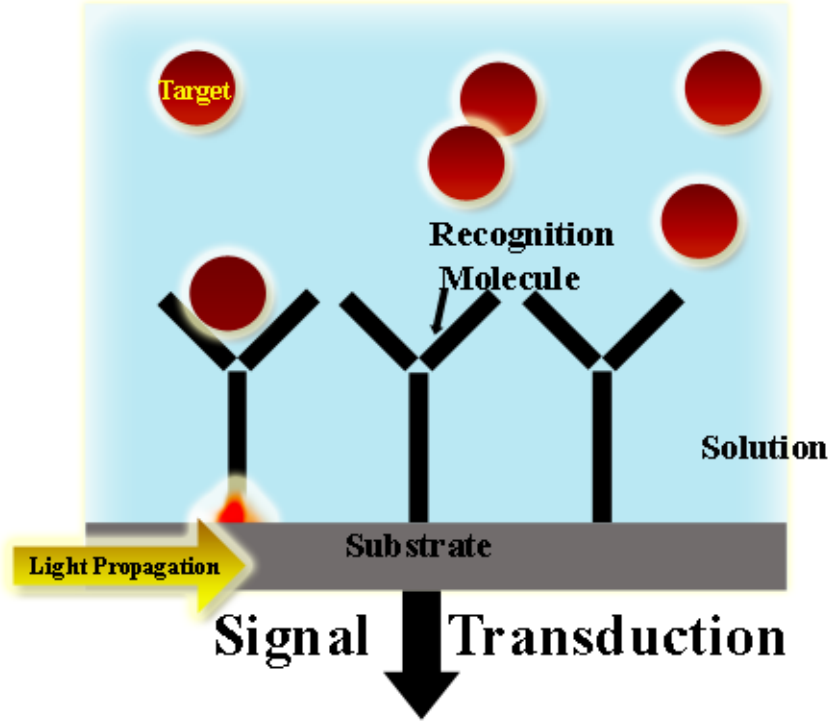

Figure 1.3 Detection principle of label-free optical sensors.

Table 1.2 Examples of label-free optical sensors.

Optical Structures	Detection Principles	Analyte	Limit of Detection	References
BIAcore 2000 SPR	Surface Plasmon resonance	Protein	60 pg/mL, 1-5 pg/mm^2	[59, 70]
Phase Sensitive SPR	Surface Plasmon resonance	Protein	1.3 nM	[56]
Mach-Zehnder	Interferometry	Protein	0.1 pg/mm^2	[59]
Porous silicon	Interferometry	DNA	2 pM	[56]
Resonant mirror	Waveguide	Protein	~ 0.1 pg/mm^2	[56]
Metal-clad waveguide	Waveguide	Bacteria	~ 10^5 spores/mL	[56]
Fiber Fabry-Perot cavity	Grating Coupler	Protein	25 μg/mL, 1-10 pg/mm^2	[56, 59]
Fiber bragg grating	Grating coupler	DNA	0.1 μM	[56]

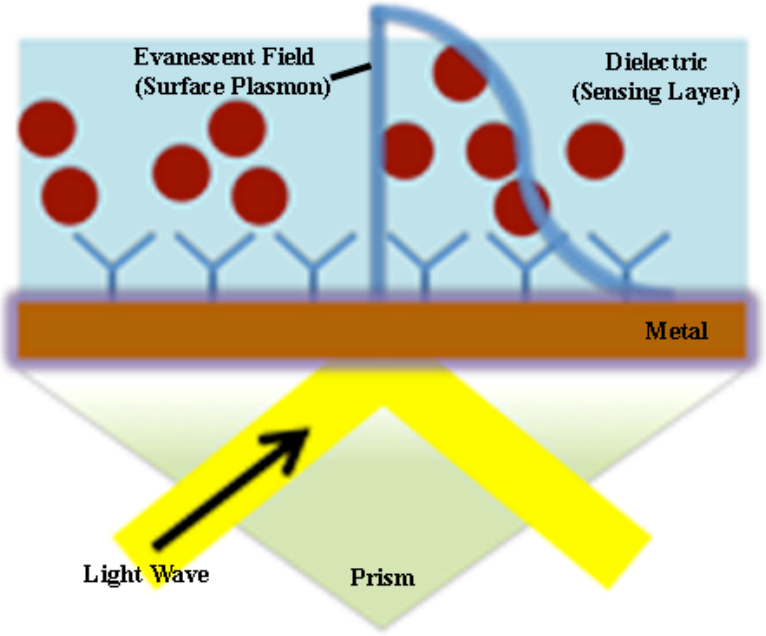

Figure 1.4 Diagram of prism coupled surface plasmon resonance.

1.3.3 Outlook

Advancements in optical sensors have helped overcome some of the challenges in current analytical tools by improving sensitivity and reliability in signal detection and by enabling real-time monitoring of a biomolecular interactions. Adopting these sensitive detectors into well-established analytical methods has been an ongoing trend to help improve existing bioanalytical tools. One of the most practiced hyphenated systems is liquid chromatography-tandem mass spectrometry (LC-MS) with shown improvements in speed, resolution and sensitivity for high-throughput analysis. Since its discovery, LC-MS has been accepted as the preferred technique for characterizing small molecules and many biomolecules in complex biological fluids.[71] As detection techniques evolve, more hyphenated systems (size exclusion chromatography[30] and capillary electrophoresis[30]) have been developed with multiplexed functionalities, and enhanced performance and sensitivity.

Another growing field is nanomaterials bringing together many attractive features. Applying nanomaterials in biosenors has become a new interdisciplinary frontier between biological detection and material sciences.[72] In particular, nanomaterials such as gold nanoparticles,[73] carbon nanotubes,[74] magnetic nanoparticles,[75, 76] and quantum dots[77, 78] have been actively investigated for the development of multipexed sensors and microarrays. Another exciting field is nanopores, with dimensions close to biological processes, these nanopore devices provide greater control and more selective separation. Label-free detection schemes have also been coupled to these structures to perform bioanalytic studies. The

realization of these nanopore devices will provide new strategies for the design of multiplexed systems with the ability to perform DNA sequencing, protein analysis, and ultrafiltration with single-molecule sensitivity and improved cost efficiency.

1.4 Porous Silicon

Porous silicon was discovered in the mid 1950's by Arthur Uhlir at Bell Laboratories. It was found as a brown residue on the semiconducting material while attempting to electrochemically machine silicon wafers for microelectronic circuits. A few decades later, different groups had reported interesting findings on the photoluminescence properties of porous silicon.[79, 80] Since then, the material has been investigated for its chemical, physical and optical properties in various application spanning from chemical sensors to drug delivery. In particular, developments in using porous silicon as label-free optical sensors have been shown to cover a wide range of areas for chemical[22, 81, 82] and biological[83-85] applications in point-of-care diagnostics, environmental sensors, bioanalytics, and pharmaceuticals.[56] The tunable properties of the material possess capability for multiple functions as a "smart dust" material for potential miniaturization of integrated sensing devices.[86]

Porous silicon possesses many attractive features including a high surface to volume ratio (typically around several hundreds m^2/cm^3),[87] controllable pore morphology (pores ~ 1 nm - 100 μm),[88] easily tailored surface chemistry,[89] and tunable optical signatures.[90] The following section will outline some of the approaches that

have been used to take advantage of these attractive features in the field of bioanalytics and biosensing.

1.4.1 Fabrication of Porous Silicon

Porous silicon can be prepared through various methods including stain, electrochemical, and photoelectrochemical etching of silicon wafers.[87, 88, 91] The most common approach is by electrochemical etching of (p- or n- type) silicon wafers in hydrofluoric acid (HF) solutions contained in a Teflon etch cell (Figure 1.5). This is typically carried out in a two-electrode configuration under galvanostatic conditions. A number of different mechanisms have been reported for porous silicon formation.[80, 87, 88, 91, 92] One proposed reaction is outlined in Figure 1.6. Porous silicon formation is initialized when an anodic current is applied to the wafer causing positive hole (h^+) carriers to migrate to the silicon/electrolyte surface. The positively charged surface now is susceptible to nucleophilic attack by fluoride ions, replacing Si-H bonds with Si-F bonds. The polarizing effect of the bonded fluorine allows a second fluoride ion to attack the Si atom generating H_2 gas. The weaken silicon backbone is susceptible to additional attacks by HF and H_2O. As a result, the oxidized silicon is removed from the surface in the form of SiF_4 leaving hydrogen terminated surfaces. This process is driven by the hole carriers and as the hole carriers become depleted, the walls are protected from further dissolution. The resulting nanostructure has a high surface area with retained crystallinity of the silicon.[93]

Porous silicon morphology can be controlled with various parameters such as dopant type, HF concentration, current density, etch duration, and electrolyte composition, resulting in various structures including Fabry-Perot layers,[85] multiplayers,[94] rugate filters,[95] and microcavities.[96] One example is to use a temporal current density profile to construct a desirable morphology (Figure 1.7).[97] The lower image in Figure 1.7a illustrates a nanostructures containing similar spatial modulation in the z-direction as the current density profile that was used to etch the sample. Figure 1.7b shows a planar view of scanning electron microscope image of two samples with distinguishable pore sizes that were prepared from two different current densities, showing the control over pore dimension as a function of current density. Other than the pore size, the thickness of the porous silicon film can be controlled by the duration of the etch. Certain crystallographic faces are more favorable for the etch, which happens more preferably at the tip of the pores, resulting in an uni-direction pore formation. Thus, a longer etch will remove more silicon from the structure resulting in a thicker porous layer. The tunable dimensions and surface area of porous silicon materials that are in the same length scale as the biological molecules have been show to provide a powerful route for molecular sieving and separation based on molecular size and enhanced surface interaction.[27]

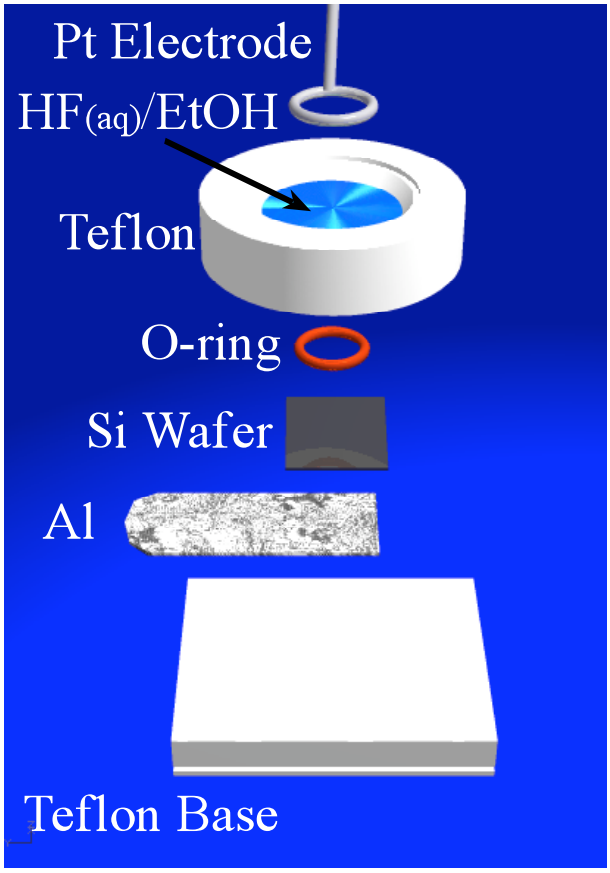

Figure 1.5 Schematic of an etch cell for the preparation of porous silicon samples.

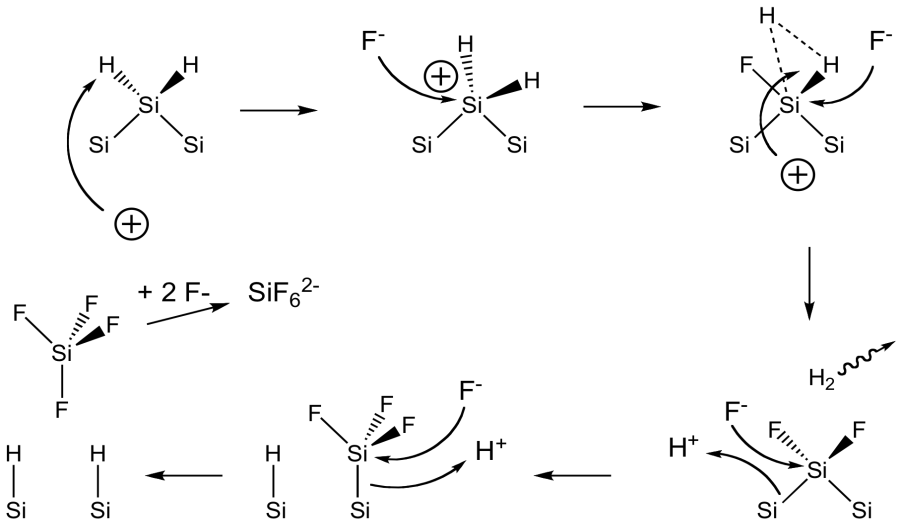

Figure 1.6 Mechanism of porous silicon formation.

a.

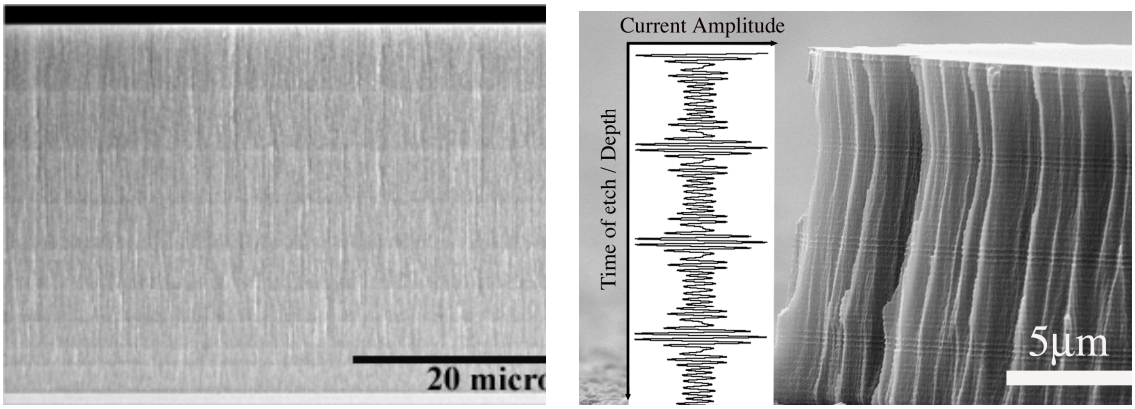

b.

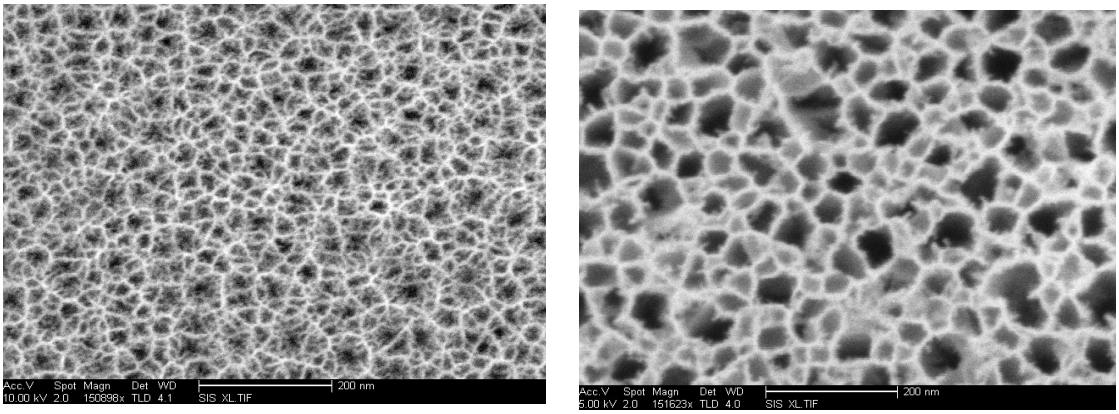

Figure 1.7 Examples of controlled porous silicon nanostructures. **a.** Porous silicon samples prepared from a 9-step current density profile and a composite sinusoidal waveform. **b.** Two different pore sizes are prepared from two current densities (333 mA/cm^2 and 542 mA/cm^2), illustrating current dependent pore formation.

1.4.2 Optical Properties of Porous Silicon

Porous silicon also possesses interesting optical properties that can be used for tracking and identifying biomolecules. These optical properties are determined directly by the physical properties of the material. Porous silicon behaves as a dielectric material with an effective refractive index, *n,* that is directly dependent on its porosity and the refractive index of the material that is embedded in the porous matrix. Thus, any changes in *n* is indicative of changes in the composition of the effective medium, providing an excellent means to track analyte infiltrating into and out the matrix. Here, two classes of porous silicon structures are described: Fabry-Pérot and rugate filters.

Fabry-Pérot filters, also known as Fabry-Pérot interferometers, are single layer silicon films produced from a constant current etch. The reflectivity spectrum collected from the sample is an interference pattern calculated by combining the reflected light waves that has passed through the material constructively and deconstructively. The effective refractive index can be estimated from the Fabry-Pérot relationship:

$$m\lambda = 2nL \tag{1.1}$$

where λ is the wavelength of maximum constructive interference for spectral fringe of order *m*, and *n* is the effective refractive index of the porous layer and its content, and *L* is the physical thickness of the porous layer.[25] The value *nL* is often referred as the optical thickness of a particular porous silicon sensor and is determined by Fourier transformation of the reflectivity spectrum. It is worth mentioning that multilayer structures behave similarly as Fabry-Pérot filters with a resulting reflectivity spectrum that superimposes the interference patterns reflecting from the additional layers.

Rugate filters are thin film layers consisting of a continuous variation of the refractive index in the direction that is perpendicular to the plane of the filter. These materials are usually made using a periodic current waveform. Rugate filters behave as photonic crystals that can filter and allow specific wavelength to pass through the structure. The mechanism is similar to that of multilayer samples except with a larger number of interfaces. Light travels through the material and reflects back constructively and deconstructively filtering out different wavelengths. The position of the resulting peak can be correlated to the optical thickness and used for sensing analytes within and outside of the matrix. Both structures have been harnessed for the detection of various biomolecules and chemical agents.[25, 26, 81, 98] Chapter 2 of this dissertation will provide insight into to selecting the optimal type of sensor to use for different applications.

1.4.3 Surface Modifications

Besides the physical and optical properties of porous silicon, the ease of functionalizing the surface to increase selectivity is also an attractive feature for many applications. Freshly etched porous silicon is thermodynamically unstable and is prone to oxidation to SiO_2 in air or water, resulting in an undesirable baseline drift, therefore various surface chemistries have been developed to chemically graft organic species to the silicon surfaces. However, the different methods can be generalized into two classes: Si-O and Si-C bonds.[89,93]

Surface modification via Si-O bonds is relatively easy and has been used as the main method to passivate silicon devices. One of the most commonly used methods is thermal oxidation. This one step approach is convenient; creating a thin oxide layer that can be readily used for silanol chemistry to attach biomolecules. The negatively charged surfaces in a solution that is greater than pH 2 also offers a potential route for studying electrostatic interactions between the pore walls and the analytes. However, these surfaces have been found to be susceptible to nucleophilic attack, and slowly dissolve in biological media.[93] For the Si-C grafting chemistries, the lower electronegativity of carbon relative to oxygen suggesting a greater kinetic stability of Si-C species on silicon surfaces.[93] Attaching molecules to the porous Si surface via Si-C bonds has also been shown to impart remarkable stability to the porous Si surface relative to Si-H or Si-O surfaces.[99] However, hydrophobic surfaces may denature biological samples, resulting in undesirable changes. Table 1.3 provides three examples of surface chemistries that are commonly used to stabilize porous silicon surfaces.

Table 1.3 Examples of different surface chemistries for porous silicon samples.

Process	Chemical Reaction	Surface Species	Contact Angle(°)
Freshly etched	---	Si-H	102±3
Thermal oxidation	Si-H + O2 =>	Si-O-Si	20±1
Hydrosilation with 1-dodecene	$Si\text{-}H+CH_2=CH_2(CH_2)_9CH_3$ =>	$Si\text{-}(CH_2)_{11}CH_3$	119±2
Thermal Acetylation	Si-H + H-C=C-H =>	"Si-C"	80±3

* adapted from Reference [100]

1.4.4 Smart Dust: Encoded Particles

The term "smart dust" was first coined in 1997 by professor Kristofer Pister, envisioning miniature wireless semiconductor devices made from the microelectronics. A few years later, Schmedake adopted the idea and created a sub-millimeter scale particle that is self-sufficient at performing in situ chemical detection.[82] The particle was fabricated from porous silicon and was devised to move, sense and respond to changes in the environment. The ability to sense and perform signal processing all took advantage of the complex photonic structures in porous silicon. As discussed previously, with careful manipulation of the electrochemical preparation conditions, distinctive reflectivity spectra can be prepared or encoded into the nanostructures to store spectral barcodes and information. Strategies on how to engineer distinctive spectra were first suggested by Berger *et al.*[101] and demonstrated by Meade *et al.* in a multiplexed DNA array[26]. These encoded particles have also been harnessed as drug delivery carriers with the ability to report their payload.[102] These studies have shown a promising new route to exploit the unique optical properties of porous silicon for biomolecular identification in multiplexed manners. Examining and utilizing the encoding ability of porous silicon material for multiplexed biomolecule identification will be discussed in greater detail in Chapter 2 and 4.

1.4.5 Using Porous Si as a Separating and Sensing Matrix

Besides the built-in optical signature and tailored surface chemistry, the physical dimensions of porous silicon have also been exploited directly to separate biomolecules

based on their physical dimensions and surface charge. A recent example employed a lift-off porous silicon film to perform molecular sieving based the size and charge of an analyte.[27] This approach has demonstrated that a porous silicon film with fine-tuned physical properties can be used as a powerful alternative for membrane filtration applications. Other strategies have exploited the optical properties of porous silicon for monitoring and quantifying biomolecular interaction, by attaching biomolecular probes on the surface of the sensors as a potential label-free immunoassay.[25, 94] One of the first example, utilizing both the physical and the optical properties of porous silicon for molecular size estimation, utilized a pore gradient prepared by performing an asymmetric electrochemical etch as seen in Figure 1.8. Subsequently, a double layer porous silicon structure was harnessed to act as a nanoreactor. The double layer structure was designed with a top porous stack to host protease molecules and a bottom layer to capture protease digestion production. This strategy employs both the pore size as well as the optical properties of the material to present a new attractive approach to quantify an enzymatic reaction (Figure 1.9) in real-time.[24] To date, these methods have focused more on the identification process without close examination of the molecular interaction of biomolecules with the pore walls. The transport behavior of biomolecules within porous silicon materials that has characteristic dimensions that are comparable to biomolecules is a more realistic representation of natural membrane phenomena and can provide important insights into this phenomena. In summary, porous silicon materials can be used as a multifunctional material that can perform signal processing, molecular sieving, and sensing all in one platform, continuing with the trend for miniaturizing multifunctional systems.

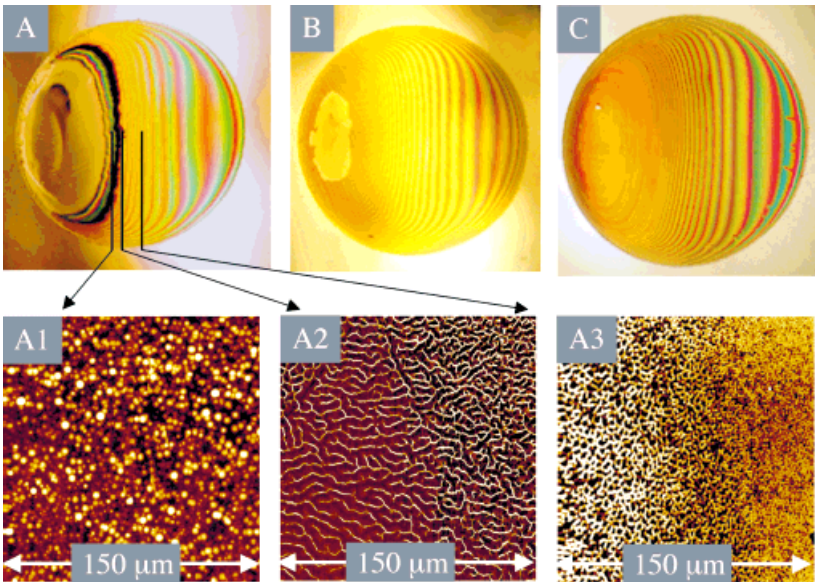

Figure 1.8 Photographs of graded porosity silicon films. Samples A-C are different samples prepared using different electrolyte composition. A1-A3 are atomic force images of different surface morphologies observed at indicated areas on sample A.[19]

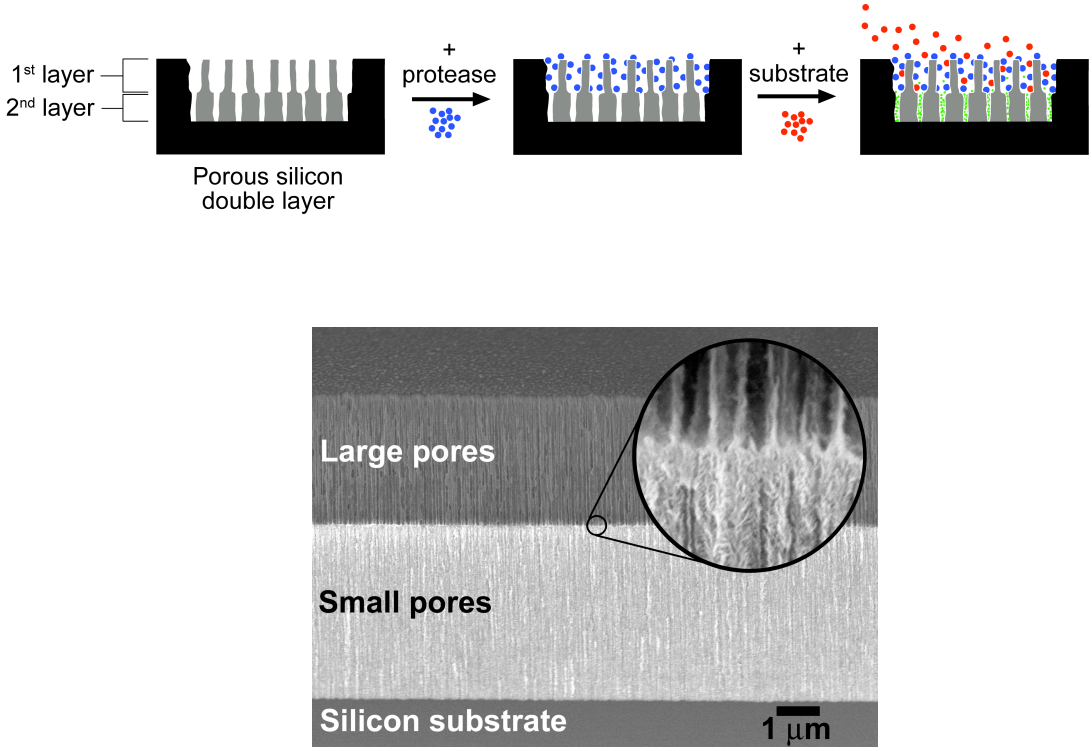

Figure 1.9 Example demonstrating utility of simultaneous sample processing and detection using porous silicon based nanoreactor. The bottom image is a cross-sectional scanning electron micrograph image of a porous silicon nanostructure containing a built-tin size separation matrix.[24]

1.5 Conclusions

Miniaturization, robustness, reliability, potential for mass production with resulting reduction of production costs, low energy consumption, and simplicity has become the design requirements for new bioanalytical tools. The advancements in the field of optical sensors have resulted in an innovative class of microoptical sensors exhibiting detection capability comparable to those sophisticated analytical laboratory instrumentations. In the effort to comply with these needs, optical detection systems have been integrated into current analytical methods to improve efficiency, sensitivity and reliability of existing technique. An emerging field is nanotechnology with an immense number of new materials offering enhanced sensitivity and multifunctional capability to separate, identify, and characterize the analyte of interest, all in one platform.

Recent developments in porous silicon have demonstrated its potential to be an alternative label-free chemical and biomolecular sensor that can be constructed relatively easily and potentially be integrated with conventional silicon “biochip” fabrication technologies. The tunable nanostructure of porous silicon makes it an attractive candidate as a spectrally encoded material that is suitable as an identifier/barcode for multi-analyte bioassays and a spatially controlled structure that is applicable as a chromatography matrix for biomolecule separation. Combining these two properties together with tailored surface moieties, porous silicon material can be treated as a multifunctional material allowing simultaneous separation and detection,

capable of the multiplexed, low-level biodetection necessary to accommodate complex biological mixtures such as urine, whole blood, or serum used for disease diagnosis.

CHAPTER TWO

PREPARATION AND ANALYSIS OF POROUS SILICON MULTIPLAYERS FOR SPECTRAL ENCODING APPLICATIONS

2 Preparation and Analysis of Porous Silicon Multiplayers for Spectral Encoding Applications

2.1 Abstract

Here, two methods used to encode information into the optical spectrum of a porous silicon film using a modulated current-time waveform are compared. In the first approach, a waveform consisting of a sequence of current steps is used to produce a porous silicon multilayer structure. Each layer in the multilayer acts as a Fabry-Pérot interference film, and the superposition of their contributions results in a complicated reflectivity spectrum. The spectrum can then be deconvoluted by means of a Fast Fourier Transformation (FFT), which yields the optical thickness of each of the individual layers and their combinations. The second type of waveform consists of several superimposed cosine waves of differing frequencies. The resulting reflectivity spectrum consists of a series of peaks, each of whose position in the spectrum (frequency at which a peak is at maximum amplitude) corresponds to the frequency of a cosine wave component in the current-time waveform. The two methods of encoding information are compared in terms of repeatability, tunability, and information capacity. The superimposed cosinusoidal waves are found to provide greater information density and a simpler means of decoding.

2.2 Introduction

Bead-based assays generally require a means of encoding the beads to allow their tracking and identification through the course of the assay. Specific labels such as

fluorescent molecular tags, reflective metal stripes, diffraction gratings, and photonic crystals have been used.[90, 103-107] Multilayered porous silicon microparticles have been proposed for this type of application, where the characteristic spectral bands in the reflectivity spectrum of the multilayers are used as the encoding elements. This work investigates two methods to control the spectrum with a current-time waveform. The first method involves a series of constant current-time steps to prepare multilayers. Each layer in the multilayer acts as a Fabry-Pérot interference film yielding a series of peaks that represent the encoding elements. The second method involves a sum of several cosine waves with different frequencies that mimic a rugate filter. In the latter case, the several peaks that appear in the reflectivity spectrum form the encoding elements. In our previous work, we demonstrated that the approach yields at least 4^{10} distinct spectral codes.[90] The goal of this study was to analyze and compare the reliability, bit depth, and reproducibility of the two methods of generating spectral barcodes.

2.3 Experimental Methods

2.3.1 Encoding Current Density Waveforms

Two types of the encoded materials are prepared using the encoded waveforms presented here: 1) composite current step waveform and 2) composite consinusoidal waveform. First, a sequence of constant current-time steps were used to prepare the first type of the encoded material. In order to test reproducibility, three groups of double layer samples were prepared. For each group, the same etching conditions and current density waveform were used. Second, several cosine waves with different frequencies

were summed together to produce a composite waveform. The frequencies of each waveform were designed to differ by a constant amount for each consecutive cosine wave. The waveform was passed to a computer-controlled power supply, which converted it into a current-time etch profile. To determine the reproducibility of this method, two groups of three samples were studied. The reflectivity spectrum of each group contained three distinct peaks, each of which was used for analysis.

2.3.2 Synthesis of Porous Silicon

All samples were prepared from highly doped p-type silicon wafers (boron doped, 0.5-1.5 mΩ·cm resistivity, polished on the (100) face) and anodically etched in a 3:1 solution of 48% aqueous HF:ethanol.[90, 94, 108, 109] Silicon chips with an exposed area of 1.2 cm^2 were contacted on the backside with aluminum foil and mounted in a Teflon etch cell. Samples were then electrochemically etched using the waveforms designed from the previous section in a two-electrode configuration using a platinum counter-electrode and a computer controlled power supply. The waveform generated on the computer was passed to the power supply by means of a digital to analog converter. The power supply was configured to convert the voltage-time waveform into a current-time waveform. Figure 2.1 shows how a waveform transforms into an encoded porous silicon structure.

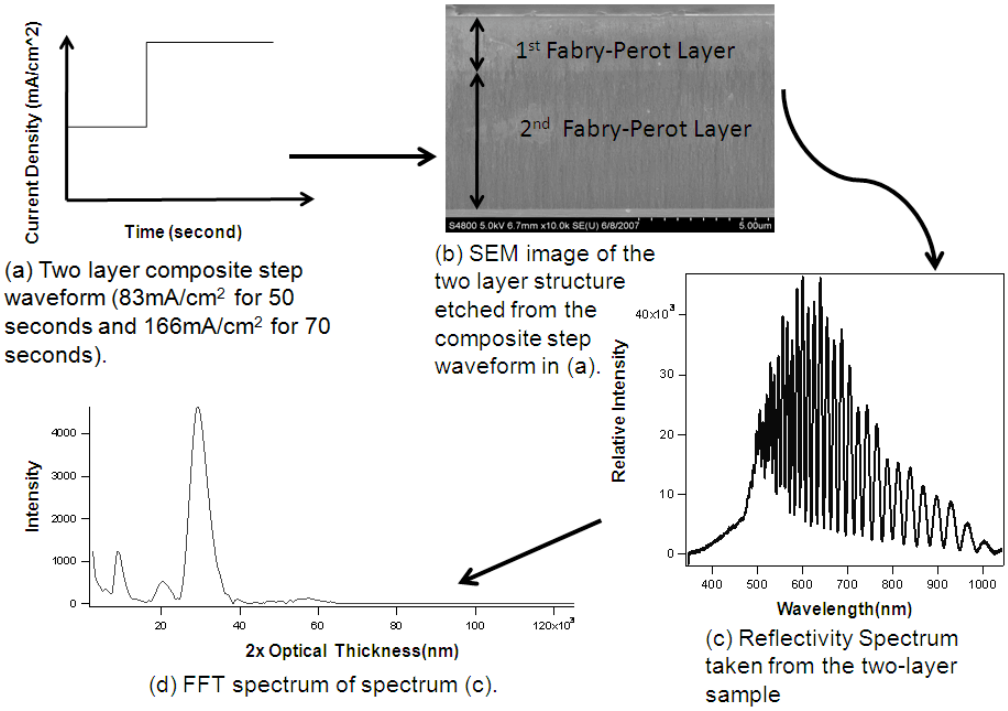

(a) Two layer composite step waveform (83mA/cm^2 for 50 seconds and 166mA/cm^2 for 70 seconds).

(b) SEM image of the two layer structure etched from the composite step waveform in (a).

(c) Reflectivity Spectrum taken from the two-layer sample

(d) FFT spectrum of spectrum (c).

Figure 2.1 Schematic of multilayer porous silicon preparation. Approach used to prepare spectrally encoded porous silicon based on a composite step waveform. The FFT spectrum contains peaks corresponding to a pair of reflective interfaces in the double layer structure.

2.3.3 Thermal Oxidation

For the four- and five-layer samples, the freshly etched porous silicon samples were thermally oxidized at 950 °C for 20 min and then allowed to cool to room temperature. All other samples were used as-prepared., without thermal oxidation.

2.3.4 Spectral Measurement

Reflectance spectra were collected with an Ocean Optics USB-4000 CCD spectrometer fitted with a microscope objective lens coupled to a bifurcated fiber optic cable. A tungsten halogen (Ocean Optics LS-1) light source was focused onto the center of the porous silicon sample with a spot size of approximately 1-2 mm^2. Both the illumination of the surface and the detection of the reflected light were performed along an axis coincident with the surface normal. Reflectivity data were recorded in the wavelength range 400-1000 nm, with a spectral acquisition time of 100 ms.

2.3.5 Data Processing

The collected reflectance spectrum of the multilayer Fabry-Perot stack requires an additional mathematical manipulation to deconvolute the data into a form that can be used for comparison. A Fast Fourier Transformation (FFT) was performed on the data acquired from the encoded samples prepared from composite step waveforms.[94]

2.4 Results and Discussion

2.4.1 Reproducibility

Both encoding methods were tested for sample-to-sample reproducibility using the same etching waveforms. The composite step waveforms will be discussed first. In Figure 2.2, each data point represents a group of three double-layer samples. Each member of a group was etched from a separate silicon chip cut from the same wafer, using the same etching conditions and waveform. Each peak in the FFT spectrum is derived from constructive interference between two interfaces in the structure. In this case, there were three interfaces in the double layer structure (porous silicon/air, 1st /2nd porous silicon layer, and 2nd porous silicon layer/bulk silicon), leading to three peaks in the FFT spectrum.

The position of a given peak in the FFT spectrum corresponds to the value $2nL$, where n is the refractive index and L is the thickness of a given layer, also known as 2 times the optical thickness. Values in Figure 2.2 were determined using the peak in the FFT spectrum of each sample that corresponds to the sum of both layers (1st Fabry-Perot layer and 2nd Fabry Perot layer, see Figure 2.1), and they are plotted as a function of time elapsed in the etching of the second layer. The step waveforms were designed such that the etch current and duration of the first layer was constant (83 mA/cm^2 for 50 sec) while the second layer was varied in current density (167, 333, and 417 mA/cm^2) and duration (60, 70, and 120 sec). Layers etched between 50 to 70 seconds appeared to be more repeatable than those etched for longer times. Overall, the position of the peaks in the FFT spectrum is consistent and reproducible if the samples are prepared from wafers of the same resistivity.

Next, composite cosinusoidal waveforms were studied. Two sample groups of porous layers were prepared for the analysis. The waveforms consisted of a sum of three cosine waves with different frequencies. Each group displays a different reflectivity spectrum containing three distinguishable peaks. The wavelength of a given peak is approximately inversely proportional to the frequency of one of the cosine waves used in the composite waveform. Table 2.1 displays the average wavelength and the standard deviations of all three peaks measured from each sample group. Peaks corresponding to the same cosine component in the etching waveform deviate by ~2 nm from for both sample groups. Although peaks generated using this method show smaller positional errors compared with the composite multilayer method, the composite cosine method is restricted to a smaller encoding range, namely, within the observable range of the CCD spectrometer (in this case 400-1000 nm). The results indicate that both methods produce reproducible patterns in porous silicon with unique reflectivity spectra that can be used to encode information.

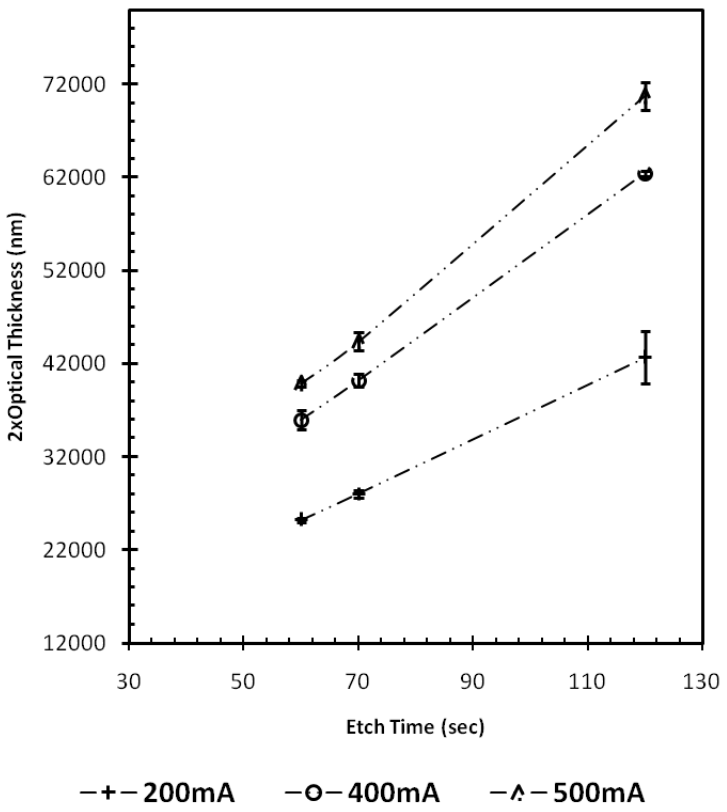

Figure 2.2 Reproducibility of the composite stack method. Double-layer samples were prepared based on the method outlined in Figure 1. The position of the three FFT peaks that correspond to the three values of effective optical thickness (2nL) for the double layer structure are presented as a function of time used to etch the second layer. This second layer was etched at current density of 200, 400, or 600 mA/cm^2 as indicated. The error bars represent two standard deviations above and below the mean. Each data point is the average of the three duplicate samples. The dashed lines are added as a guide to the eye.

Table 2.1 Composite cosinusoidal method: code reproducibility.

Waveform 1*	Waveform 2**	Peak #
623.6 ± 3.2 nm	609.5 ± 2.0 nm	1
658.8 ± 2.5 nm	642.6 ± 2.1 nm	2
696.4 ± 1.6 nm	680.2 ± 2.0 nm	3

* A_{max} and A_{min} were 300 and 33 mA/cm^2, respectively. The samples were etched for 400 sec. Errors indicated are standard deviations.

** A_{max} and A_{min} were 300 and 17 mA/cm^2, respectively. The samples were etched for 260 sec.

2.4.2 Information Capacity

The information capacity of the two methods was compared. The information density of the composite cosinusoidal waveform method has been investigated previously.[90] The composite step method was analyzed first by identifying the effect of an additional layer on the reflectance spectrum of the porous silicon sample. Samples containing three, four, and five distinct Fabry-Perot layers were prepared and examined. The samples were thermally oxidized prior to analysis in order to reduce optical absorption due to residual silicon in the layers.[101]

Two parameters are important to consider in designing the composite step waveform: current density and the duration of each step, which determine the refractive index and the thickness of the layer, respectively.[94, 110, 111] Large differences in current density between adjacent layers result in high index contrast, leading to greater interfacial reflectivity and more pronounced peaks in the FFT spectrum. Although refractive index also affects the position of the peaks, for the range of current densities used in this work the thickness of the porous silicon layer is more significant in determining the position of an FFT peak. To avoid overlapping peaks, any added step with the same current density as any of the previous layers must be etched for a different duration. Double layer structures yield three FFT peaks,[94, 109] and the addition of a new layer adds peaks to the FFT spectrum according to eqn. (2.1):

$$N = \sum_{i=1}^{n} i \tag{2.1}$$

where N is the total number of peaks in the FFT spectrum and n is the number of layers in the film. Figure 3 presents a current-time waveform and the resulting layers and FFT

spectrum for a four-layer etch waveform, where the current density for each layer is alternating between 88 mA/cm^2 and 442 mA/cm^2.

The maximum number of distinguishable peaks that can be observed was studied by looking at the full width half maximum (FWHM) of the peaks in the observable range of the FFT spectrum. The FWHM was determined to be approximately 3500 nm for the oxidized samples used in this study. The FFT spectral range is limited by the pixel resolution of the CCD used in the experiment. The Nyquist theorem requires at least two data points per cycle, setting an upper limit on the density of optical information that can be embedded in the nanostructure. In the present case, the spectrometer-determined upper limit of the FFT spectrum is 1.5 x 10^6 nm. For half-linewidth separation this translates to 428 peaks, or bits. However, utilizing the entire FFT spectrum is unrealistic, since each additional layer in a stack adds more than one peak to the FFT spectrum and it increases the overall thickness of the layer. Much of the reflected light signal can be lost to absorption or scattering in the thicker structures. To correct for silicon absorption, thermal oxidation was used to convert silicon to silica. After oxidation, the reflectivity spectrum exhibited all the predicted peaks in a four-layer stack as shown in Figure 2.3(d). It is evident that light was not able to penetrate the fourth layer as seen in Figure 2.3(b)-(c), where peaks assigned letters G-J were not observed in the FFT spectrum of the unoxidized sample. These peaks involve the last layer in one or both of the reflective interfaces. Furthermore, relative peak intensities were attenuated in the oxidized samples. This is attributed to the lower index contrast that exists between layers of porous silica compared to layers of porous silicon.

Because reflectivity at a given interface depends on the index contrast and thus the relative difference in porosity between adjacent layers, the relative intensities of the FFT peaks depend on layer arrangement. The relative relationship of these various peak intensities can also be used as a part of the spectral code. Whereas the presence or abscence of a peak can be thought of as a single binary digit, if several intensities can be reproducibly encoded, the number of available codes increases dramatically (for a given number of peaks m and a set number of intensity levels n, the number of discrete numbers that can be represented is m^n-1). Although there are many ways to increase the information content in the FFT spectra, this method is restricted by the physical thickness added to the strucuture each time a new layer is added. An interesting attribute of the method is that some of the peaks can be used as error checking bits. This is because each additional layer contributes to more than one peak in the resulting FFT spectrum.

Next, the information capacity of the composite cosinusoidal method was examined. The information density of the composite cosinusoidal waveform method was probed by preparation of 10-, 12-, and 20- component waveforms. The etch profiles were created by adding 10, 12, or 20 cosine waves with different (equally spaced) frequencies using the method described previously.[90] Resulting spectral codes appear in the reflectivity spectra as a series of peaks shown in Figure 2.4(a), (b), and (d), and they do not require FFT processing to obtain the code embedded in the nanostructure. Figure 4(c) represents the composite cosinusoidal waveform that was used to electrochemically prepare the 20-peak rugate filter whose spectrum is displayed in Figure 2.4(d). The 20-peak rugate filter shown in Figure 2.4(d) demonstrates the

largest number of peaks yet produced by the waveform superposition method. As demonstrated from our previous work, the number of codes is not restricted to the number of peaks. More possible spectral patterns can be produced by adjusting the amplitude ranges (bit depth) as described above.[90]

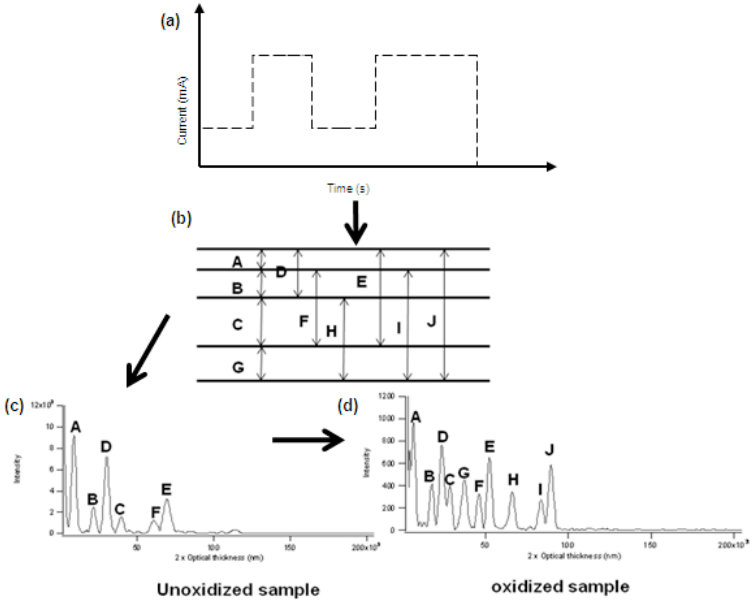

Figure 2.3 Spectral barcodes synthesized from a composite step waveform. (a) Composite step waveform used to produce (b) the four-layer structure shown. All the possible layer combinations that can generate a peak in the FFT spectrum (c) are indicated. Each lettered arrow corresponds to the bounding interfaces of a Fabry-Perot layer and a peak in the FFT spectrum of the oxidized sample (d). The spectra (c) and (d) are the FFT spectra derived from the reflectance spectra of the four-layer stack before and after thermal oxidation, respectively.

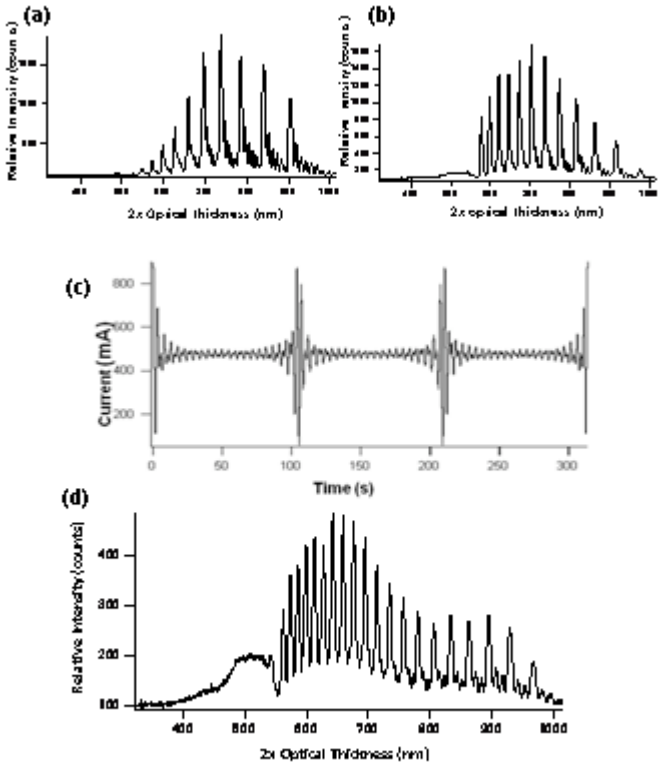

Figure 2.4 Spectral barcodes synthesized using a composite cosinusoidal waveform. Spectra of samples resulting from waveforms containing 10 (a) and 12 (b) cosine waves with sequentially stepped frequencies. (c) Composite cosinusoidal waveform consisting of 20 superimposed cosine waves results in a 20-peak reflectivity spectrum (d).

2.5 Conclusions

Both composite step and summed cosine waveforms can be used to fabricate spectra with distinguishable codes with relatively high reproducibility and tunability. An additional decoding step is needed for the multilayer stack (a FFT), adding an extra level of complexity to that particular method. Each layer added to the stack generates more than one peak in the spectrum, which can be used as an error check bit. However, each additional layer requires the porous silicon sample to be thicker and may not be desirable for barcoding applications that utilize porous silicon as target identifiers. For composite cosinusoidal waveforms, each added frequency produces one additional peak without changing the thickness of the sample, which is ideal for multiplexed bioassays that can be decoded easily. The summed cosine method allows quick and easy readout using conventional low-cost CCD spectrometers. On the other hand, thick and constant pore dimensions can provide a reservoir to observe molecular interaction and real-time kinetic acquisition. Step changes of pore diameters can also be exploited to monitor analyte movement and separate analytes based on their size. Despite all these differences between composite step and cosinusoidal waveforms, both method provide complementary detecting platforms that makes porous silicon biosensors versatile and an attractive alternative for label-free biosensors.

Chapter two, in part or in full, is a reprint (with co-author permission) of the material as it appears in the following publication: Chen, M. Y.; Meade, S. O.; Sailor, M.J., Preparation and Analysis of Porous Silicon Multilayers for Spectral Encoding Application. *Physica Status Solidi (c)* 2009, 6(7), 1610-1614. The author of this dissertation is the primary author of this manuscript.

CHAPTER THREE

TEMPERATURE AND STRUCTURE DEPENDENT THERMAL OXIDATION OF ENCODED POROUS SILICON PARTICLES

3 Temperature and Structure Dependent Thermal Oxidation of Encoded Porous Silicon Particles

3.1 Abstract

"Smart dust", porous silicon (pSi) materials have been shown with interesting properties that can be used as multifunctional materials for bio-and chemical- sensing.[86] Applying this material in the field of drug delivery has also received much interest because of its high loading capacity.[18, 112] Although pSi material has been demonstrated with great biocompatibility, only completely oxidized, amorphous SiO_2 is a FDA approved Generally Recognized as Safe (GRAS) material. Here, two encoded pSi structures are studied for its ability to maintain a detectable optical signal after thermally transformed into $pSiO_2$. The crystalline structure of pSi is examined and compared as a function of temperature and structure. Reflectivity spectra of the encoded particles are obtained before and after thermal oxidation, investigating different degrees of oxidation as spectral code intensity decreases due to physical changes in the material. The result shows reduced but detectable optical signatures in amorphous $pSiO_2$ particles as smart, standalone identification and delivery systems.

3.2 Introduction

Freshly prepared encoded porous silicon (pSi) undergoes slow oxidation in air, to silicon dioxide, resulting in an undesirable change to the optical properties of the material.[93] Different surface modifications have been explored and exploited to stabilize silicon surfaces for various applications. The approaches can be generalized

into two classes based on the surface species: Si-O and Si-C bonds.[89, 113, 114] Surface modification via Si-O bonds is relatively easy and has been used as the main method to passivate silicon devices.[115] Of which, the most commonly used method is thermal oxidation. This one step approach is convenient; creating a thin oxide layer that can be readily used for silanol chemistry to attach biomolecules.[26] The chemically modified surfaces are also biocompatible and inert suitable for a wide range of applications including drug delivery,[14] chromatography,[116] biosensing,[117] microarrays,[118] and multiplexed assays[26].[119] Until recently, pSi has only been used as a drug carrier to host its content.[112, 119] Using encoded mesoporous Si as a smart, self-reporting system for sustained drug delivery has only been reported recently.[102] As pSi gain more attention as "smart dust" carriers, a completely oxidized material that complies to the Generally Recognized as Safe (GRAS) guideline provided by FDA is essential for pharmaceuticals to pursue this approach. Unlike pSi, fully oxidized, amorphous SiO_2 is a FDA approved GRAS material. Although the formation and properties of Si and SiO_2 surfaces is one of the most investigated subjects in surface sciences, little has reported on the optical properties of encoded porous silicon particles as a function of both temperature and nanostructures. In this study, two types of encoded pSi particles (multilayer and rugate filters) were fabricated and oxidized at various temperatures to study thermal oxidation of pSi to amorphous $pSiO_2$ and the code fidelity after thermal oxidation at each temperature. The aim is to demonstrate that encoded pSi particles can be completely converted to amorphous $pSiO_2$, while maintaining its optical properties and signal processing ability, as a nontoxic and ingestible FDA approved material applicable to smart drug delivery and barcoding systems.

3.3 Experimental Methods

3.3.1 Synthesis of Encoded Porous Silicon Nanostructures

3.3.1.1 Composite Current Step Waveform

Double layer structures with the first and second layer etched at 250 and 47 mA/cm^2, respectively. Each layer was etched for 130 s for a total of 260 s to ensure comparable etching conditions with the prepared rugate filters.

3.3.1.2 Composite Cosinusoidal Waveform

Three cosine waves with different frequencies were summed together to produce a composite waveform. The frequencies of each waveform were designed to produce peaks between 600 to 700 nm and the amplitude of the waveform was between 250 and 47 mA/cm^2.

3.3.2 Fabrication of Porous Silicon

All samples were prepared from highly doped p-type silicon wafers (boron doped, 0.5-1.5 mW·cm resistivity, polished on the (100) face) and anodically etched in a 3:1 solution of 48% aqueous HF:ethanol.[90, 109, 117] Si chips with an exposed area of 3.2 cm^2 were contacted on the backside with aluminum foil and mounted in a Teflon etch cell. Samples were then electrochemically etched using the waveforms designed as described above in a two-electrode configuration using a platinum counter-electrode and a computer controlled power supply. The waveform generated on the computer was passed to the power supply by means of a digital to analog converter. The power

supply was configured to convert the voltage-time waveform into a current-time waveform.

To prepare pSi particles, a freshly etched pSi film was first lifted off by replacing the etching solution with 3.33% HF in ethanol and etched at 3 mA/cm^2 for 260 s. The liftoff film was then removed from Si substrate with edges cut off keeping only the center (~3mm radius) to eliminate undesirable edge effect. The center of the liftoff film was then transferred into a glass vial with 3.5 ml of ethanol and sonicated for 3 minutes.

3.3.3 Thermal Oxidation

For both structures, the freshly etched pSi particles were thermally oxidized at 200, 400, 600, 900 and 1000 ºC for 1 hour in ambient air and then allowed to cool to room temperature.

3.3.4 Physical Characterization of Porous Silicon Encoded Particles

Freshly etch porous silicon layer thickness was examined with a Philip XL 30 environmental SEM operating in second electron mode. Accerlating voltages of 10 to 20 keV.

Nitrogen adsorption-desorption isotherms of porous Si microparticles were recorded at 77 K using a Micromeritics TriStar 3000 volumetric apparatus. Prior to the adsorption experiment, porous Si samples were degassed overnight. The surface area of the sample was measured by the BET (Brunnauer-Emmett-Teller) method, which yields the amount of adsorbate corresponding to a molecular monolayer. The pore dimensions

were determined using the BdB (Broekhof-de Boer) method from the nitrogen adsorption curve.[120-122]

3.3.5 Powder X-ray Diffraction

Samples were placed into a mortar and grinded into powder. Once done, samples were then transferred into a 1.5 mm glass capillary. To ensure samples were packed with similar density, the glass capillary was dropped 25 times in a larger diameter glass tube. XRD data were acquired from a Bruker AXS diffractometer with Cu radiation and collected at 2 Theta values of 15, 40, 65, 90, and 115 for 5 minutes each.

3.3.6 Spectrum Acquisition and Analysis

Encoded and thermally oxidized particles were placed on an electrical tape on a microscope slide. Reflectance spectra were acquired using a Nikon LV-150 fluorescence microsope in combination with a SpectraPro275 scanning monochromator. A CoolSnap HQ2 (Photometrics) 14 bit, monochromatic camera was used to acquire reflectivity images. Metamorph software (Molecular Devices) was used to control the camera and the monochromator to acquire spectral image stacks. All images were acquired with a 10x objective with a binning of 4. Reflectivity images were acquired while the monochromator was scanned from 450 to 725 nm in 1 nm steps. A 25 ms-exposure image was used at each step, resulting in a spectral image stack with 276 sequential images. Image stacks were analyzed using a code developed in MATLAB, which yielded the wavelength maximum of the reflectivity spectrum for each particle.

The value of wavelength maximum for each particle was determined from the average of 5 pixels.

Collected reflectance spectra of the multilayer Fabry-Perot stack required an additional mathematical manipulation to deconvolute the data. A Fast Fourier Transformation (FFT) was performed on the data acquired from the encoded samples prepared from composite step waveforms.[117] Spectra for the rugate filters were used as acquired.

3.4 Results and Discussion

3.4.1 Optical Properties and Physical Characterization of Encoded Porous Silicon Nanostructures

Two porous silicon (pSi) structures were prepared through electrochemical etch of single crystal silicon wafers: multilayer and rugate structures. The first structure was electromachined using a 2-step current, 250 mA/cm^2 for 130 s followed by 47 mA/cm^2 for 130 s. The optical properties of this multiplayer structure behave similarly as Fabry-Pérot filters with resulting reflectivity spectrum superimposes the interference patterns reflecting from the additional layers.[109, 117]

Fabry-Pérot filters are single layer silicon films produced from a constant current etch. The reflectivity spectrum collected from the sample is an interference pattern calculated by combining the reflected light waves that has passed through the material constructively and deconstructively. The Fabry-Pérot relationship describes this process:

$$m\lambda = 2nL \tag{3.1}$$

where λ is the wavelength of maximum constructive interference for spectral fringe of order *m*, and *n* is the effective refractive index of the porous layer and its content, and *L* is the physical thickness of the porous layer. The value *nL* is often referred to as the optical thickness of a particular porous silicon sensor and is determined by Fourier transformation of the reflectivity spectrum.

The second structure was constructed using a composite current profile obtained from superimposing three different cosinusoidal waves with distinguishable frequencies, generating a triple peak reflectivity spectrum following the method described previously.[90] Three peaks were designed to fall between 600-700 nm allowing detectable blue shifts in the peak position after oxidation. This type of structure is also known as rugate filters with periodic variations in refractive index in the direction of pore growth.[123] Rugate filters behave as photonic crystals allowing specific wavelength to pass through the structure. The mechanism is similar to that of multilayer samples except with a larger number of interfaces. Light travels through the material and reflects back constructively and deconstructively filtering out different wavelengths. The position of the resulting peak correlates to the physical structure as well as the refractive index of the material giving pSi its unique but tunable optical signatures.

One of the key studies is to compare thermal oxidation of rugate and multilayer structures. As mentioned, the multiplayer structure was prepared with two current densities, 250 and 47 mA/cm^2. For the purpose of comparison, the rugate structure was fabricated using cosinusoidal waves with alternating amplitude from 250 to 47 mA/cm^2 and etched for 260 s, similar to the conditions used to prepare the multilayer structure.

Two engineered structures were then characterized using BET and SEM. As displayed in Table 3.1, the multilayer structure exhibits greater surface area, larger average pore diameter, and thicker porous layer. Comparing to the multilayer, rugate samples have thinner film layer consisting smaller porosity, suggesting slower etch rate with greater amount of Si remained in the matrix after the etch. Smaller surface area and greater amount of Si can also suggest longer oxidation or higher temperature needed comparing to the multilayer structure for complete oxidation.

Table 3.1 Physical characteristics of encoded porous silicon particles.

	Thickness (μm)*	Surface Area (m^2/g)**	Porosity (%)**	Average Pore Diameter (nm)***
Rugate	13	434	74	9
Multilayer	15	499	84	14

* Sample thickness estimated from cross-section scanning electron microscopy images of the samples.
** Esimated using BET (Brunnauer-Emmett-Teller) analysis method.
*** Approximated using the BdB (Broekhof-de Boer) method from the nitrogen adsorption curve.

3.4.2 Thermal Conversion of Encoded Crystalline Porous Silicon to Amorphous Porous Silica Structures

Two encoded pSi structures were subjected to thermal oxidation in five different temperatures ranging from 200 to 1000 °C for an hour. The blue traces in Figure 3.1a and b exhibit single crystalline Si peaks observed from powder X-ray diffraction (XRD) for freshly etched encoded particles. Orange and red traces for the top two plots in Figure 3.1 show Si crystalline peak intensities after thermal oxidation at 600 and 900 °C, respectively. At 900°C, crystalline peaks for Si were not observable for both structures. In order to compare the degree of oxidation between the two structures, the intensity of the most prominent crystalline peak for Si was used. The y-axis in Figure 3.1c is estimated from the measured intensity of the <111> Si peak from samples treated at each temperature in respect to freshly etched samples. Diminishing peak intensities as temperature increases for both pSi were observed, suggesting a temperature dependent thermal oxidation. Furthermore, multilayer samples display complete oxidation at 600 °C as opposed to 900 °C for rugate samples, implicating a faster oxidation process comparing to rugates.

Both multilayer and rugate structures exhibit a three-peak reflectivity spectrum as shown in Figure 3.2. After complete conversion to amorphous silicon, both structures retained their optical properties except with reduced peak intensities and shifted peak positions as a result of roughen surfaces, decreased pore sizes, and reduced intrinsic absorption coefficient of the material by converting Si to SiO_2.[124] Here, two pSi structures were thermally oxidized into amorphous structures with retained optical properties.

a. Rugate

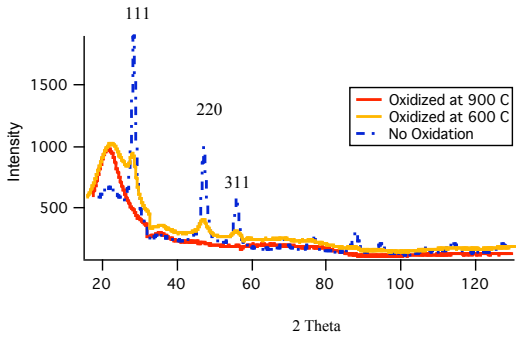

b. Multiplayer

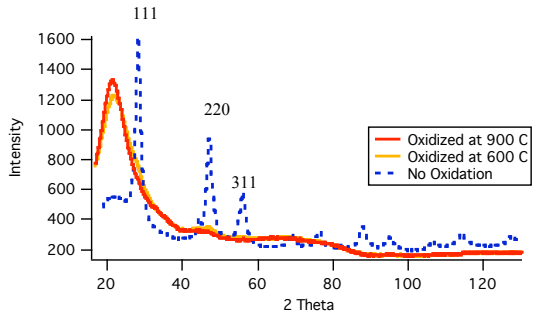

c.

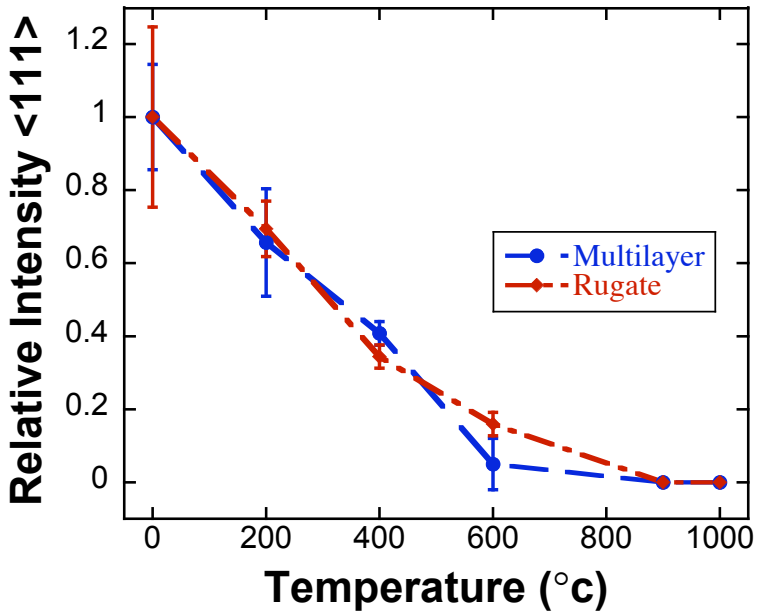

Figure 3.1 Thermal oxidation of encoded porous silicon (pSi) particles into amorphous silica. Powder X-Ray diffraction (XRD) measurement of **a.** rugate samples and **b.** multilayer samples before and after thermal oxidation at 900 °C. **c.** <111> silicon crystalline peak obtained from XRD was used to determine the amount of silicon left in the matrix. Two traces were estimated in respect to unoxidized samples.

a. Rugate Filters

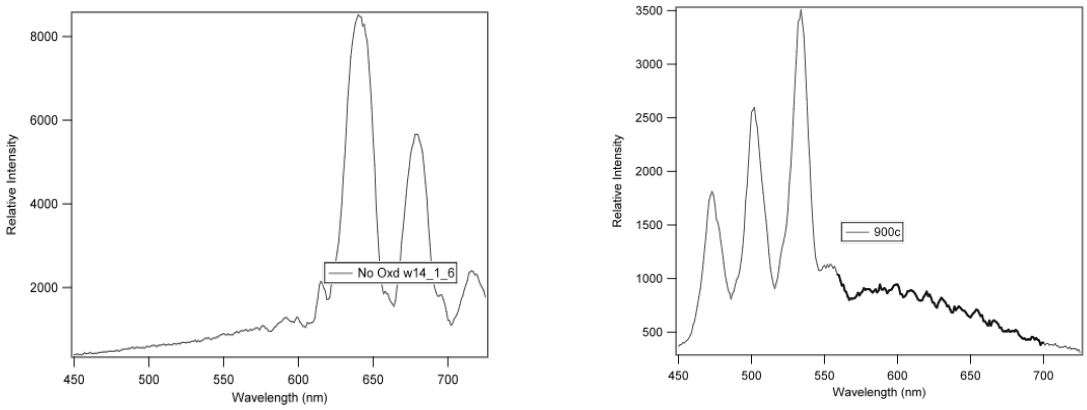

b. Multilayer

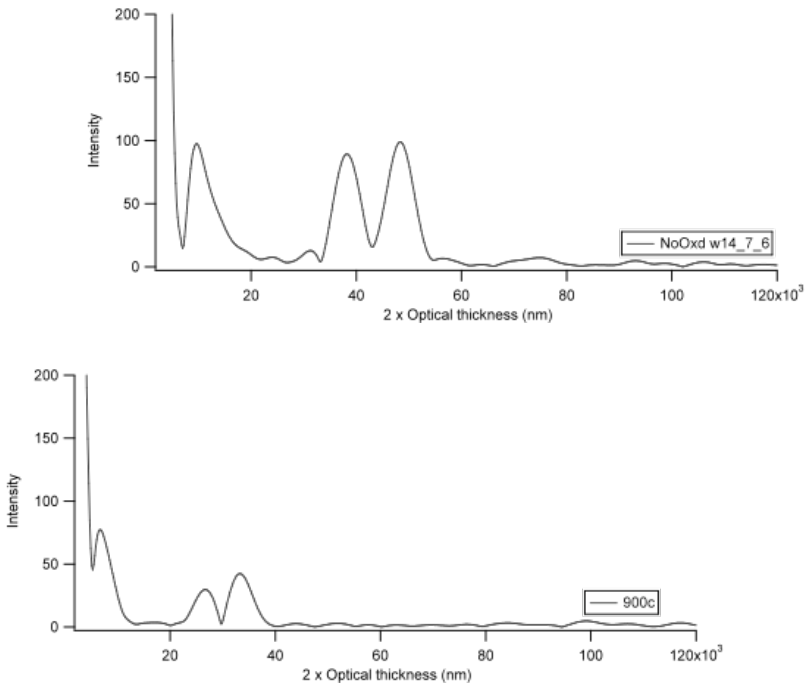

Figure 3.2 Reflectivity spectra of encoded porous silicon particles. a. Top two figures are spectra obtained experimentally from the microscope.

3.4.3 Digital Simulation of Reflectivity Spectrum

A theoretical approach was used to verify the thermal conversion of pSi to $pSiO_2$. Reflectivity spectra of fully oxidized samples were simulated using SCOUT, a software written by W. Theiß to theoretically predict reflectance spectra of multilayer structures in different materials. Two parameters characteristic of the film, namely, the porosity and the physical thickness of the layer obtained from BET and SEM were used for the calculation. Optical constants of the film were derived using Bruggeman model and the refractive index profile within the rugate sample was estimated as a function of current density. Figure 3.3 shows the calculated reflectivity spectrum of a fully oxidized rugate sample. Simulate $pSiO_2$ reflectivity spectrum appears to be in good agreement with the experimentally observed spectrum for a rugate sample oxidized at 900 °C, showing more than 98% silica content within the encoded particles.

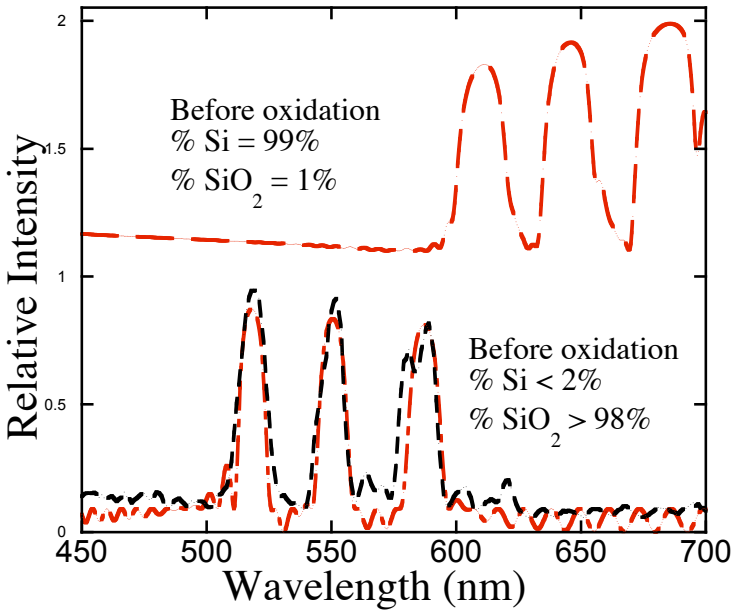

Figure 3.3 Scout simulated spectra predicting silica content in comparison with experimentally measured spectrum. The red trace represents the simulated spectra and the black trace represents the experimentally measured spectrum.

3.5 Conclusions

Freshly etched porous silicon (Si) is unstable and undergoes slow oxidation due to its hydrogen-terminated surface that is susceptible to hydrolysis. [86, 113, 125] In this study, we demonstrated that pSi could be converted to $pSiO_2$ with its optical code still intact for detection. Peak shift of both reflectivity and FFT spectrum were consistent with refraction index change of the material. Furthermore, two different pSi structures exhibited different oxidation rate suggesting faster oxygen diffusion process for multilayer structures. In conclusion, both pSi films constructed from composite cosinusoidal and step waveforms can be modified by thermal oxidation to have more stable surface with intact optical information that can be used for biosening, multiplexed biomolecular arrays, and most important, for "smart" drug delivery systems.

Chapter three, in part, is a reprint (with co-author permission) of the material as it appears in the following publication: Chen, M. Y.; Sciacca, B.; Miskelly, G. M.; Sailor, M.J., Temperature and Structure Dependent Thermal Oxidation of pSi. *manuscript in preparation.* The author of this dissertation is the primary author of this manuscript.

CHAPTER FOUR

EXTRACTING SPECTRAL INFORMATION FROM ENCODED POROUS SILICA MICROPARTICLES FOR MULTIPLEXED DNA ASSAYS

4 Extracting Spectral Information from Encoded Porous Silica Microparticles for Multiplexed DNA Assays

4.1 Abstract

Personalized medicine has received much interest in recent years since the beginning of human genome project. Although an immense amount of information has been uncovered, the need for innovative approach with faster and more cost efficient detection is still under investigation. One idea is to design a platform that is capable of detecting and identifying multiple probes at the same time. Porous silicon (pSi) particles have been shown to exhibit unique spectral signatures offering a new method for biomolecular identification in a multiplexed manner. In this Chapter, spectral information of encoded pSi particles was extracted and used to identify multiple DNA targets at the same time. The result demonstrated that the spectral codes of pSi particles are stable and distinguishable as alternative identifers.

4.2 Introduction

The discovery of multiplexed assays has played an important role in the field of genomic, proteomics, and epigenomics, resulting in new developments in diagnostic and therapeutic tools.[126] In order to screen and identify multiple analytes in a single array, multiplexed assays generally require a means to track and identify probing molecules through the course of the assay. Currently, the methods used to identify probes are classified into two categories based on how the identity of the probe is

recognized. Usually, chemical probe sites are segregated spatially, whose spatial address are used to determine the identity of the probe. Alternatively, randomly ordered probe supports in the forms of microspheres, microrods, or microdiscs incorporated with identifiers (i.e quantum dots,[127, 128] striped metallic rods,[103] fluorescent dyes,[129] and holographic microgratings,[130] etc) are used to obtain probe identity.[126, 131, 132]

Complex photonic structures in porous silicon (pSi) have been studied extensively for their unique spectral properties over the years.[90, 101, 123] As discussed in Chapter 1, with careful manipulation of the electrochemical preparation conditions, these distinctive reflectivity spectra can be prepared or encoded into the nanostructures for storing spectral information. Strategies on how to engineer distinctive spectra were first suggested by Berger *et al.*[101] and demonstrated by Meade *et al*,[90] superimposing various sinusoidal waves into a current density profile to encode information into Si structures. In this Chapter, spectral information of encoded $pSiO_2$ particles was extracted and used in a multianalyte assay to detect and identify multiple DNA sequences simultaneously, presenting an alternative identifier for multiplexed bimolecular identification.

4.3 Experimental Methods

4.3.1 Fabrication of Encoded Porous Silicon Particles

A single crystalline silicon wafer (resistivity 1 mΩ-cm) was electrochemically etched in an HF solution (3:1 aqueous 49% HF:ethanol by volume) using a current-time waveform consisting of six superimposed sine waves of different frequencies. Encoded

pSi microparticles were prepared from freshly etched pSi sample using microfabrication described previously.[97]

4.3.2 Thermal Oxidation

Freestanding microfabricated pSi particles were first transferred to a nickel crucible and placed in a tube furnace at 500 ºC, ramped to 950 ºC at a rate of 50 ºC /min, held at 950 ºC for 30 min, cooled back to 500 ºC and then removed from the furnace. The particles were rinsed in the crucible with 0.05% $HCl_{(aq)}$, transferred by pipette to a microcentrifuge tube and rinsed with absolute ethanol.

4.3.3 Image Acquisition and Analysis

Both reflectivity spectra and fluorescence images were acquired using a Nikon LV-150 fluorescence microscope connected to either a 100 W tungsten filament lamp (reflectivity spectra) in combination with a SpectraPro 275 scanning monochromatora or a 100 W mercury arc lamp (fluoresce images). In fluorescence mode, standard filter cubes containing the desired dichroic, excitation and emission filters were placed in the optical path. In the "particle decode" mode, a 50/50 mirror was placed in the optical path. A CoolSnap HQ2 (Photometrics) 14 bit, monochromatic camera was used to acquire fluorescence as well as reflectivity images. Metamorph software (Molecular Devices) was used to control both the camera and the stepper motor of the monochromator, allowing for the generation of spectral image stacks.

All images were acquired with a 10x objective with a binning of 2, yielding a 520 x 696 pixel image. Prior to analysis, the image was cropped to 480 x 480 pixels

covering an area of about 570 x 570 μm. Fluorescence images were acquired using the "Cy5.5" filter combination (excitation filter centered at 650 nm, 45 nm bandpass; dichroic filter centered at 680 nm; emission filter centered at 710 nm, 50 nm bandpass) and the "Cy3" filter combination (excitation filter centered at 535 nm, 50 nm bandpass, dichroic at 565 nm; emission filter centered at 610 nm, 75 nm bandpass) for imaging Alexa Fluor 680 and 555, respectively. The illumination source was then switched from the filtered mercury lamp to the monochromated tungsten filament lamp, and reflectivity images were acquired while the monochromator was scanned from 400 to 725 nm in 1 nm steps. A 15 ms-exposure image was acquired at each step, resulting in a spectral image stack with 326 sequential images.

4.4 Results and Discussion

4.4.1 Encoding and Assay Methodology

Figure 4.1 provides an overview of the multiplexed DNA assay utilizing encoded $pSiO_2$ particles to identify DNA sequences. The preparation of encoded pSi particles and the general principles of the decoding method used in this work have been presented in earlier publications,[86, 90, 97, 133] but a brief summary will be presented here. First, the "spectral barcode" was generated by programmed electrochemical etch of a single crystal Si wafer. The etching waveform consisted of a superposition of six sine waves, generating a complex stratified porosity gradient in the direction perpendicular to the surface of the wafer. This porosity gradient acts like a one-dimensional photonic crystal; the spectrum of light reflected from the material consists of a series of sharp peaks that act as the "bits" in the spectral code (Figure 4.1b). Because of the 1D

photonic structure, these spectral codes are only observable when the microscope axis is coincident with the gradient direction. The porous film was lithographically patterned into disks with 25 μm in diameter, and the microparticles, each containing the identical code, were lifted off from the substrate.[97] The microparticles were stabilized and prepared for surface functionalization by thermal oxidation to give translucent microparticles of porous silica. The porous SiO_2 microparticles were then functionalized by silanes allowing further biofunctionalizations.[134] The functionalized porous SiO_2 microparticles were modified with an oligonucleotide, acting as the capture probe for the assay (Figure 4.1a).

Three groups of pSi particles with distinctive spectral signatures were prepared for this experiment, as seen in Figure 4.1b. Although the code used in this work was 6 bit binary (64 total possible codes), > 10 bits with grayscale encoding has been demonstrated in this system.[135] Each particle type was functionalized with the indicated oligonucleotide sequence in Table 4.1. Fluorescently labeled complementary oligonucleotide sequences were used as received.

For the hybridization experiment, a mixture of different oligonucleotide probes attached to the microparticles (Figure 4.1b) was added to a solution containing the fluorescently labeled oligonucleotide targets. After the reaction, encoded particles were rinsed and collected using an alumina filter. Subsequently, the fluorescence images and the reflectivity image stack of the hybridized $pSiO_2$ microparticles were acquired. The fluorescence images indicate provides a means to verify oligonucleotide hybridization. And, the reflectivity spectrum allows the determination of the identity of the particular probe oligonucleotide sequence that was attached to the specific spectral barcode.

The multiplex assay was decoded using a system that consisted of a standard fluorescence microscope combined with a scanning monochromator that provides a spectrally tunable illumination source. While systems capable of both fluorescence detection and spectral microscopy have been constructed and demonstrated previously,[136, 137] the present system provided ready access to the narrow bandwidth reflectivity spectra required to decode multi-bit spectral barcodes over an entire field of view.

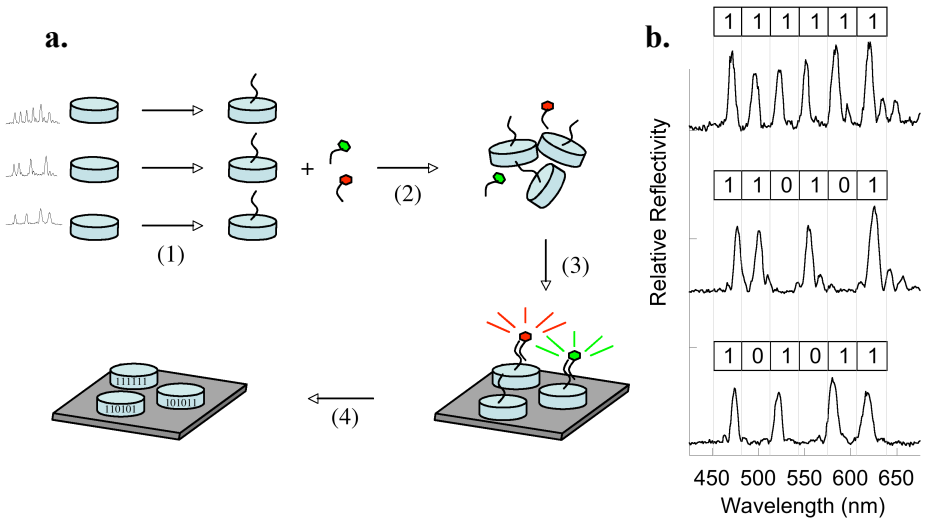

Figure 4.1 Summary of the procedure used in the DNA hybridization assay. **a.** (1) Several types of DNA-labeled encoded particles are prepared. Each set of particles contains a unique spectral barcode (three examples are shown in Figure 2B) and a specific DNA probe sequence. (2) The particle types are pooled together and the combined mixture is reacted with fluorescently labeled target sequences. (3) The particle suspension is washed, assembled onto a surface, and a fluorescence microscope image is acquired. (4) Without moving the particle assembly relative to the imager, reflectivity spectra of all the particles in the field are acquired simultaneously by means of a wavelength-scanned illumination source. **b.** Reflectivity spectra observed for single pixels of each of the three encoded particle types used in this study. The binary codes assigned to each spectrum are shown. To assign the codes, the spectrum is binned into six spectral regions. A bin is assigned a code of "1" if the spectral intensity in that bin exceeds a threshold value. If no peak is observed in the spectral region, the bin is assigned a code of "0."

Table 4.1 Spectral codes, oligonucleotide sequences, and the corresponding fluorescent label associated with the three particle types used in this work.

Spectral Code	Capture Probe*	Target	Target Labels**
111111	P1	T1	AF 555
101011	P2	T2	AF 680
110101	P3	---	---

* P1:ACTGTGTGATGAAGTTTGGTCAGTCGGCTTGTTATTATCTCGTGCTTGTA-3'
P2: TCCTGTAATGATCCAGGTGAGTGATATGCCATACATCCTAGATCCTTATA-3'
P3: TCTGGATAGTCATACGTCACCCTCGCTTAGGATCTATACTTACTATACTA-3'
**AF = Alexa Fluor; indicates the identity of the fluorescent dye attached to the target sequence (T1 or T2) that is complementary to the capture probe sequence indicated. N/A indicates that no target sequence was used; the capture probe for this particle type was included as a negative (non-specific binding) control for the other target sequences.

4.4.2 Spectral Code Extraction

The image stack was analyzed with a Matlab program that classified the individual pixels of each image into a group (representing each photonic code) after the work of Mansfield.[138] The sharp spectral peaks derived from the porous SiO_2 photonic crystals (Figure 4.1b) represent bits in a binary code,[90] with each microparticle having only one code, and therefore spectral unmixing methods for pixel classification were not required. Instead, each pixel associated with a microparticle was identified, decoded, and classified in the following sequence:

(1) An image was created showing the maximum light intensity at any wavelength in the reflectivity stack for each pixel. This image was then spatially top hat filtered with a disk structuring element slightly larger than the microparticle size, followed by morphological closing of the image with a smaller disk to give a mask identifying the locations of the microparticles. The pixel spectra were then background-corrected to allow for spatial non-uniformity of the illumination. Further masks were created that eroded the microparticle locations by 1-3 pixels.

(2) The spectrum of each pixel identified by these masks was scanned for reflectivity maxima above set height and width thresholds, and the wavelength and intensity of each spectral maximum was determined.

(3) Each code includes a peak at short wavelength that was used as a reference peak. The location of this first peak in the spectra of all the microparticle-associated pixels that showed at least four spectral peaks was 472 nm with a standard deviation of 13 nm (n= 6356). The location of each subsequent peak in the code was determined

relative to this peak, resulting in a set of relative peak position (RPP) values with much greater precision than the absolute peak positions. Thus, the standard deviations for the RPP ranged from 2.0 nm (second peak) to 3.2 nm (fifth and sixth peaks). The distributions of RPP were even less variable if pixels near the edges of the microparticles were discarded, Figure 4.2.

(4) Each pixel was decoded based on the number of reflectivity peaks and the values of each RPP. The RPP and the peak intensities were tested against predetermined acceptance criteria assigned to a particular code. The acceptance criteria consist of three parameters: the number of RPP values expected for the code, the upper and lower wavelength boundaries of each of the expected RPP values and an intensity threshold for each peak in the code. Pixels meeting these criteria were classified into one of the three microparticle code types. If a pixel did not meet all the predetermined criteria, then it was marked as invalid. In addition, most data reported in this paper are derived using masks in which microparticle locations have been eroded by 1 or more pixels. The spectral criteria combined with this spatial filtering were set to ensure there were no false classifications of single pixels based on the classifications of the surrounding pixels in the same microparticle. The spectral and spatial criteria used lead to a large number of pixels that are classified as invalid. However, within each microparticle the majority of pixels are classified correctly.

(5) Finally, the photonic codes were compared to the fluorescence result to determine true positive and true negative results. An indexed color image representing the results of the decoding algorithm applied to the reflectivity image

stack is shown in Figure 4.3C. Pixels decoded as 111111, 101011, 110101 are indicated as green, red, and blue, respectively. Pixels that fail the classification routine are assigned a grey value in the image, while background pixels are shown as black. The irregular object near the center of the images in Figure 4 was not associated with a photonic structure, and so pixels in this region have been excluded from the classification analysis.

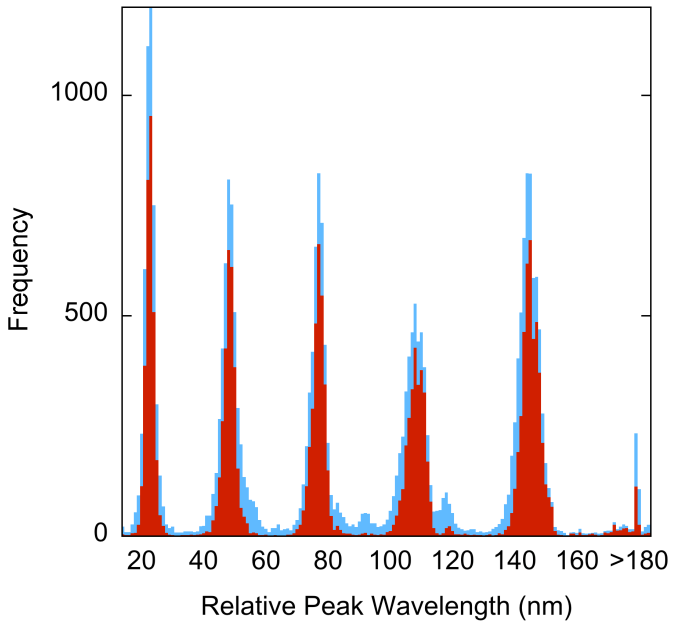

Figure 4.2 Distributions of the relative peak positions (RPP) for all pixels identified as belonging to the microparticles with no erosion (blue) and 3 pixel erosion (red) of the microparticle locations.

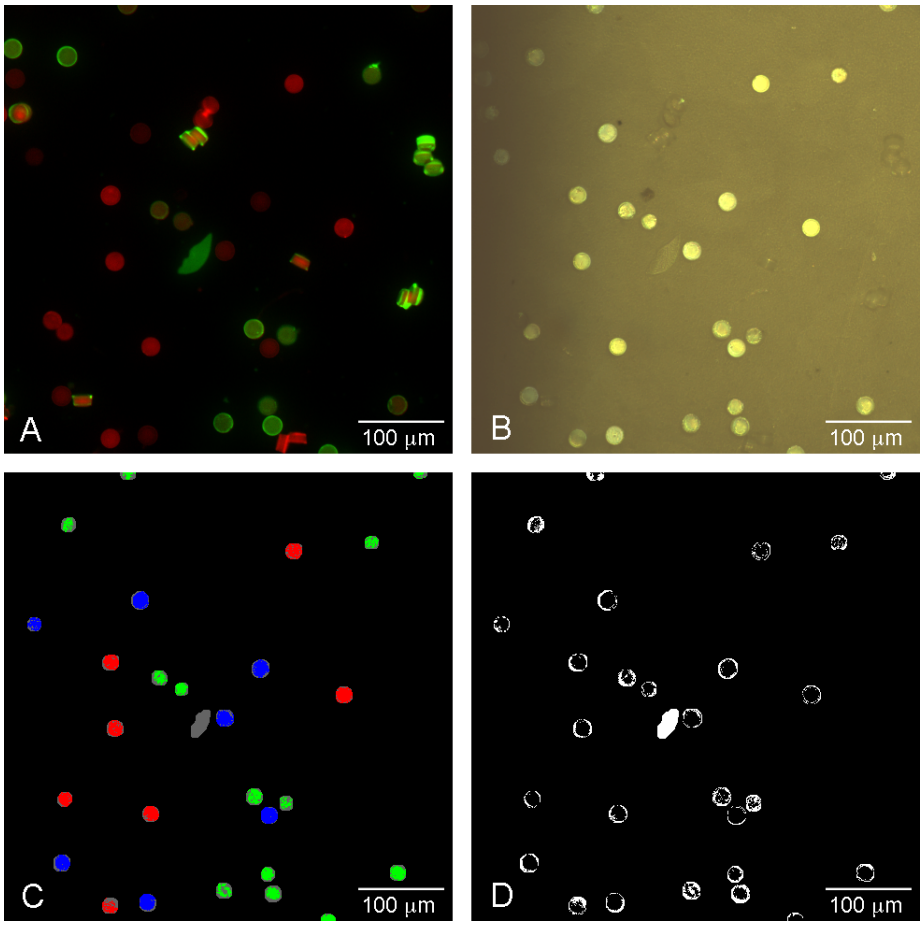

Figure 4.3 Microscope images of particle ensembles comparing results of fluorescence and reflectivity assays. (A) False color image of fluorescence measured from particle ensemble. The green and red colors represent the fluorescence intensity measured in the AF555 channel (Alexa Fluor 555, λ_{em} = 610 nm) and the AF680 channel (Alexa Fluor 680, λ_{em} = 710 nm) respectively. (B) Color reflectivity image constructed from the reflectivity image stack. (C) Indexed color image resulting from a decode of the reflectivity image stack after 1 pixel morphological erosion of the microparticle locations. Pixels decoded as 111111, 110101, and 101011 are represented as green, blue, and red, respectively. Pixels in the image that fail the decode algorithm are assigned to gray, while background pixels are black. (D) Image showing the positions of pixels that failed the decode algorithm when no morphological erosion is applied to the microparticles. Scale bar is 100 µm.

4.4.3 Comparisons with Fluoresce Assays

Figure 4.4 shows plots of the fluorescence at 610 nm (Alexa Fluor 555) and 710 nm (Alexa Fluor 680) measured for each microparticle-associated pixel, with the data points being coded based on the reflectivity spectrum at each pixel. The data in both plots show separation of the three code types, indicating that the method was able to correctly identify particle types under the conditions of a fluorescent oligonucleotide assay. The average intensity measured in each fluorescence channel for each particle type, the standard deviation, and the % coefficient of variance for the data are given in Table 4.2.

Pixels decoded as 111111 exhibited fluorescence intensity values that were highest in the Alexa Fluor 555 channel and low in the Alexa Fluor 680 channel (Figure 5). This is in agreement with expected results, because microparticles of code 111111 were functionalized with capture oligonucleotide sequence P1, whose complementary oligonucleotide target probe (T1) was labeled with Alexa Fluor 555 dye (Table 4.1). Correspondingly, pixels decoded as 101011 exhibited fluorescence intensity values that were low in the Alexa Fluor 555 channel and highest in the Alexa Fluor 680 channel (Figure 4.4). The 101011 microparticles were functionalized with capture oligonucleotide sequence P2, whose complementary oligonucleotide target probe (T2) was labeled with Alexa Fluor 680 dye (Table 4.1). Pixels decoded as 110101 exhibited fluorescence intensity values that were low in both fluorescence channels relative to pixels decoded as 111111 or 101011, consistent with their being functionalized with oligonucleotide P3, for which there was no fluorescently labeled complementary target sequence in the analyte solution. Because these results match the experimental design,

we have demonstrated that the immobilized probes and reflectivity codes are stable through the assay conditions and that the system is capable of detecting multiple analytes in a single sample.

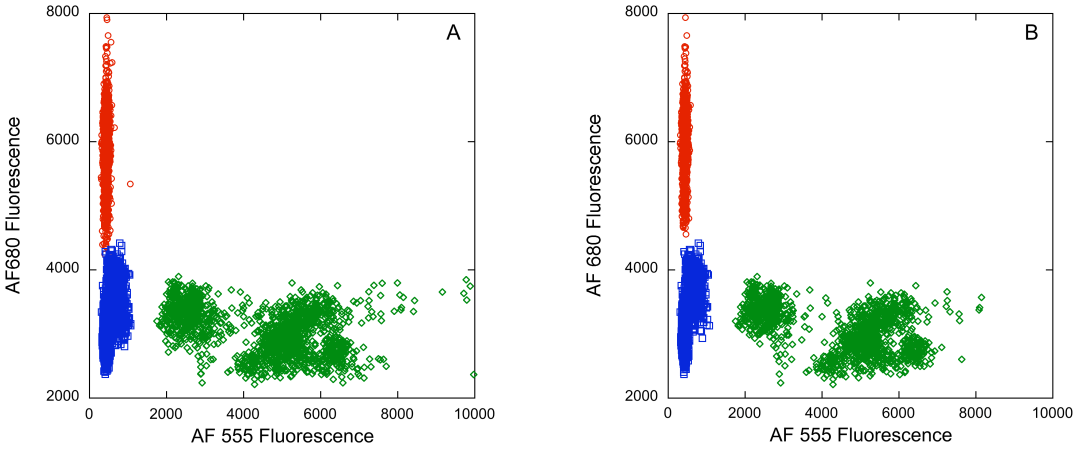

Figure 4.4 Scatter plots depicting the classification capability of the spectral decoding algorithm for microparticles that have had (A) 1 pixel eroded from their image edges and (B) 3 pixels eroded from their image edges. The fluorescence intensity measured in the AF680 channel (Alexa Fluor 680, λ_{em} = 710 nm) is plotted against the fluorescence intensity measured in the AF555 channel (Alexa Fluor 555, λ_{em} = 610 nm) for each pixel in the image of Figure 4A corresponding to a classified pixel. The data are represented with red circles, green diamonds, or blue square symbols for codes 101011, 111111, or 110101, respectively (see Table 1). The pixels decoded as 101011, 111111, or 110101 are distributed over 7, 13, and 7 individual particles, respectively.

Table 4.2 Average pixel intensities from each fluorescence channel for codes represented in **Figure 4.4**A.

Code	Channel	Intensity*	Stdv	% CV	Number of Pixels
111111	AF555	4475	1550	35	1619
111111	AF680	3068	360	12	
101011	AF555	448	44	9.8	1457
101011	AF680	5876	560	9.6	
110101	AF555	547	160	30	1637
110101	AF680	3230	440	14	

[a]14-bit scale, maximum value 16383

4.5 Conclusions

This work demonstrated a system that is capable of detecting multiple analytes contained in a single sample using spectrally encoded porous SiO_2 microparticles. The microparticles are stable under biological assay conditions and can be functionalized using silane chemistry. The photonic codes are identified by analysis of their wavelength-dependant reflectance properties, obtained simultaneously on an ensemble of particles by wavelength-resolved digital imaging. The codes are retained throughout the preparation and analysis process.

Two target oligonucleotides were conjugated with fluorescent dyes of different colors to provide an independent test of the classifications based on the photonic codes. In practice, a single dye could be used for all sequences because sequence identification is obtained from the reflectivity spectrum of the microparticle to which the sequence is attached. Thus, whether or not a microparticle has probe oligonucleotides complementary to the target oligonucleotide sequences is determined by observing which particles in the ensemble are fluorescent; the identity of the oligonucleotide on each of the fluorescent microparticles is then determined by decoding the reflectivity spectrum of that microparticle. The method could also be applied to proteomics assays using appropriately tagged fluorescent antibodies or other markers.

The decoding method used in this study is based on proven techniques to classify the spectral characteristics of multiple objects within the field of view of a digital imager. Therefore, analysis using the encoded microparticles described in this work could readily be automated using existing image analysis approaches for massively parallel, high throughput bioassays.

Chapter four, in part, is a reprint (with co-author permission) of the material as it appears in the following publication: Meade, S. O.; Chen, M. Y.; Miskelly, G. M.; Sailor, M.J., Multiplexed DNA Detection Using Spectrally Encoded Porous SiO2 Photonic Crystals Particles, *Analytical Chemistry* 2009, 81, 2618-2625. Copyright © 2009, American Chemical Society. The author of this dissertation is the co-author of this manuscript.

CHAPTER FIVE

MULTISTAGE INSULIN RELEASE USING DOUBLE-LAYER MESOPOROUS SILICA NANOTSTRUCTURES

5 Multistage Insulin Release using Double-Layer Mesoporous Silica Nanostructures

5.1 Abstract

Many nanomaterials have been interrogated for intravascular carrier to increase drug release efficacy. However, simultaneous targeting as well as avoiding biological barriers have become exceedingly difficult to overcome. Here, a multilayer porous silica matrix was constructed with a tunable neck layer that can control insulin release profiles and a reservoir layer that can concentrate up to 530 times the loading concentration (1mg/ml). The main objective here is to provide a new strategy for encapsulating, protecting, and delivering molecules in a time- controlled fashion. Multistage insulin release profile is found to be a function of the pore dimension. This approach offers a potential route for sustained release of a drug with controllable release profile in a rigid, multi-tier nanostructure with minimal preparation steps.

5.2 Introduction

Growing knowledge on diseases and the biological system has led to the development of an immense number of new drugs and potential treatments, such as gene and peptide therapies. Considerable effort has then been focused on designing effective delivery vehicles for some otherwise insoluble or unstable therapeutic compounds. Patients also receive higher dosages to compensate for drug loss during circulation. However, many drugs have limited therapeutic windows, increased risk of unwanted side effects, or toxicity with higher dosage that have prevented their

availability to patients. Additionally, biological barriers such as enzymatic degradation and phagocytosis have also posed problems for drug delivery systems. Therefore, formulation of a delivery system that can protect while hosting an unstable drug with controlled release rate within the therapeutic window has motivated researchers to optimize delivery efficacy and to explore new approaches. Recently, the promise of nanomedicine has shed some light on the design of potential delivery systems. The interest in nanoscale materials in medicine stems from the fact that their properties (optical, chemical, mechanical, etc.) can be tailored based on their size, composition, and structure orders to meet these needs.[139-141] Over the last few decades, different materials such as polymers,[142, 143] liposomes,[144] and mesoporous silica matrices[18, 112] have been investigated as potential drug carriers. Of which, mesoporous materials possess many desirable features that are ideal for controlled and sustained drug delivery. The unique attributes of mesoporous materials include defined, ordered pore networks allowing fine tuning of drug loading, high pore volumes for hosting larger therapeutic dosages, and chemically functionalized surfaces providing additional control over drug loading and release kinetics.[15, 112] Over the last decade, mesoporous silicon or silica matrices have been developed as a vehicle to host and transport biomolecules and drugs, but with little data presented for controlled drug release profiles.[14-18, 145-150] Various strategies have been implemented to allow more control over the release profiles. Some of the more attractive approaches involve capping the matrix with a polymeric material or blocking the pores with linkers and gating species that is responsive to stimuli such as pH and temperature.[150-153]

While these approaches have shown to increase control, additional preparation and polymerization steps pose new obstacles including possible inactivation of proteins, and compression within the structures.[143, 154] More specifically, the extent of penetration and the effect on polymer expansion within the porous matrix can lead to undesirable physical changes of the material. A more attractive approach is to utilize the physical structure of mesoporous material to control molecule release behavior, as a multistage delivery system.[15] In this chapter, a multilayer porous silica ($pSiO_2$) structure was constructed with a small neck layer, with a diameter on the order of the dimension of the drug, and used to study the effect of different pore sizes on drug release profiles, offering an alternative route for controlled, multistage release of a drug without extraneous capping material. A second layer was constructed below the neck layer to increase the drug loading capacity of the carrier. The main advantage of this approach is the uniform and biologically inert silica structure that is capable of controlled protein/drug delivery with minimal preparation steps, shielding molecules/drug from biological barriers.

5.3 Experimental Methods

5.3.1 Fabrication of Porous Silica Carrier

Porous Si samples were prepared by anodization of highly doped p-type silicon wafers (p++, <100> orientation) with a resistivity ranging from 0.83 to 0.85 mΩ cm in an ethanolic hydrofluoric acid solution (3:1 v/v 48% aqueous HF : ethanol). Si chips with an exposed area of 1.2 cm^2 were contacted on the back side with a strip of aluminum foil and mounted in a Teflon etch cell. Samples were then electrochemically

etched in a two-electrode configuration using a platinum mesh counter electrode. Double-layer samples were prepared by application of a two-step current density waveform. Samples were rinsed three times with ethanol and then dried with nitrogen gas. Freshly etched samples were then thermally oxidized in a tube furnace (Lindberg/Blue M) at 750 °C for 1h in air and then allowed to cool to room temperature.

5.3.2 Physical Characterization of Porous Silica Carrier

Freshly etch porous silicon layer thickness was examined with a Philip XL 30 environmental scanning electron microscopy operating in second electron mode. Accerlating voltages of 10 to 20 keV.

Nitrogen adsorption-desorption isotherms of triplicate porous Si samples were recorded at 77 K using a Micromeritics ASAP 2020 volumetric apparatus. Prior to the adsorption experiment, porous Si samples were degassed overnight. The surface area of the sample was measured by the BET (Brunnauer-Emmett-Teller) method, which yields the amount of adsorbate corresponding to a molecular monolayer. The pore dimensions were determined using the BdB (Broekhof-de Boer) method from the nitrogen adsorption curve.[120-122] Porosity was characterized using the nondestructive spectroscopic liquid infiltration method (SLIM) as described previously.[155]

5.3.3 Insulin Preparation and Loading

Insulin was purchased from Sigma-Aldrich (Cat. No. I6634). For loading solution, 1 mg/mL of insulin was dissolved in 5mM pH 3.8 acetic acid buffer solution

with ionic strength ~ 150 mM.[156] The solution was slowly agitated for 1 h to allow equilibration of protein prior to filtration with 0.22 μm filters (Millipore, Cat. No. SLGV033RS).

For the loading experiment, 1.5 mL of filtered insulin solution was added into a glass vial containing a porous SiO_2 sample and slowly agitated for 12 h.

5.3.4 Release Study

Insulin impregnated porous SiO_2 samples was incubated in physiological conditions by performing all the experiments at 37 °C at pH 7.4 in 1.5 mL Dulbecco's phosphate-buffered saline. Fresh solution was replaced ever 2 h for 12 h. Insulin was quantified using micro-BCA (bicinchoninic acid) assay kit obtained from Thermo Scientific (Cat. No. 23235). After the release experiment, insulin was recovered by dissolving porous SiO_2 in 1mL of 1M sodium hydroxide solution overnight followed by neutralizing the solution with 1mL of 1 M hydrochloric acid.[157]

5.4 Results and Discussion

5.4.1 Insulin

Daily subcutaneous injection of insulin decreases the quality of life for diabetic patients. Various routes have thus been investigated to provide more convenient ways to ease patients' lives. However, insulin agglomeration caused by pH, ionic strength, agitation, and surface hydrophobicity of the environment or the carrier leading to inactivity has presented hurdles for the development of insulin delivery systems.[156, 158, 159] A transporting material with the ability to protect insulin from agglomeration and

provide slow release of insulin is thus desirable. A wide range of applications using $pSiO_2$ nanostructures has shown its potential as an excellent, alternative method for sustained release of insulin.[14, 15] There are three attributes of this material that are most applicable for insulin delivery. First, hydrophilic silica surfaces have been demonstrated to provide better stability for insulin.[159] Second, the neck layer acts not only as a rate regulator but also as a sieving or segregating film to allow non-aggregated insulin to pass through and protect insulin from the environment. Lastly, the biodegradability and biocompatibility of these $pSiO_2$ materials have been demonstrated over the years for drug delivery applications.[18, 160, 161]

5.4.2 Physical Properties of Multilayer Mesoporous Nanocarrier

A double-layer sample was designed with a reservoir and a size-controlled neck, as shown in Figure 5.1a. Porous SiO_2 carriers were prepared in two steps. First, a double layer Si sample was prepared by electrochemical etching a two-step current density, with a smaller current density followed by a larger current density step. In order to perform a systematic comparison, dimensions of the bottom layer (reservoir) were made with constant average pore diameter ~38 nm, as illustrated in Figure 5.1b, and film thickness ~8.8 μm for each double layer structure. The porosity of the bottom layer was ~79 % using the nondestructive spectroscopic liquid infiltration method (SLIM) described previously.[162] As pointed out above, the top layer is used to control the multistage release, whereas, the bottom layer is constructed to serve as a reservoir and accommodate greater overall drug loading. For this purpose, the neck was fabricated to have less than half of the thickness of the reservoir. Figure 5.1c is the

cross-sectional-view of the scanning electron microscope (SEM) image of a double layer sample showing a thin neck layer (~3.3 - 4.2 μm) followed by a thick bottom layer (~8.8 μm). Furthermore, Figure 5.1d provides a SEM image at the intersection of the structure illustrating the difference in the pore morphology between the two layers. Following the fabrication of the multilayer structure, the porous Si sample was thermally oxidized creating a thin layer of surface oxide that is negatively charged above pH 2 solutions.[163] As reported, insulin (isoelectric point ~ 5.3) is prone to agglomeration when in contact with uncharged surfaces and in a solution near its isoelectric point.[158, 159] To address these conditions specifically, negatively charged $pSiO_2$ pore walls allow an electrostatic loading of dissolved and positively charged insulin molecules in pH 3.8 buffer solution.

The aim of this study is to investigate insulin release from a double-layer nanostructure as a function of pore size. For this purpose, multilayer structures were designed to possess similar total porous volume. The dimension or the amount of total Si removal can be manipulated based on several parameters including substrate doping densities, HF concentration, current density, and etch duration.[91] Assuming a linear silicon dissolution rate with respect to current density and keeping everything else consistent, two parameters, namely, current density and etch duration, were tuned for the preparation of double-layer structures. Three different current densities (20.8, 62.5, and 104 mA/cm^2) were chosen with estimated etching durations (360, 120, and 72 s, respectively) to remove similar amount of Si from a substrate with area ~ 1.2 cm^2. To characterize the samples, single layer $pSiO_2$ structures representative of individual neck layer were prepared in triplicates for Brunauer-Emmett-Teller isotherm (BET) analysis.

Values presented in Table 5.1 show the physical properties of the prepared samples. The dashed line in Table 5.1 implicates that the pore dimensions have fallen out of the regime where the BET analysis can provide a meaningful estimation. For the three double-layer structures, a small deviation in volume is observed.

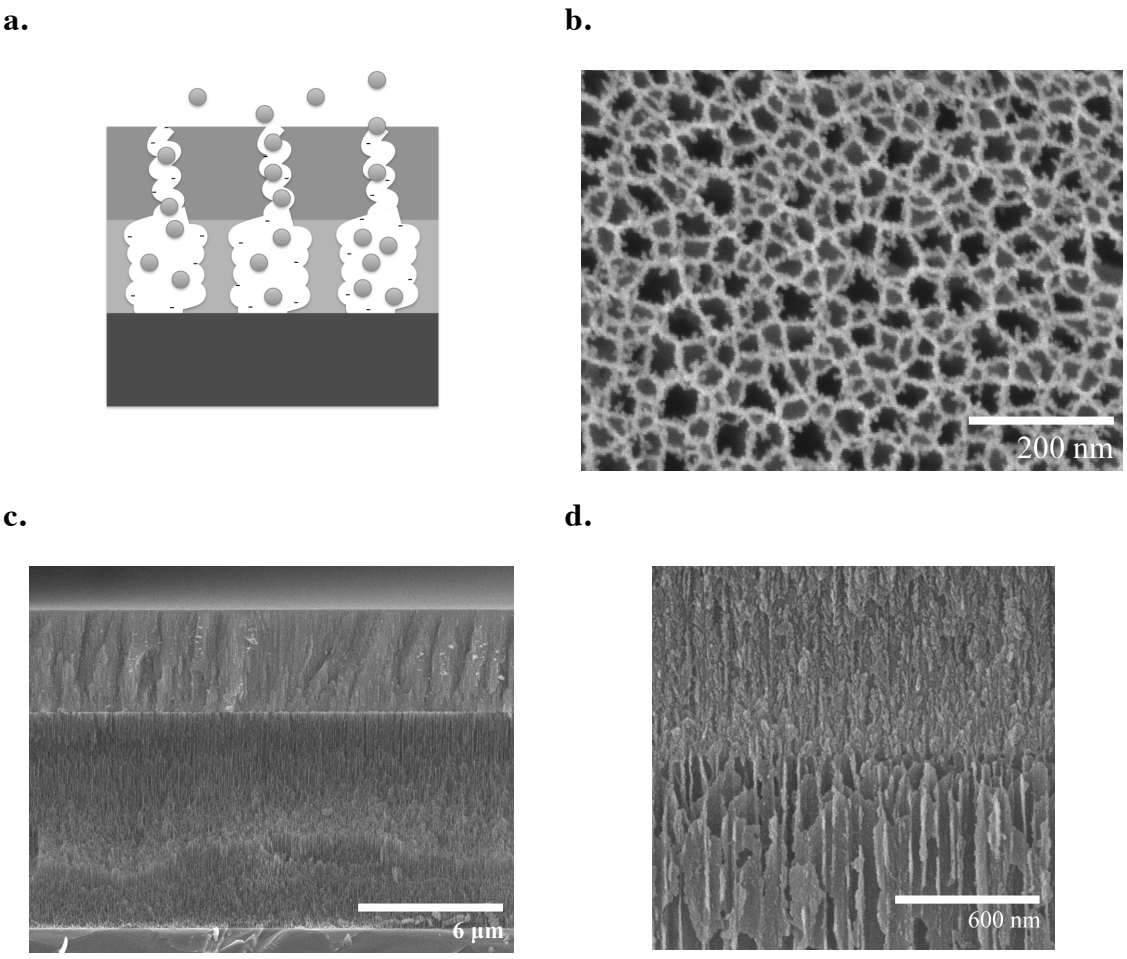

Figure 5.1 a. Schematic of the $pSiO_2$ double layer nanostructure used in this study. **b.** A scanning electron microscope (SEM) image of the top (plan) view of a single layer film, representative of the reservoir layer. Average pore diameter estimated ~ 38 nm. **c-d.** Cross-sectional and closed up SEM images of a two layer nanostructure sample.

Table 5.1 Porous Silica Characterizations.

Current density (mA/cm^2)	Pore Size (nm)[a]	Pore Size (nm)[b]	Porosity (%)[c]	Volume,$x10^{-3}$ (cm^3/chip)[a]	Surface Area (mm^2/chip)[a]
20.8	7	8 ± 2	60.7 ± 0.2	0.265	0.158
62.5	9	9 ± 2	62 ± 2	0.274	0.138
104	11	12 ± 4	67 ± 2	0.292	0.110
375	---	38 ± 9	79 ± 3	---	---

[a.] Values are obtained from single layer samples in triplicates and calculated using Brunauer-Emmett-Teller isotherm theory.
[b.] Pore sizes are estimated from scanning electron microscope.
[c.] Porosities are obtained using the nondestructive spectroscopic liquid infiltration method. Error corresponds to the standard deviation of the measurements.

5.4.3 Drug Loading Experiment

Although with slight deviations in the total volume for the three multilayer structures, the difference in the total amount of insulin loaded per chip in each double-layer structure is almost indistinguishable, as shown in Table 5.2, after a 12-hour loading period. For the loading experiment, ~1 mg/ml insulin was introduced to the single layer and three double-layer $pSiO_2$ chips in pH = 3.8 buffer solution for 12 hours. The quantity of loaded insulin was estimated by measuring insulin concentration in the loading solution before and after loading, using a bicinchoninic acid (BCA) protein assay. As pointed out from the previous section, insulin loading was facilitated by electrostatic adsorption. This approach loaded a concentration that is nearly 300 times of the original concentration. Furthermore, more insulin was loaded into the single layer sample that resembles the reservoir layer as compared to the other three multilayer structures. This difference is likely contributed to hindered insulin diffusion due to the size of the pores that are close to the dimension of the insulin. Another valuable attribute of this approach is the increased total surface area within the nanostructure, shown in Table 5.2. The smaller pores with larger surface areas allow the drug of interest to be in close proximity of the pore walls providing more interaction with the pore surface. Here, three double-layer structures were constructed and loaded with a similar amount of insulin to facilitate a systematic study of insulin release as a function of pore size. The larger surface areas for the neck layer also provide an enhanced control for the release of the drug of interest.

Table 5.2 Insulin Loading Data.

Current density used to prepare samples (mA/cm^2)	20.8[D]	62.5[D]	104[D]	375[S]
mg insulin loaded per g of Si[a]	330 ± 30	410 ± 48	440 ± 30	910 ± 55
mg insulin loaded per chip[b]	310 ± 28	360 ± 41	350 ± 24	440 ± 27
mg insulin loaded per mL[c]	270 ± 24	320 ± 37	320 ± 21	530 ± 32

[D.] Triplicate double layer samples.
[S.] Triplicate single layer samples.
[a.] Assuming the true density of SiO_2, 2.2 g per cm^3.
[b.] Each chip was ~1.2 cm^2.
[c.] Volume of the porous layer was estimated using the porosity of the sample obtained from the nondestructive spectroscopic liquid infiltration method.

5.4.4 Multistage Insulin Release

In a solution with a pH greater than its isoelectric point, insulin exhibits a slightly negatively charged surface that experiences repulsion from the negatively charged $pSiO_2$ walls. After the 12-hour loading period, each insulin-impregnated chip was rinsed with phosphate buffered saline (PBS) to clean off loosely bound insulin prior to each release study. The solution was saved in order to account for the total amount of loaded insulin. Subsequently, drug release experiments were performed by adding 1.5 ml of PBS to the insulin containing sample and incubation at 37 °C. The solution was collected and replaced with new PBS solution every two hours, and the amount of insulin release was quantified using micro BCA assay. A blank double-layer $pSiO_2$ sample was used as a control with 1.5 ml of PBS solution collected every two hours. The result confirmed that dissolved silica did not interfere with the micro BCA protein assay. Figure 5.2 illustrates the release profile of insulin in a single layer and three double-layer structures as a function of pore size. The y axis, % insulin released, is the total amount of released insulin up to time t divided by the total amount of insulin loaded into the nanostructure. In comparison, the single layer reservoir with 38 nm pore diameter exhibits the greatest initial burst release, nearly 100 % of insulin embedded in the structure was released after 4 hours. For double-layer structures, insulin also exhibits burst release, however, with a decreasing initial burst as the top pore size decreases with more than 40 % of insulin retained in the matrix after 12 hours. Figure 5.2 suggests that the additional neck introduces a new strategy to reduce the initial burst release. Furthermore, the release profiles for all the samples exhibits a multistage release, with initial burst release followed by slow, constant release of molecules.[161]

After the release study, the insulin containing $pSiO_2$ film was dissolved using 1 M sodium hydroxide followed by adding 1 M hydrochloric acid to neutralize the solution. The solution was then collected to determine the amount of insulin remained in the nanostructure. This value was added to the total amount of released insulin after 12 hours and was found to be in good agreement with the total amount of insulin determined previously using BCA protein analysis. The release profile, as demonstrated in Figure 5.2, demonstrates a reducing initial burst release with decreasing pore diameters of the neck layer, offering a potential route for sustained release of insulin with controllable release profile in a rigid, double-layer nanostructure.

Figure 5.3 illustrates concentration profiles of free insulin as a function of time and pore diameter. With decreasing pore diameters, slower diffusion rates were observed even with similar initial concentration gradients and with greater electrostatic repulsion through larger surface interaction. This implicates that pore size plays the predominant role in insulin diffusion from $pSiO_2$. This effect, however, becomes less prominent as the pore diameter increases as stated by the hindered transport theory on charged particle diffusion within a charged membrane.[164]

Up until now, single layer porous silicon films were constructed with large pore diameters to accommodate the dosage requirement for the drug of interest.[14, 15] In order to obtain more control on the release profile of a particular drug, additional preparation steps are usually necessary to achieve desirable release rate. Figure 5.2 and Figure 5.3 show the degree of control one can gain by adding a restricting top layer to significantly reduce initial burst release and possibly slowed down the release rate. The smallest pore (~ 8nm) retained most of its content with an almost steady release of

insulin comparing to the reservoir sample, which shows over 100 μg/ml of free insulin after 2 hours. It is also important to look at the actual amount of insulin that was released into the free solution with respect to the physiological levels of insulin. The dashed lines in Figure 5.3 indicate the lowest basal concentration (~3 μg/ml) and the highest secretion level (~ 100 μg/ml) during hyperglycermia for insulin.[165] These values were calculated based on hexameric insulin. In comparison, the samples were able to deliver concentrations that are within the physiological levels for the first few hours. By fine-tuning the pore dimensions and loading conditions, these structures can offer a powerful alternative for sustained release of insulin within its therapeutic window in a desirable delivery time frame.

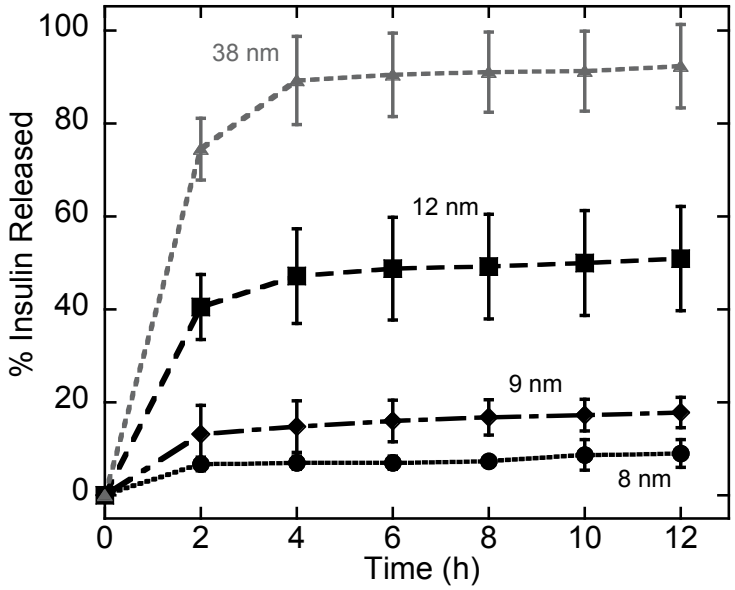

Figure 5.2 Multistage insulin release profiles as a function of pore size. Traces labeled 8 - 12 nm are double-layer structures with the indicated pore size as the diameter of the neck layer. 38 nm pore is the single layer reservoir with the same morphology as the bottom layer of the other three structures shown here. The y axis, % insulin released, is the accumulated amount of released insulin up to time t divided by the total amount of insulin loaded into the nanostructure.

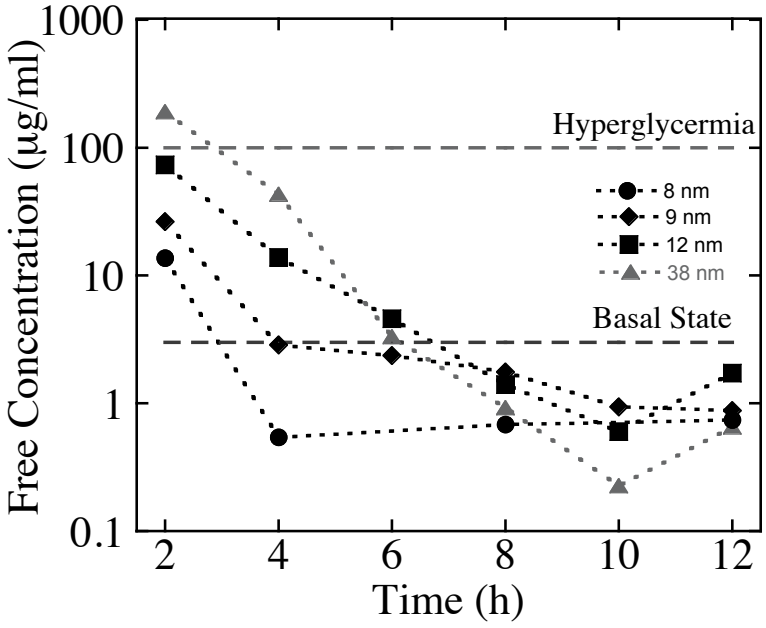

Figure 5.3 Concentration profiles of released insulin in PBS solution for 12 hours. Free insulin concentration profiles of three double-layer and a single layer (38 nm) structures are presented here. The dashed lines indicate the lower limit of insulin concentration in the basal state and the upper limit of insulin secretion during hyperglycermia. Physiological values are calculated based on literature values[165] assuming insulin is in the hexamer form.

5.5 Conclusions

In summary, double-layer porous silica ($pSiO_2$) matrices were prepared to study the release of insulin as a function of their tunable neck dimensions, as a multistage drug delivery host. Insulin, a widely used hormone for the treatment of type 1 and 2 diabetes, was dissolved and loaded into the double-layer structures. The negatively charged $pSiO_2$ matrix allows the positively charged hormone to be concentrated within double-layer porous material by a factor ~ 300 times of the original concentration of insulin in solution. A similar amount of insulin was loaded into each multilayer structure. A systematic study of insulin release as a function of pore size demonstrated differential initial burst release profiles. Although below the physiological levels, smaller pores present more steady release of insulin and possibly more control due to the larger surface area and closer pore wall and drug interaction range. Furthermore, the neck can act as not only the rate limited layer but also as a filtration membrane. Double-layer structures provide an attractive method to host, protect, as well as deliver the drug of interest in a more controllable fashion. The result of this study will provide a new direction for controlled and sustained drug delivery using rigid nanostructures with minimal preparation steps.

Chapter five, in part, is a reprint (with co-author permission) of the material as it appears in the following publication: Chen, M. Y.; Diep, V.; Wu, C.; Secret, E.; Cunin, F.; Andrew, J; Sailor, M.J., Multistage Insulin Release using Double-Layer Mesoporous Silica Structures. *manuscript in preparation.* The author of this dissertation is the primary author of this manuscript.

CHAPTER SIX

CHARGE-GATED TRANSPORT OF PROTEINS IN NANOSTRUCTURED OPTICAL FILMS OF MESOPOROUS SILICA

6 Charge-Gated Transport of Proteins in Nanostructured Optical Films of Mesoporous Silica

6.1 Abstract

The admission into and diffusion through nanoscale pores by molecules is a fundamental process of great importance to biology and separations science. Systems (e.g., chromatography, electrophoresis) designed to harness such processes tend to remove the separation process from the detection event, both spatially and temporally. Here we describe the preparation and characterization of thin optical Fabry-Pérot films of mesoporous silica ($pSiO_2$) that can detect protein infiltration by optical interferometry, which probes the separation process in real time and in the same ultrasmall physical volume (5 nL). Admission of a protein into the pores is controlled by the diameter (~50 nm) and the surface charge of the pores, and both the rate and the degree of protein infiltration is a function of solution pH. Test proteins bovine serum albumin (BSA, 66kDa), bovine hemoglobin (BHb, 65kDa) and equine myoglobin (EMb, 18kDa) are admitted to or excluded from the nanophase pores of this material based on their size and charge. The rate of protein transport within the pores of the $pSiO_2$ film is slowed by 3 orders of magnitude relative to the free-solution diffusion values, and it is maximized when pH = p*I*.

6.2 Introduction

Membranes with abiotic micro- or nanometer sized pores have been harnessed for sensing,[51, 166] filtration,[27] controlled release and gating experiments.[167, 168] They are

usually more stable and predictable compared to biological pores,[169] and they provide experimentalists with a range of synthetic alternatives to control analyte transport behavior, sensitivity, and specificity. Porous silicon (pSi) membranes offer a versatile platform for studies of protein transport and binding: the porous nanostructure can be controlled during synthesis to yield a range of pore sizes, and optical structures can be incorporated into the films to provide sensitive, label-free quantification of biomolecular binding.[170] Unlike surface plasmon or other label-free biosensor devices, the three dimensional control of nanostructure that is achievable in electrochemically prepared pSi devices allows spatially resolved molecular separation simultaneous with the detection event that can improve the fidelity of sensing in complex media.[28, 109, 171] The ability to separate large molecules such as proteins based on size has been demonstrated in pSi membranes,[20, 27, 28, 171] and the native negative charge[172] on the surface of oxidized porous Si ($pSiO_2$) has been used to enhance the binding of proteins within the pores.[14, 25] Although both pore size and the charge on the pore walls should have an effect on transport and binding of proteins, the transport of charged proteins within such membranes has not been studied. In particular, pH exerts a pronounced effect on the charge of a protein and on its rate of transport through very small, charged pores.[169, 173, 174] In addition, the time dependence of protein transport in mesoporous SiO_2 films has been observed but not addressed or quantified.[25]

Here, a mesoporous $pSiO_2$ film is constructed and transport of three test proteins is quantified as a function of pH. A relatively small pore size is chosen for these experiments (50 nm), in order to enhance protein-pore wall interactions and slow diffusion rates to experimentally accessible timescales of 1-30 min. The rate and extent

of biomolecule infiltration is observed without the use of fluorescent or radioactive labels by harnessing the optical interference property of the film, which provides a real-time measure of the mass of protein in the film. We find that protein diffusion within the nanostructure is influenced by electrostatic interactions between the negatively charged pore walls and the pH-dependent charge on the surface of the protein, providing a means to determine protein isoelectric point (p*I*).

6.3 Experimental Methods

6.3.1 Materials

Aqueous HF (48%) and ethanol (99.9%) were supplied by EMD and Gold Shield Chemical Company, respectively. Porous silicon samples were prepared from highly doped p-type Si with resistivity ranging from 0.0008-0.001 Ω-cm (polished on the (100) face, boron doped, from Siltronix Corp). Bovine serum albumin (BSA, 66kDa) was obtained from CalBiochem (Cat. No. 12657). Bovine hemoglobin (BHb, 65kDa) and equine myoglobin (EMb, 18kDa), were obtained from Sigma-Aldrich, Cat. No. H2500 and M0630, respectively. All the proteins were used as-received without further purification. 5mM buffer solutions were prepared by mixing ultrapure (18 MΩ) water with monobasic sodium phosphate (Cat. No. S369-500 from Fisher), glacial acetic acid (Cat. No. AX0073-75 from EMD Chemicals), or Tris (tris(hydroxymethyl) aminomethane, Cat. No. BP152-500 from Fisher Scientific) depending on the pH and its buffer capacity. Desired pH values were then adjusted by adding a small amount of HCl or NaOH. The ionic strength of the prepared buffer solutions ranged from 0.001 to 0.15 M.

6.3.2 Porous Silicon Preparation and Characterization

Porous silicon samples were anodically etched in a 3:1 solution of aqueous 48% HF: ethanol. Si chips with an exposed area of 1.2 cm^2 were contacted on the back side with a strip of aluminum foil and mounted in a Teflon etch cell. Samples were then electrochemically etched in a two-electrode configuration using a platinum mesh counter electrode. Single-layer samples were prepared by application of a current density of 417mA/cm^2 for 32 s. Samples were rinsed three times with ethanol and then dried with nitrogen gas. Porosity was characterized using the nondestructive spectroscopic liquid infiltration method (SLIM) as described previously.[155]

6.3.3 Thermal Oxidation

Porous silicon samples were thermally oxidized in a tube furnace (Lindberg/Blue M) at 750 °C for 1h in air and then allowed to cool to room temperature.

6.3.4 Interferometric Reflectance Spectra Collection and Data Processing

Reflectance spectra were recorded with an Ocean Optics USB-4000 CCD spectrometer coupled to a bifurcated fiber optic cable. A tungsten halogen light source was used to illuminate the surface of the sample via one arm of the bifurcated fiber. Both the spectral acquisition and light illumination were performed along an axis normal to the surface of the $pSiO_2$ sample. Effective optical thickness (EOT), defined here as the value 2nL (where n = average refractive index and L = sample thickness in

nm), was obtained from the Fast Fourier Transform (FFT) of the acquired reflectance spectrum as previously described.[117] In this work the percent change in *nL* is defined as $(nL_a\text{-}nL_b)/nL_b$, where nL_a is the value obtained in the presence of analyte and $nL_{\mathbf{b}}$ is the baseline value obtained in the pure buffer of interest.

6.3.5 Time-Resolved Biosensing Experiments

Buffer solutions ranging in pH from 4.2 to 7.5, with ionic strength 0.01M, were used in the experiments to determine the p*I* of each test protein. Buffer solutions (pH 4.2, 4.7, and 7.5) with ionic strengths ranging from 0.002 to 0.15M were used in the experiments quantifying the electrostatic interaction between BSA and $pSiO_2$. A custom-designed flow cell system[175] fitted with an optically transparent window to facilitate acquisition of reflectance spectra was used. In a typical experiment, spectra were acquired every 30s and an initial baseline was established in a given buffer solution (flow rate ~0.5mL/min). A solution containing 5mL of the protein of interest (1mg/mL), dissolved in the same buffer, was then introduced to the flow cell (flow rate ~0.5mL/min) and spectral data were acquired for 1 hr. The buffer solution was circulated in a closed loop during data acquisition (total solution volume = 5 mL).

6.3.6 Protein Characterization

Zeta potential and hydrodynamic diameter of each protein was determined by dynamic light scattering (DLS) using a Malvern Zetasizer. Solutions containing 2mg/mL of each protein were measured. BHb and EMb were measured before and after filtration through a 100-nm syringe filter (Millipore, Cat. No. SLVV033RS). The

p*I* of each protein was determined using IEF gel electrophoresis (Invitrogen, Cat. No. EC6655A).

6.4 Results and Discussion

6.4.1 Protein Characteristics and Surface Interactions

The surface charge on a protein is determined by the chemical identity of the exposed residues and by the pH of the solution. The charge on a protein can be characterized by its p*I* value; when p*I* = pH, the net ionic charge on the protein is zero. Three proteins were chosen for the present study: bovine serum albumin (BSA), bovine hemoglobin (BHb), and equine myoglobin (EMb). Size and p*I* data are summarized in Table 6.1. The surface of $pSiO_2$ has a net negative charge at pH > 2 (references [25, 176, 177]), and electrostatic attractions will cause a positively charged protein to nonspecifically bind to this surface. Previous work with bovine serum albumin (BSA),[178, 179] protein A,[25, 109, 176] immunoglobulin G (IgG),[14] and other proteins[180, 181] have taken advantage of these electrostatic interactions to concentrate the protein on the inner pore walls of $pSiO_2$. The ability of a $pSiO_2$ film to act as a sensitive, label-free interferometric sensor provides a means to systematically study these electrostatic interactions, and in turn, determine the p*I*s and nanoscale transport properties of the proteins in real time.

Table 6.1 Proteins properties.

Protein	Molecular Mass (kDa)	Dimensions (nm)[a]	Hydrodynamic radius (nm)[b]	pI[c]
bovine serum albumin (BSA)	66	14 x 3.8 x 3.8 (reference [182])	7.1	4.7 (reference [183])
bovine hemoglobin (BHb)	65	6.3 x8.4 x 5.4 (reference [184])	7.4	6.8 (reference [185])
equine myoglobin (EMb)	18	4.5 x 3.5 x 2.5 (reference [186])	4.2	6.7,7.3 (reference [183, 187])

[a]From crystallographic measurements as referenced.
[b]Dynamic light scattering measurements of non-aggregated proteins at pH 7.5
[c] Literaure values as referenced

6.4.2 Physical and Optical Characteristics of Porous Silica Sensors

The $pSiO_2$ sensors were prepared in a two step procedure: first, a mesoporous Si sample was generated by electrochemical etch of single crystal Si, generating a 5.7 μm thick porous film of porosity 80% and average pore diameter 50 nm. Representative cross-sectional and plan-view SEM images are presented in Figure 6.1. The pores in this material are oriented preferentially in the <100> direction, which is perpendicular to the face of the wafer. Second, the porous Si sample was subjected to thermal oxidation, which generates a layer of surface oxide on the pore walls. Silicon dioxide or silica is commonly used as a matrix for microarray bioassays[188, 189] and as a stationary phase in chromatography[190] due to its stability, biocompatibility, and convenient surface modification chemistry. In the present case, the oxide provides a stable, negatively charged surface for the entire pH range studied (4-7).

The principle of operation for label-free biosensing with $pSiO_2$ films derives from the optical interference spectrum (Fig. 1c). The interference fringes depend on the quantity nL, where n is the average refractive index of the porous layer and L is its thickness. The value nL is determined from the Fabry-Pérot relationship, $m\lambda = 2nL$, where λ is the wavelength of maximum constructive interference obtained from the reflectivity spectrum and m is the spectral order of a particular interference fringe maximum.[25] The n values were determined by Fourier transform of the optical reflectivity spectrum (Fig. 1d), as previously described.[191] When immersed in a buffer solution, the value of n corresponds to a nonlinear average of the index of the $pSiO_2$ matrix and the buffer. All proteins have a refractive index that is larger than that of

water, so infiltration of protein usually results in an increase in the measured value of nL.

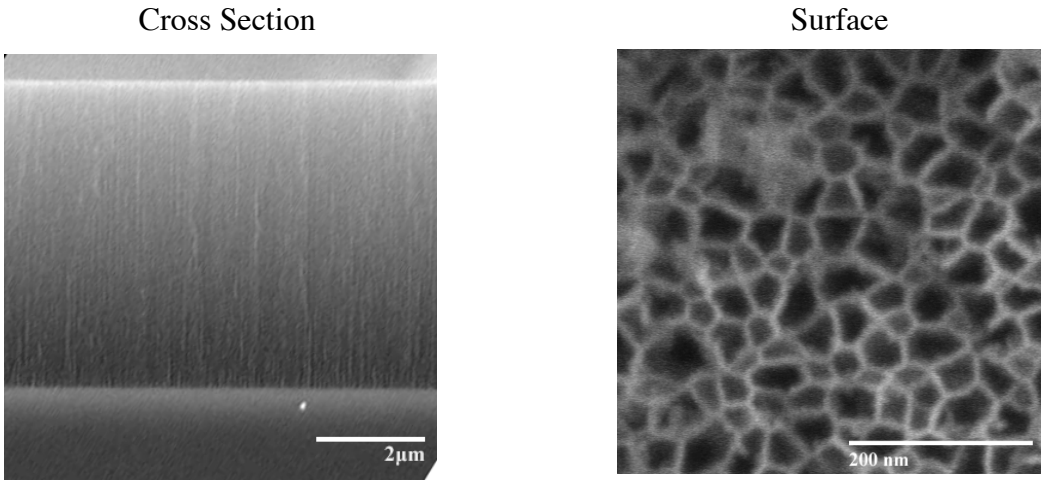

Figure 6.1 Morphology of $pSiO_2$ sensors. Representative cross-sectional (Left) and plan-view (Right) images of a porous Si sample obtained prior to thermal oxidation. Sample thickness is 5.7 μm, with a porosity of 80% and average pore diameter 50 nm.

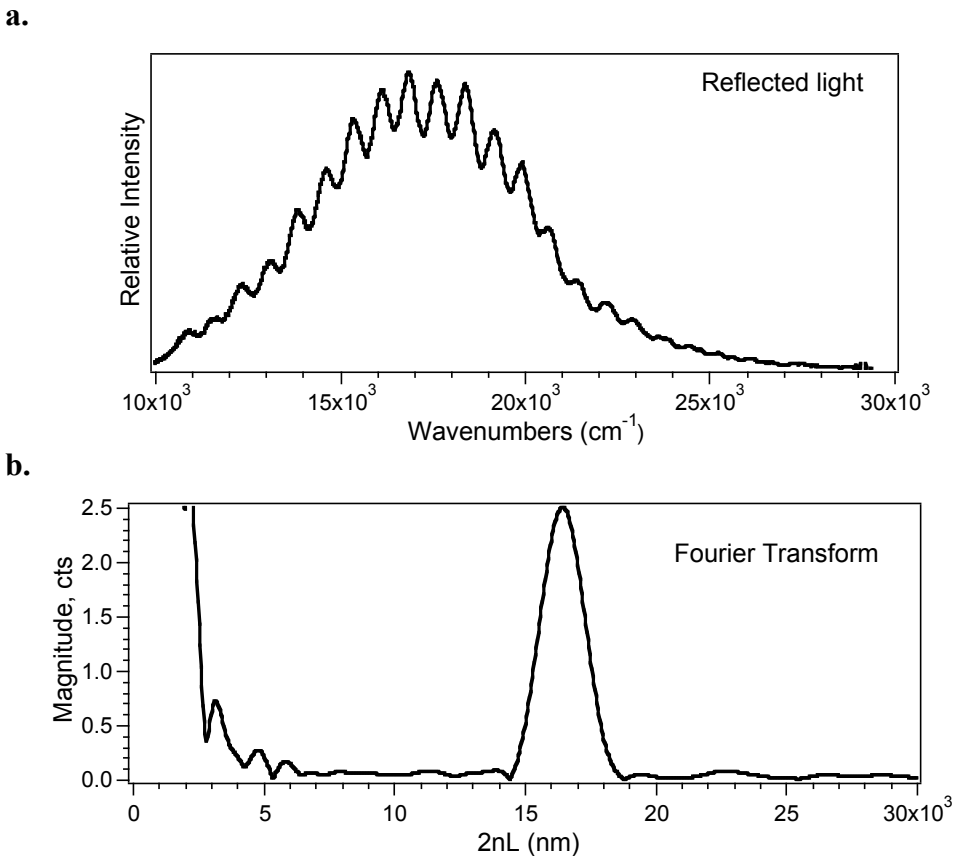

Figure 6.2 Optical charateristics of pSiO2 sensors. **a.** Reflected light spectrum of $pSiO_2$ sample immersed in phosphate buffered saline solution at pH 7.4, showing the characteristic Fabry-Pérot interference fringes. The sample is illuminated with focused white light, and reflected light is collected through the same lens positioned along an axis normal to the sensor surface and then transmitted to a CCD spectrometer. **b.** Fourier-transform of the spectrum in **(a)** yields a single peak whose position along the x-axis is equal to the value $2nL$ (product of average refractive index and thickness of the film).

6.4.3 pH Dependent Protein Infiltration

Figure 6.3 presents the temporal optical response of a $pSiO_2$ film upon introduction of BSA. Experiments were performed at pH = 4.2, 4.7, 6.7, and 7.0. The diffusion profiles are highly pH dependent, with very little BSA entering the pores at pH values greater than the p*I* of BSA (4.7), and the most BSA entering the pores at pH = p*I*. The data are consistent with an electrostatic binding process: the negatively charged $pSiO_2$ surface binds larger quantities of BSA when the protein is positively charged compared to when it is negatively charged.

Analagous pH behavior is observed with the other two proteins studied, and the results are summarized in Figure 6.4. The percent change in *nL* is found to reach a maximum at the p*I* value of the protein. For example, the peak in the value for BSA occurs at pH = 4.7, consistent with the published p*I* value for this protein.[183] BHb displays a maximum percent change in *nL* at pH ~ 6.7, although the transition is not as sharp as with BSA. EMb displays an even broader transition, with a maximum occurring in the pH range 5.7-7.3. The value of p*I* for all three proteins was independently measured using a commercial isoelectric focusing (IEF) kit (Figure 6.5). The broad transitions observed in the $pSiO_2$ film experiments for BHb and for EMb are consistent with the IEF results reported here and in the literature.[187, 192] The IEF results for BHb display a broad streak spanning a range of values from pH 6.8-7.4 that is consistent with the optical data. The data for BHb suggest that conformational changes, denaturing, or agglomeration of protein occurs under the conditions of the experiment. EMb has been found to contain two different components with different structures,[187]

and the IEF measurement yields two distinct values for p*I*, at pH 6.7 and at pH 7.3. The $pSiO_2$ optical measurement of this protein displays a broad maximum that spans these two p*I* values.

Figure 6.4b compares the temporal and near-equilibrium response of a $pSiO_2$ sensor for the three proteins studied. The pH of each solution in this set of experiments was chosen to match the p*I* of the particular protein tested. The two proteins with similar molecular masses (BSA, 66kDa and BHb, 65kDa) exhibit similar temporal responses when pH = p*I*, and the percent change in *nL* at equilibrium is comparable for both (Figure 6.4ab). As demonstrated previously, the magnitude of *nL* is proportional to the total mass of material infiltrated into the $pSiO_2$ layer.[193] Therefore, proteins with similar sizes and binding affinities should exhibit a similar percent change in *nL*. It is possible that certain residues on either BSA or BHb could interact more strongly with the $pSiO_2$ surface, leading to different binding affinities and thus different equilibrium values for the percent change in *nL*. However, the data indicate that this is not the case, and the magnitude of the signals observed in the optical experiment show that the maximum protein binding occurs at pH = p*I*. The equilibrium percent change in *nL* for EMb is approximately half the value observed for the other two proteins, indicating that only half of the total mass is bound to the $pSiO_2$ surface relative to BSA and BHb. The EMb protein is approximately one-third of the mass of the other two proteins, and its hydrodynamic radius is ~1/2 as large as either BSA or BHb (Table 6.1). Thus it is expected that EMb will form an overall thinner layer of protein, with correspondingly less total mass bound to the saturated $pSiO_2$ surface.

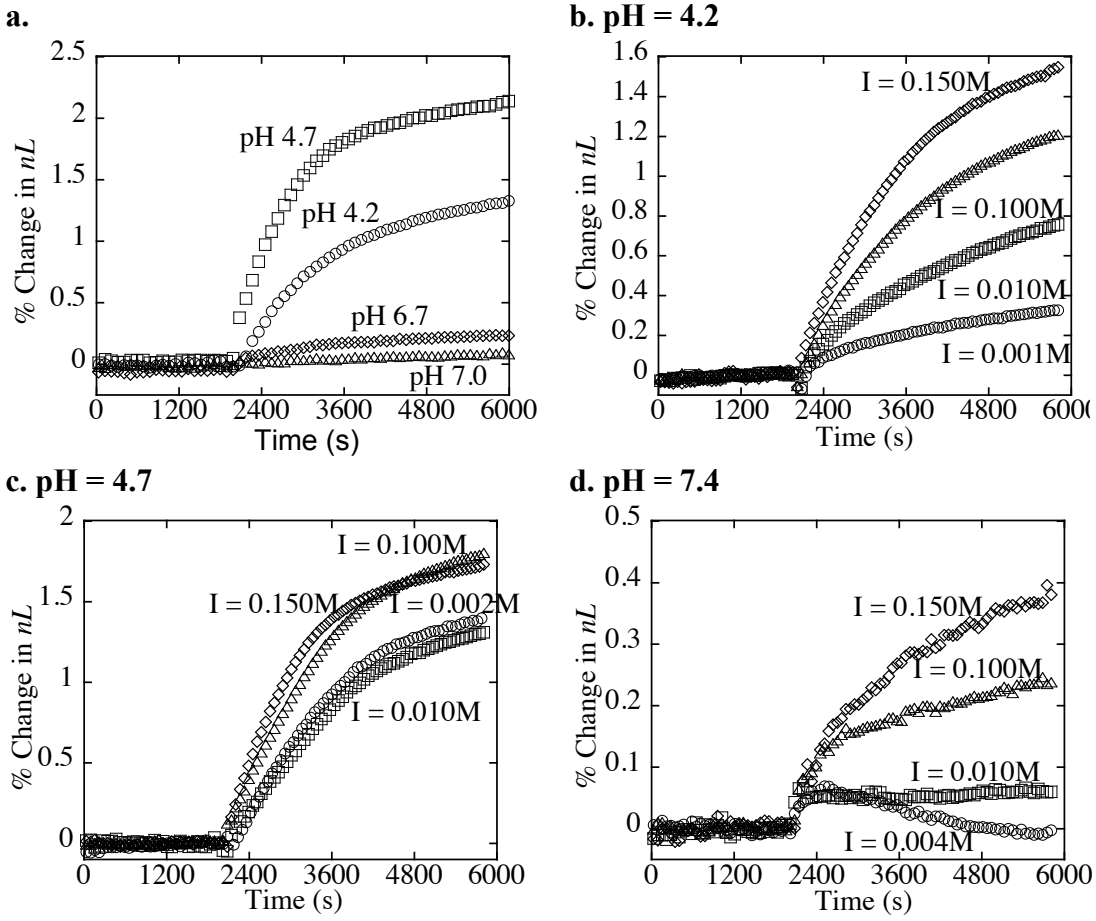

Figure 6.3 Optical responses of a $pSiO_2$ sensor to bovine serum albumin (BSA) as a function of time. For all charts, 1.0 mg/mL solution of BSA is introduced at t = 2000 s. **a**. Dependence on solution pH. The percent change in the quantity *nL* from the $pSiO_2$ film is greatest when pH = pI (= 4.7). Ionic strength for all solutions = 0.01 M to reduce screening effects from the electrolyte, ensuring an adequate electrostatic interaction between the pore walls and the protein.[174] **b-d.** Dependence on ionic strength for the indicated pH values.

a.

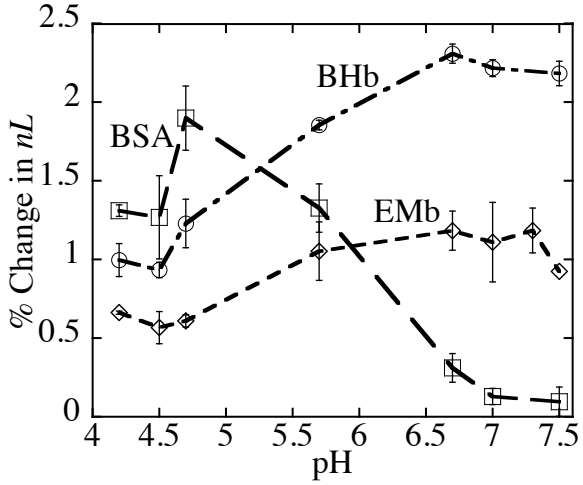

b.

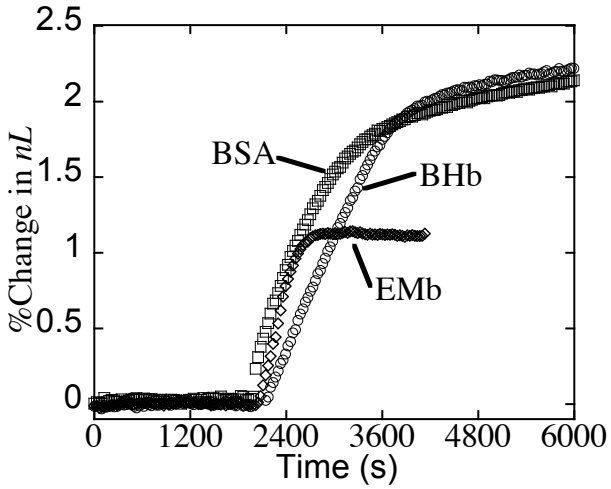

Figure 6.4 pH dependent protein transport as a function of time. **a**. Equilibrium percent change in *nL* as a function of solution pH for the three proteins. The results correlate with protein isoelectric point. Dashed lines are included as a guide to the eye. **b**. Optical responses of a $pSiO_2$ sensor to the indicated proteins as a function of time. For each protein the experiment was performed at a solution pH equal to the pI of that protein: pH 4.7 bovine serum albumin (BSA), pH 6.8 bovine hemoglobin (BHb), or pH 6.7 and 7.3 equine myoglobin (EMb). Proteins introduced at t = 2000 s. All measurements performed with 1.0 mg/mL protein concentration in 0.01 M buffers.

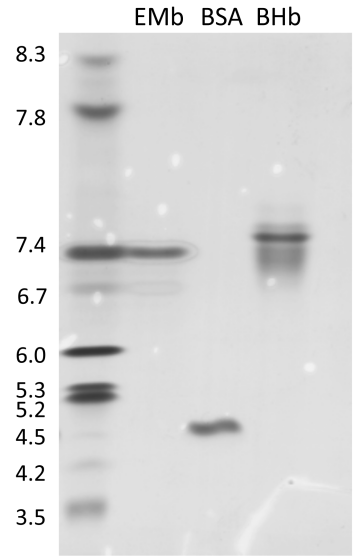

Figure 6.5 IEF gel electrophoresis of the model proteins. pH values are indicated on the left. The isoelectric points of bovine serum albumin (BSA), bovine hemoglobin (BHb) and equine myoglobin (EMb) are as indicated.

6.4.4 Protein Diffusion in Porous Silica Material

The data of Figure 6.4b also reveals information on the rate of transport of each protein in the porous layer. The EMb protein reaches the equilibrium binding point within 10 min, much more rapidly than the two larger proteins BSA and BHb. This result can be interpreted in terms of the physical size of the protein and its molar concentration. The Stoke-Einstein equation describes spherical particles diffusing in an aqueous solution. The diffusivity of a dilute suspension of spherical colloid particles, D, is expressed as[194]

$$D = \frac{\kappa T}{6\pi\mu_B r} \tag{6.1}$$

where κ is Boltzmann's constant, T is temperature, μ_B is the viscosity of the solution, and r is the hydrodynamic radius of the particle. Thus, proteins with smaller hydrodynamic radii are expected to show larger diffusivity in free solution. In the present experiments all protein solutions were studied at concentrations of 1 mg/mL; thus the molar concentration of EMb is nearly four times larger than the other two proteins. According to Fick's Second law of diffusion,[195] this larger concentration gradient will yield a larger observed rate of diffusion.

The pH of the buffer solution exerts a pronounced influence on the amount of protein that can infiltrate the $pSiO_2$ matrix (Figure 6.3 and Figure 6.4), and it also affects the rate of protein infiltration. Figure 6.6 compares the temporal response of BSA infiltration at pI = pH (4.7) and pI > pH (4.2) to theoretical curves derived from

Fick's Second law. Fick's Second law describes the time-dependent mass transfer of molecules in a concentration gradient:

$$\frac{\partial c}{\partial t} = D\left(\frac{\partial^2 c}{\partial x^2} + \frac{\partial^2 c}{\partial y^2} + \frac{\partial^2 c}{\partial z^2}\right) \tag{6.2}$$

where D is diffusion coefficient and c is concentration. Considering diffusion into the aligned pores of the $pSiO_2$ film as a one-dimensional process, the diffusion coefficient can be derived based on the following boundary conditions: (1) at $t = 0$, $c = 0$ anywhere in the $pSiO_2$ film, and (2) at $x = 0$, $c = C_0$, where t is time, x is the distance from the pore mouth in the direction perpendicular to the chip surface, c = concentration and C_0 = initial concentraion. As previously solved by Crank,[195] the one-dimensional solution to eqn. (6.2) is given by:

$$c(x,t) = C_0\left(1 - \frac{4}{\pi}\sum_{n=0}^{\infty}\frac{(-1)^n}{2n+1}\exp\left[-D(2n+1)^2\pi^2 t/4l^2\right]\cos\frac{(2n+1)\pi x}{2l}\right) \tag{6.3}$$

where $c(x,t)$ is the molar concentration and l is the total thickness of the $pSiO_2$ layer (5.7 μm) and n is an integer corresponding to the number of elements in the discretized solution. In the present case, solutions to eqn. (6.3) converged for $n = 10^4$ finite elements. To map this equation to the optical measurement, the total concentration of analyte in the film at time t was determined by summation of the concentration c of analyte in each finite element.

The data for diffusion of BSA into the mesoporous matrix for the case pH = pI (Figure 6.6a) fits the one-dimensional diffusional model well ($R^2 = 0.994$), yielding an effective diffusion coeffient of 2.3 x 10^{-10} cm^2/s. This value is 3 orders of magnitude smaller than the diffusion coeffient for free BSA in solution, which is ~6 x 10^{-7} cm^2/s

(reference [196]) The result of the fit indicates that transport of BSA is significantly impeded in the 50-nm pores of the $pSiO_2$ layer and it is comparable or slightly greater than the literature reports for diffusion of proteins and small molecules in confined porous alumina,[197, 198] agarose gel,[199] and silicon oxides,[200, 201] contributed to the flow-through systems perfomed in the literature experiments, allowing a greater concentration gradient between two compartments and faster diffusion. Although with impeded diffusion rate, the diffusion within the pores appears to follow Fick's 2nd law when the protein exhibits an overall neutral surface charge. Furthermore, the charged surfaces on the protein seem to influence the diffusion behavior, showing a deviation in the fit for concentration based diffusion.

a.

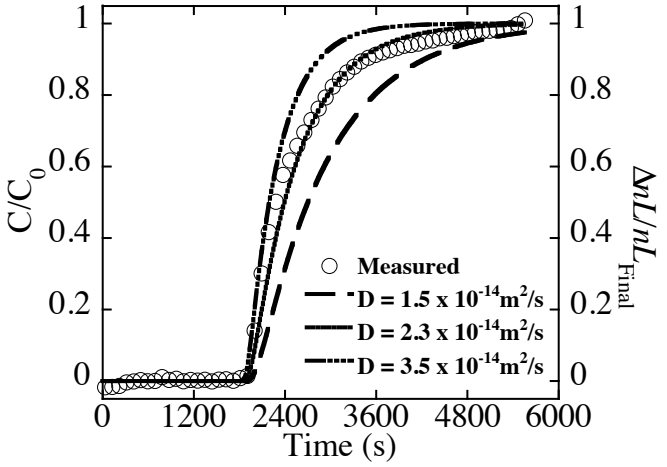

b.

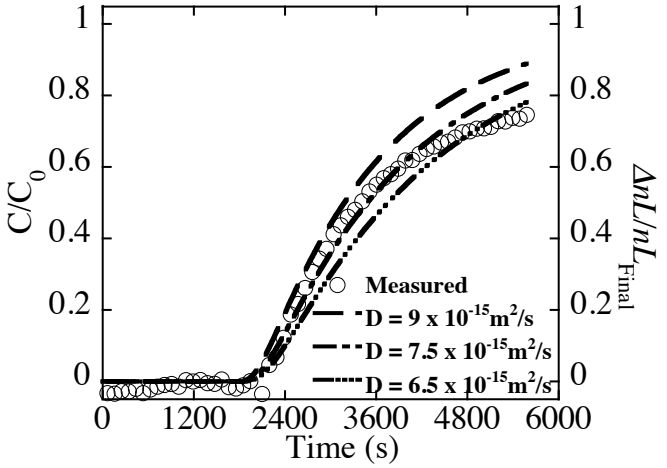

Figure 6.6 Temporal responses of optical $pSiO_2$ sensor to the protein BSA, measured **a.** at pH = 4.7 = p*I* and **b.** at pH = 4.2 < p*I*. Experimentally determined data points are given as circles, and the lines provide the theoretical prediction of Fick's law for the indicated values of diffusion coefficient. Concentration of protein in solution (C_0) = 1.0 mg/mL, introduced at $t \sim 2000$ s. The y-axis for the theoretical curves, C/C_0, represents the ratio of concentration of protein in the porous film to the concentration in the bulk solution. The experimental data are presented as change in the quantity *nL* relative to the final equilibrium value, DnL/nL_{Finall}, where $DnL = (nL_{measured} - nL_{initial})$ and $nL_{Final} = (nL_{equilibrium} - nL_{initial})$. Ionic strength for buffer solutions = 0.01 M.

6.4.5 Proposed Charge-Gated Binding and Transport Mechanism

Figure 6.7 describes a model to explain the observation that both the extent of protein infiltration and the rate at which it is admitted to the mesoporous $pSiO_2$ film maximizes at pH = p*I*. In the proposed model, the 50-nm pores are sufficiently narrow and the ionic strength are sufficiently low that electrostatic protein-protein repulsions in the nano-pores become significant. In order to provide an illustrative description, the three-dimensional electrostatic potential around the protein BSA was calculated for relevant solution pH and ionic strength values, using the computer program Adaptive Poisson-Boltzmann Solver (APBS).[202] The resulting charge distribution maps are presented in Figure 6.8.

For pH values < p*I* of the protein, the protein carries a net positive charge, and it is expected to be strongly attracted to the negatively charged pore walls (Figure 6.7, left image). This is consistent with prior studies of the loading of IgG antibodies,[14] protein A,[25, 176, 193, 203] and BSA[178, 179] into oxidized porous Si films, where protein loading is maximized for pH values at which the protein carries a net positive charge. For example, it has been reported that the anti-angiogenic antibody bevacizumab (trade name Avastin) can be concentrated by > 400-fold relative to its solution concentration in a porous SiO_2 film.[14] In that previous study, the ionic strength of the solution used to load the protein was much larger (15 x) than the ionic strength used in Figs 3-4, and so protein-protein repulsions were reduced. In the present case the protein feels a strong electrostatic attraction to the negatively charged pore surface, but protein-protein repulsions limit the rate and extent of infiltration.

At pH values > p*I* of the protein, the protein carries a net negative charge, and it is expected to be repelled from the negatively charged pore walls (Figure 6.7, right image). As in the case where the protein carries a net positive charge, protein-protein repulsions are an important limiter of the rate and extent of infiltration. In addition, the pore surface exerts a repulsive force on the negative portion of the protein, which is expected to reduce the total amount of protein adsorbed. The data of Figure 6.3 and Figure 6.4 support this interpretation; in particular, the smallest quantity of the protein BSA is adsorbed at pH > p*I*, where the protein carries a net negative charge, rather than at pH < p*I*, where the protein carries a net positive charge. In both cases the porous SiO_2 surface is negatively charged. In the absence of adsorption, the change in index expected when pure buffer (n = 1.333) is replaced with the solution of 1mg/mL protein (n = 1.334) corresponds to < 0.1 % change in signal. The infiltration data (Figure 6.4) indicate that negligible quantities of BSA adsorb at pH > 7, while significant adsorption of BHb and EMb occurs even at pH = 7.5. The porous SiO_2 matrix used in these studies is unstable (toward hydrolysis) at pH > 7.5, precluding the acquisition of data at pH values > 7.5.

In all cases studied, protein binding appears to be maximal at pH values where the net charge on the protein is zero (Figure 6.4). Although one might expect the strongest binding between the negatively charged porous SiO_2 surface to be in a pH range where the protein carries a net positive charge (i.e., pH < p*I* of the protein), the effect of protein-protein repulsions is significant, especially for solutions of low ionic strength (Fig. 2). Thus the optical binding curves show maximal response at pH = p*I*.

The diffusional behavior of the proteins in the pores (Figure 6.6) is also closest to the ideal predictions of Fick's law when the protein is neutral.

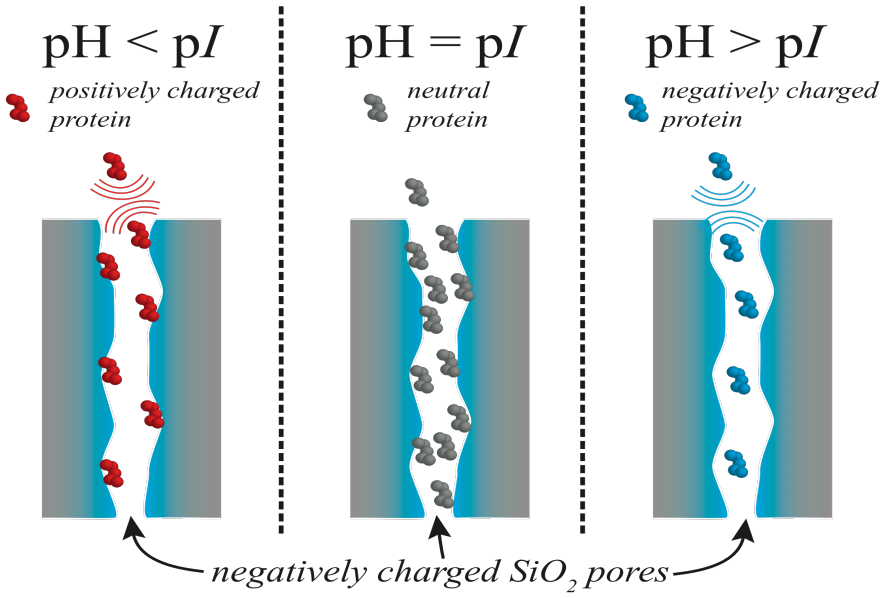

Figure 6.7 Proposed mechanism controlling rate and extent of protein infiltration to $pSiO_2$ pores. At pH < p*I* for the protein (left), the positively charged protein feels a strong electrostatic attraction to the negatively charged pore surface, but protein-protein repulsions limit the rate and extent of infiltration. When the pH of the solution is equal to p*I* (center), the protein has no net charge, protein-protein repulsions are minimized, and both the rate and extent of protein infiltration is maximized. Protein transport is concentration-driven. At pH > p*I* (right), the negatively charged protein is repelled by both the pore walls and other proteins, and diffusion and adsorption are limited. In both the left and the right cases, electrostatic repulsions are important contributors to the diffusional process.

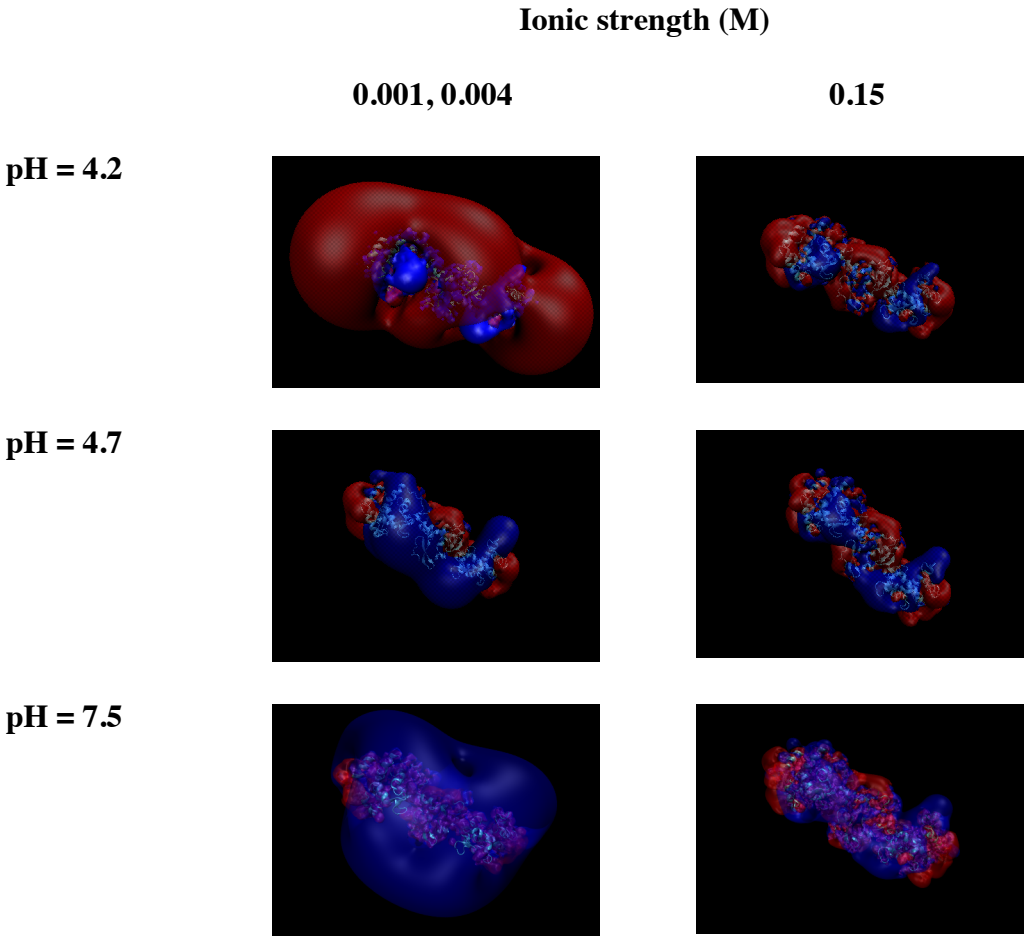

Figure 6.8 Charge distribution on BSA as a function of pH and ionic strength. Three-dimensional charge density maps resulting from APBS electrostatic calculations for bovine serum albumin (BSA), determined for the indicated ionic strength and pH values. Blue color indicates negative charge and red indicates positive charge. BSA structure from crystallographic data[204].

6.4.6 Effect of Ionic Strength and Protein Surface Charge

In order to test the proposed charge-gated binding and transport mechanism, we obtained optical binding curves and zeta potential data as a function of ionic strength for the test protein BSA (Figure 6.3b, Figure 6.9). Ionic strength has a direct effect on the solution's ability to screen the charges on dissolved proteins.[197, 205] The effect of ionic strength on the calculated charge distribution around the BSA molecule is shown in Figure 6.8. These calculations are consistent with the observed rate and extent of protein infiltration (Figure 6.3), which increase with increasing ionic strength (decreasing Debye length)[205] for either the positive (pH < p*I*) or the negative (pH > p*I*) protein, but remain relatively constant for the neutral protein (pH = p*I*). As expected, the zeta potential tends toward zero with increasing ionic strength (Figure 6.9). The data support the conclusion that charged proteins are less likely to enter (and they diffuse more slowly in) nanopores when the solution is at a lower ionic strength. Diffusion of neutral proteins (pH = p*I*) is driven mostly by the concentration gradient in the $pSiO_2$ layer, and ionic strength exerts little influence in this case (Figure 6.3b).

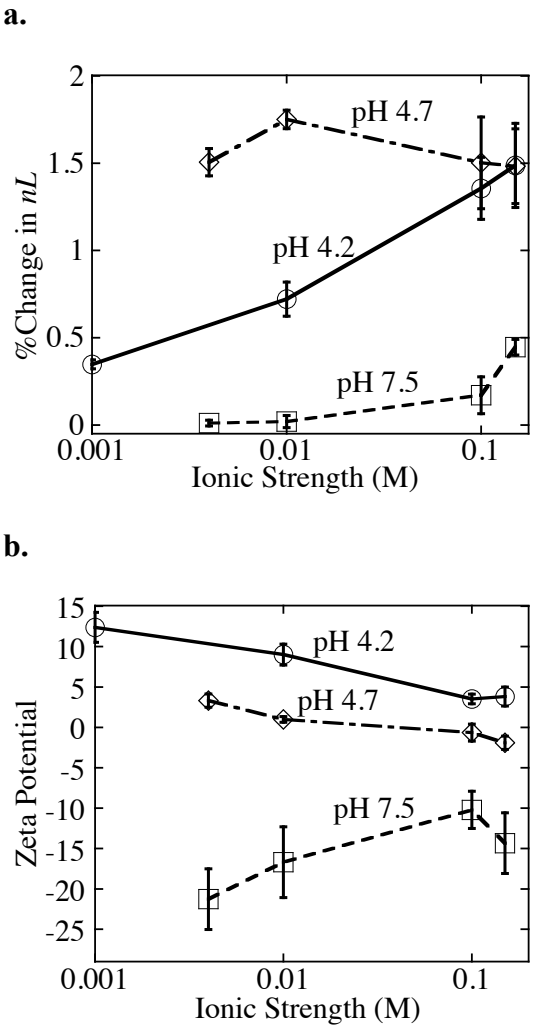

Figure 6.9 Influence of solution ionic strength on extent of infiltration and zeta potential of BSA. **a**. Optical responses (percent change in the quantity *nL*) of a $pSiO_2$ sensor to bovine serum albumin (BSA) as a function of ionic strength. A 1.0 mg/mL solution of BSA is measured. **b**. Zeta potential of BSA as a function of ionic strength, for the pH values indicated.

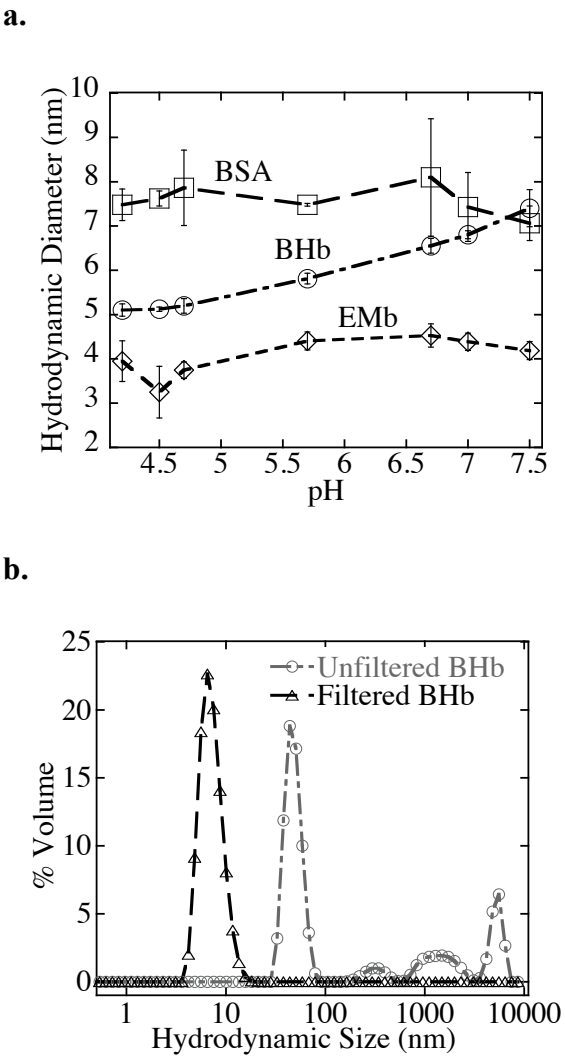

Figure 6.10 Hydrodynamic diameter of BSA, BHb, and EMb, measured by DLS. a, Hydrodynamic diameter of BSA, BHb, and EMb as a function of pH, obtained on filtered protein solutions. b, DLS traces showing particle size distribution for filtered and unfiltered BHb. Unfiltered BHb displays more than one group of hydrodynamic sizes, indicating significant aggregation of the protein under the conditions of the study. A single hydrodynamic size distribution is observed after filtration, yielding a hydrodynamic diameter in agreement with the literature value. DLS data for EMb (not shown) also indicated more than one set of hydrodynamic sizes. Similar to BHb, a single hydrodynamic size distribution is observed after filtration, yielding a hydrodynamic diameter in agreement with the literature value. BSA exhibits a stable hydrodynamic diameter across the range of pH values studied, with a single peak in the DLS hydrodynamic size histogram (not shown).

6.5 Conclusions

The pores in the $pSiO_2$ sensor are sufficiently small that they are capable of discriminating between isolated proteins and protein aggregates. IEF (Figure 6.5) and DLS (Figure 6.10) data indicate that the proteins BHb and EMb form aggregates under the conditions of the experiment. A single modal size distribution was obtained upon filtering the protein solutions through a 100-nm cutoff membrane. Filtered and unfiltered protein solutions yielded similar optical responses from the $pSiO_2$ films, indicating that the nanostructure is rejecting these larger aggregates while still admitting the individual proteins of interest. The ability of $pSiO_2$ to act as a size-selective sensor has been reported previously.[28, 171] In the present case, the $pSiO_2$ film yields more distinguishable p*I* value than the IEF experiment. In addition, the sampling and detection volumes in the present system occupy the same, very small (5 nL) physical space; thus the approach requires significantly smaller sample volumes and analyte quantities. The optical method reported here is complementary to traditional isoelectric focusing as a means of quantifying p*I*, and it provides real-time, nanostructure-dependent diffusional data that are not accessible by other means.

Chapter six, in part or in full, is a reprint (with co-author permission) of the material as it appears in the following publication: Chen, M. Y.; Sailor, M.J., Charge-Gated Transport of Proteins in Nanostructured Optical Films of Mesoporous Silica. *Analytical Chemistry, manuscript in preparation.* The author of this dissertation is the primary author of this manuscript.

CHAPTER SEVEN

ELECTRIC FIELD ASSISTED PROTEIN TRANSPORT, CAPTURE, AND INTERFEROMETRIC SENSING IN CARBONIZED POROUS SILICON FLIMS

7 Electric Field Assisted Protein Transport, Capture and Interferometric Sensing in Carbonized Porous Silicon Films

7.1 Abstract

The fidelity of detection in a biosensor is limited by the ability of the device to identify small quantities of analyte in the presence of much larger quantities of interfering molecules. Analyte separation or preconcentration are key aspects of the analysis, and the drive to decrease sample volumes and increase throughput, which has led to chip-based microanalysis systems that combine both separation and sensing components within a volume of a few cubic micrometers. Electric fields, applied via external electrodes or photogenerated in a semiconducting matrix[206], are often used to induce biomolecular separations in these systems. For example, electroadsorption phenomena provide a means to concentrate charged analytes on electrode surfaces, and electrophoresis induces field-driven migration of charged species. Here we describe an electrically addressable optical biosensor that allows simultaneous separation, capture, and detection of proteins within the same ultrasmall physical volume (5 nL). The approach uses a high surface area, highly porous optical electrode based on a carbonized porous Si Fabry-Perot film. An applied negative electric potential induces concentration of the positively charged test protein, lysozyme within the porous nanostructure to a level ~ 9600 times the free solution concentration. Diffusion and adsorption of protein within the 40nm diameter pores is monitored in real time by optical interferometry, providing a means to identify the protein based on its

characteristic charge/size/diffusion characteristics. The captured protein can be held for several hours, and it is released when the sensory electrode is returned to zero bias. The released protein retains its enzymatic activity, and the optical electrode can undergo multiple adsorption/desorption cycles.

7.2 Introduction

Since the first experiments demonstrating single-molecule transport in a nanopore constructed from the natural membrane protein, α-haemolysin,[48] many artificial polymeric[3], inorganic[3, 27, 49], and composite[207] nanoscale porous structures have been developed. The constricted environment in a nanopore has a substantial influence on molecular transport that can be harnessed for biosensing[51, 208], filtration[27, 209], nanofluidic[4], and other applications. A common means to induce diffusion or migration of biomolecules is to apply an electric field, and this has been used to enhance the rate and selectivity of ionic transport through nanotube membranes[173]. Because of the high voltages needed to produce electrophoretic transport (typically greater than 1KV applied voltage is needed to achieve field strength in the range of 100 V/cm to 500 V/cm), the electrodes in these experiments are usually far removed from the separation matrix to avoid excessive heating or degradation.

Charged molecules can also be moved with much smaller voltages. Electroadsorption involves the adsorption of ionized species onto an electrode surface upon application of small potentials (typically < 1V) [210, 211]. The distance traveled by the ions is relatively small (few nm), and the quantity of material that can be moved is also small, usually corresponding to less than a monolayer on the electrode surface [210].

Nevertheless, in solutions containing low analyte concentrations, electroadsorption can yield dramatic increases in sensitivity, especially when coupled to an immunological [212], electrochemical, or elipsometric [213] assay. Photoinduced electroadsorption, involving illuminated semiconducting electrodes, has been used to separate proteins with high selectivity [214]. In the present work, a modified porous Si (pSi) layer is used as the electroadsorptive substrate. The high surface area of this three-dimensional material provides a means to capture and concentrate significant quantities of protein. Furthermore, if the pSi matrix is prepared as a conductive but semitransparent thin film, the optical response provides a means to detect and identify the biomolecule.

7.3 Experimental Methods

7.3.1 Materials

Aqueous HF (48%) and ethanol (99.9%) were supplied by EMD and Gold Shield Chemical Company, respectively. Porous Si samples were prepared from highly doped p-type Si with resistivity ranging from 0.0008-0.001 Ω-cm (polished on the (100) face, boron doped, from Siltronix Corp). Chicken lysozyme (Lys, 14 kDa) was obtained from Sigma-Aldrich, Cat. No. L6876. The protein was used as-received without further purification. 5mM buffer solutions were prepared by mixing ultrapure (18 MW) water with monobasic sodium phosphate (Fisher Scientific, Cat. No. S369-500). The pH was adjusted by addition of small quantities of aqueous HCl or NaOH. The ionic strength of the prepared buffer solutions ranged from 0.001 to 0.15 M. Lysozyme activity assay and bicinchoninic acid assay kits were received from

Invitrogen, Cat. No. E33013 and Thermo Scientific, Cat. No. 23235, respectively. Protein assay kits were used as-received.

7.3.2 Poros Silicon Preparation and Charaterization

Porous Si samples were anodically etched in a 3:1 solution of aqueous 48% HF:ethanol. Si chips with an exposed area of 1.2 cm^2 were contacted on the back side with a strip of aluminum foil and mounted in a Teflon etch cell. Samples were then electrochemically etched in a two-electrode configuration using a platinum mesh counter electrode. Single-layer samples were prepared by application of a current density of 467 mA/cm^2 for 48 s. Samples were rinsed three times with ethanol and then dried with nitrogen gas. Porosity was characterized using the nondestructive spectroscopic liquid infiltration method (SLIM) as described previously[155].

7.3.3 Thermal Carbonization

Porous Si samples were thermally carbonized in a tube furnace (Lindberg/Blue M) at 450 °C for 30 min with a constant flow of acetylene and nitrogen gas at a flow rate of 1 L/min and allowed to cool to room temperature in a nitrogen atmosphere.

7.3.4 Interferometric Reflectance Spectra Collection and Data Processing

Reflectance spectra were recorded with an Ocean Optics USB-4000 CCD spectrometer coupled to a bifurcated fiber optic cable. A tungsten halogen light source was used to illuminate the surface of the sample via one arm of the bifurcated fiber.

Both the spectral acquisition and light illumination were performed along an axis normal to the surface of the pSi sample. The optical thickness quantity *nL* (where *n* = average refractive index and *L* = sample thickness in nm), was obtained from the Fast Fourier Transform (FFT) of the acquired reflectance spectrum as previously described[215].

7.3.5 Time-Resolved Biosensing Experiments

Buffer solutions with ionic strength ranging from 0.007 to 0.15 M, and pH values of 6.7, were used in the experiments to study the effect of ionic strength on protein loading. In the experiments to quantify loading and concentration efficiency as a function of applied bias and bulk solution protein concentration, buffer solutions (pH 6.7) with ionic strength of 0.007 M was used. Optical data were acquired using a custom-designed flow cell system fitted with a platinum electrode and an optically transparent window to facilitate acquisition of reflectance spectra. The counter electrode was a loop of platinum wire, and the carbonized pSi working electrode was contacted on the backside with a strip of aluminum foil. In a typical experiment, spectra were acquired every 10s and an initial baseline was established in pure buffer solution (flow rate ~1mL/min). A solution containing 5mL of the protein of interest, dissolved in the identical buffer, was then introduced to the flow cell (flow rate ~1mL/min) and spectral data were acquired until equilibrium was established. The buffer solution was circulated in a closed loop during data acquisition (total solution volume = 5 mL).

7.3.6 Lysozyme Activity Study

Three lysozyme solution samples were assayed: (1) buffered solution (pH = 6.7) containing as-received lysozyme, (2) similarly buffered solution containing lysozyme that had been circulated in the flow cell containing a carbonized pSi film held at an applied bias of 0V relative to the Pt counter electrode, and (3) buffered solution containing lysozyme that had been circulated in the flow cell containing a carbonized pSi film held at an applied bias of -2.75 V relative to the Pt counter electrode. After 120 min, the applied bias was changed to 0 V and the solution allowed to circulate for an additional 60 min to ensure equilibration of the released lysozyme. The solutions were collected from the flow cell and incubated at 37 °C with the lysozyme assay reagents. Fluorescence was measured on a microplate reader using excitation/emission wavelengths of 485/530 nm at five different time points (30, 60, 90, 120, and 150 min).

7.4 Results and Discussion

7.4.1 Optical and Physical Characteristics of Carbonized Porous Silicon Sensors

Prepared by the controlled electrochemical etch of single crystal Si, porous Si films can be designed with pore sizes ranging from 1 to several hundred nm, allowing size-selective filtration[27] or separation[171] of a wide range of molecular species. In the present work, a 9.8μm thick pSi film with nominal pore diameters of 40nm was prepared (Figure 7.1). The pores are parallel to each other and propagate in the <100>

direction, orthogonal to the face of the Si substrate. The chemical stability of as-formed pSi films is poor, and most biosensor applications of pSi films require thermal oxidation of the matrix prior to use [216]. Silicon oxide is an electrical insulator that was not suitable for the electroadsorption experiments. Instead, a conductive carbon coating was applied to the pSi surface using the thermal carbonization route developed by Salonen [217]. Synthesized by high-temperature decomposition of acetylene gas on as-formed pSi, this surface has been shown to be stable in aqueous media and amenable to optical biosensor applications [218]. In the present case, the carbonization reaction generated a partially transparent, slightly hydrophobic surface (contact angle ca 90°) that was readily infiltrated by aqueous solutions.

The pore dimensions in the pSi samples were smaller than optical wavelengths, and so the thin films displayed Fabry-Pérot optical interference fringes in the white light reflectance spectrum (Figure 7.1c). This interference spectrum provided a means to perform label-free detection of biomolecules that entered the film, based on characteristic changes in the refractive index of the porous medium [25, 170]. The observed interference spectrum is determined by the average refractive index, n, and the physical thickness, L, of the pSi sample via the Fabry-Pérot relationship [193]. The value nL was determined from the Fourier transform of the spectrum (Figure 7.1d) [109]. For the biosensing experiments, changes in nL corresponding to entry or exit of protein from the pSi layer were recorded in real time using a fast CCD-based spectrometer.

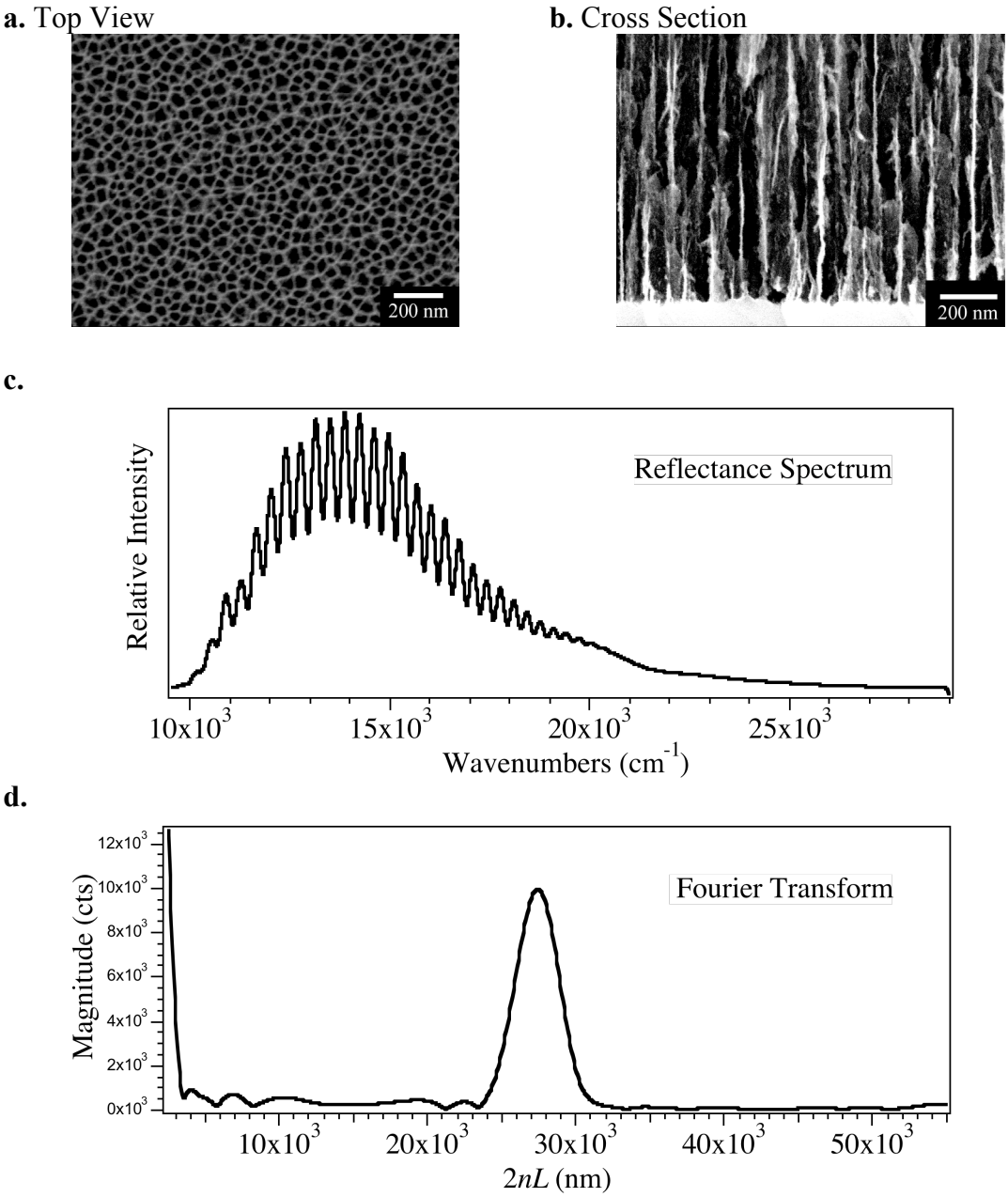

Figure 7.1 Physical and optical characteristic of carbonized porous silicon (pSi-C) films. **a-b,** Representative top (plan) view (a) and cross sectional view (b), images of a porous Si sample obtained prior to carbonization. Sample thickness is 9.8 mm, with a porosity of 73 % and average pore diameter 40 nm. **c**, Reflected light spectrum of pSi-C sample immersed in pH 6.7 buffer, showing the characteristic Fabry-Pérot interference fringes. The sample is illuminated with focused white light, and reflected light is collected through the same lens positioned along an axis normal to the sensor surface and then transmitted to a CCD spectrometer. **d**, Fourier-transform of the spectrum in (c) yields a single peak whose position along the x-axis is equal to the value $2nL$ (product of average refractive index and thickness of the film.

7.4.2 Field Assisted Protein Adsorption and Capture

Lysozyme (14 kDa, isoelectric point ~ pH 11[219]) was selected as a test protein for this study. At pH=6.7, lysozyme exhibits a net positive charge. When the carbonized pSi film was held at a negative potential relative to a Pt counter electrode in the presence of aqueous lysozyme at pH=6.7, the optical response of the pSi film indicated significant accumulation of protein within the pSi matrix. The potential-dependent response is reported in Figure 7.2 in terms of the percent change in *nL*,

$$\%\Delta nL = \frac{nL_{t,\Delta V} - nL_{t=0,\Delta V=0}}{nL_{t=0,\Delta V=0}} \times 100 \qquad (7.1)$$

where $nL_{t,\Delta V}$ is measured at a given time t and applied bias ΔV; $nL_{t=0,\Delta V=0}$ is the value of *nL* measured from the sample in pure buffer solution at a time immediately prior to introduction of protein (t = 0) and at an applied bias (ΔV) of 0 V relative to the Pt counter electrode. At a bias of 0 V in pure pH 6.7 buffer, a small, steady decrease in the baseline value of % Δ*nL* was observed, indicative of slow oxidation and dissolution of the carbonized pSi matrix. Lysozyme (10 mg/mL) was introduced to the flowing buffer solution after 30 min, which resulted in an instantaneous increase in the value of % Δ*nL* as protein infiltrated the pSi matrix. After a steady-state value was reached, the negative bias on the pSi sample was increased in a series of discrete steps, from -0.5 to -2.75 V. Bias was maintained at a given value for 10 min, after which the bias was returned to 0 for 20 min. An increase in the value of % Δ*nL* was observed that was roughly proportional to the applied negative bias with a slope ~ - 0.19 (Figure 7.3) and the value returned to the baseline when the bias was set back to 0 V. Control experiments using buffer solution that contained no protein (Figure 7.2, lower trace) or

an anionic protein (bovine serum albumin, BSA) displayed minimal response. The results are consistent with a voltage dependent protein adsorption/desorption process: adsorption of protein to the pore walls of the electroactive pSi matrix depletes the solution within the pores of protein, setting up a concentration gradient. Infiltration of additional protein from the bulk solution then generates the observed increases in the value of % ΔnL.

The total quantity of protein adsorbed on the pSi electrode increased with more negative values of ΔV. A concentration factor (CF), defined as the ratio of the mass of protein in the pSi film per unit volume to the mass of free protein remaining in the bulk solution per unit volume eqn.. (7.2) was determined from the measured equilibrium *nL* values for various values of the bulk solution concentration of lysozyme.

$$CF = \frac{[lysozyme]_{pores}}{[lysozyme]_{solution}} \tag{7.2}$$

a.

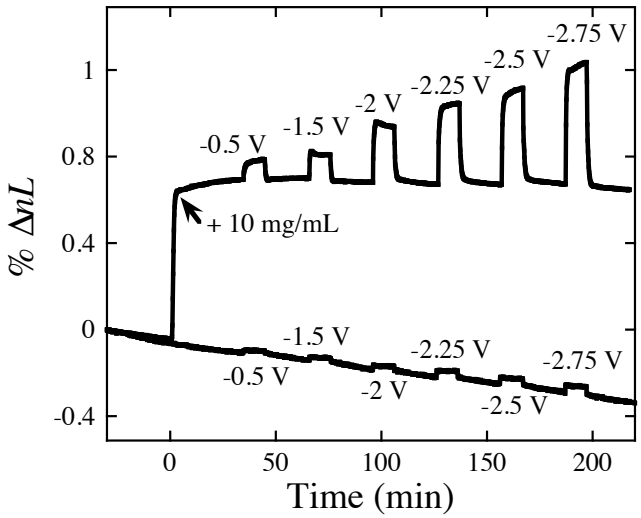

b.

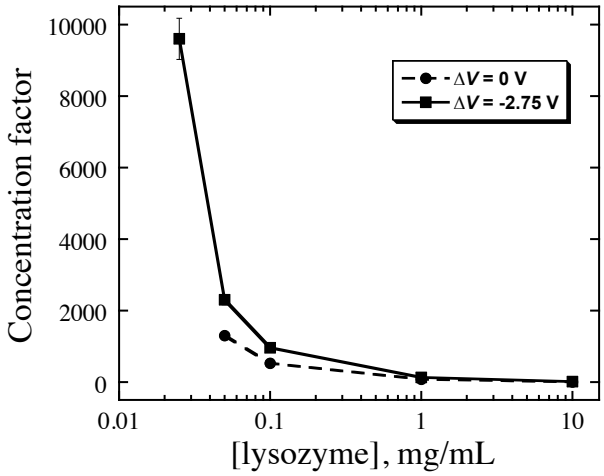

Figure 7.2 Voltage dependent adsorption and infiltration of lysozyme, measured by optical interferometry on a cabonized pSi film. **a,** Percentage change in optical thickness as a function of time. The pSi film was immersed in pH 6.7 buffer. The top trace represents the optical response of the sensor after introduction of 10 mg/mL lysozyme at time t = 0, the bias values (ΔV) applied, relative to a Pt counter electrode, are indicated. Bottom trace represents the control experiment in pure buffer, without added lysozyme. **b,** Concentration factors representing the amount of lysozyme loaded into the pSi film relative to the bulk solution concentration, calculated from eq. 3, as a function of bulk solution concentration of lysozyme. Data for two values of ΔV are shown. Lysozyme loading values calculated from the optical data, assuming protein density of 1.36 g/mL (reference [220]) and refractive index of 1.55(reference [221]).

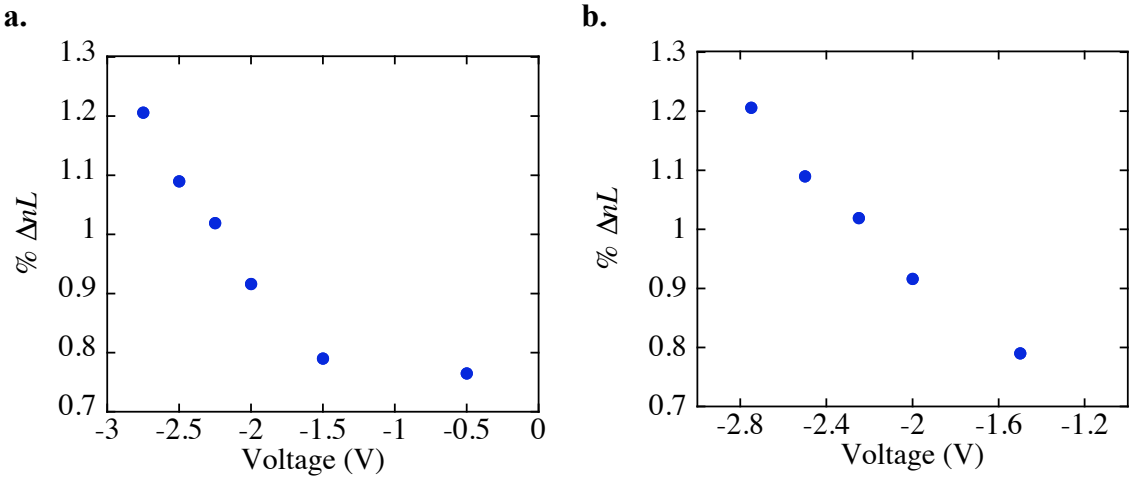

Figure 7.3 Percent Δ*nL* as a function of voltage. Sensor response to discrete voltage steps, from -0.5 to -2.75 V, preloaded with 10mg/mL lysozyme. a. An increase in % Δ*nL* that is roughly proportional to the applied negative bias with a slope ~ - 0.19. b. Without -0.5 V, shows a more linear relationship between negative bias and sensor response with slope ~ -0.33 and R^2 ~0.99.

7.4.3 Concentration Dependent Transport

The protein displays time dependent transport within the carbonized pSi matrix that is sensitive to concentration and applied voltage. At zero applied bias, the sensor required ~10 min to reach a steady-state value when the concentration of lysozyme introduced was 10 mg/mL, and ~2.5 h when the concentration of lysozyme was 0.1 mg/mL (Figure 7.4a). The interfacial capacitance of the device was measured to be 8 $\mu F/cm^2$; the time constant or a 0.5 V (non-Faradaic) voltage step was ~ 0.4 sec (Figure 7.5). In order to compare characteristic timescales, the percent change in *nL* relative to the steady state values was defined as

$$\%\Delta nL_{rel} = \frac{nL_{t,\Delta V} - nL_{t=0,\Delta V=0}}{nL_{t=\infty,\Delta V} - nL_{t=0,\Delta V=0}} \times 100, \qquad (7.3)$$

where $nL_{t,\Delta V}$ and $nL_{t=0,\Delta V=0}$ are as defined above and $nL_{t=\infty,\Delta V}$ is the equilibrium value of *nL* measured in the presence of lysozyme and with applied bias ΔV. Application of a bias of ΔV = -2.75 V to a chip that had equilibrated with 0.1 mg/mL of lysozyme at ΔV = 0 resulted in a doubling of the quantity of protein in the porous matrix (Figure 7.4a). When ΔV was returned to a value of 0, lysozyme diffused out of the matrix and the sensor returned to the original equilibrated (ΔV = 0) value. The temporal response of the film under negative bias was highly dependent on protein concentration (Figure 7.4b). For a given value of ΔV, the approach to equilibrium after introduction of lysozyme was slower at lower concentrations of the protein. These observations are in accordance with Fick's second law, which describes the time-dependent mass transfer of molecules in a concentration gradient[195]. The approach to equilibrium was faster the more negative the applied bias (Figure 7.4c).

The concentration factor increases with negative applied bias and with lower concentrations of lysozyme in the bulk solution (Figure 7.2b). For bulk solution concentrations of 25 μg/mL (the lowest concentration studied), lysozyme was not detectable at zero applied bias. However, with an applied bias of ΔV = -2.75 V, significant accumulation of protein was observed; the optical data indicated that 91 mg/mL of lysozyme accumulated in the pSi film, which reduced the total bulk solution concentration of lysozyme to 9 μg/mL, or a concentration factor of 9600. These protein concentration values were verified using a standard protein assay (micro BCA); the pSi film was digested in aqueous NaOH (1M) overnight, the supernatant was neutralized with aqueous HCl (1M) and subjected to the assay. The assay yielded a protein concentration in the pSi film of 86 mg/mL, in good agreement with the optical measurements. Whereas the total quantity of protein admitted into the pSi film scaled with the bulk solution concentration, the concentration factor increased with decreasing protein concentration in the bulk solution, such that the greatest degree of partitioning into the pSi film occurred at the lowest values of bulk solution concentration (Figure 7.2b).

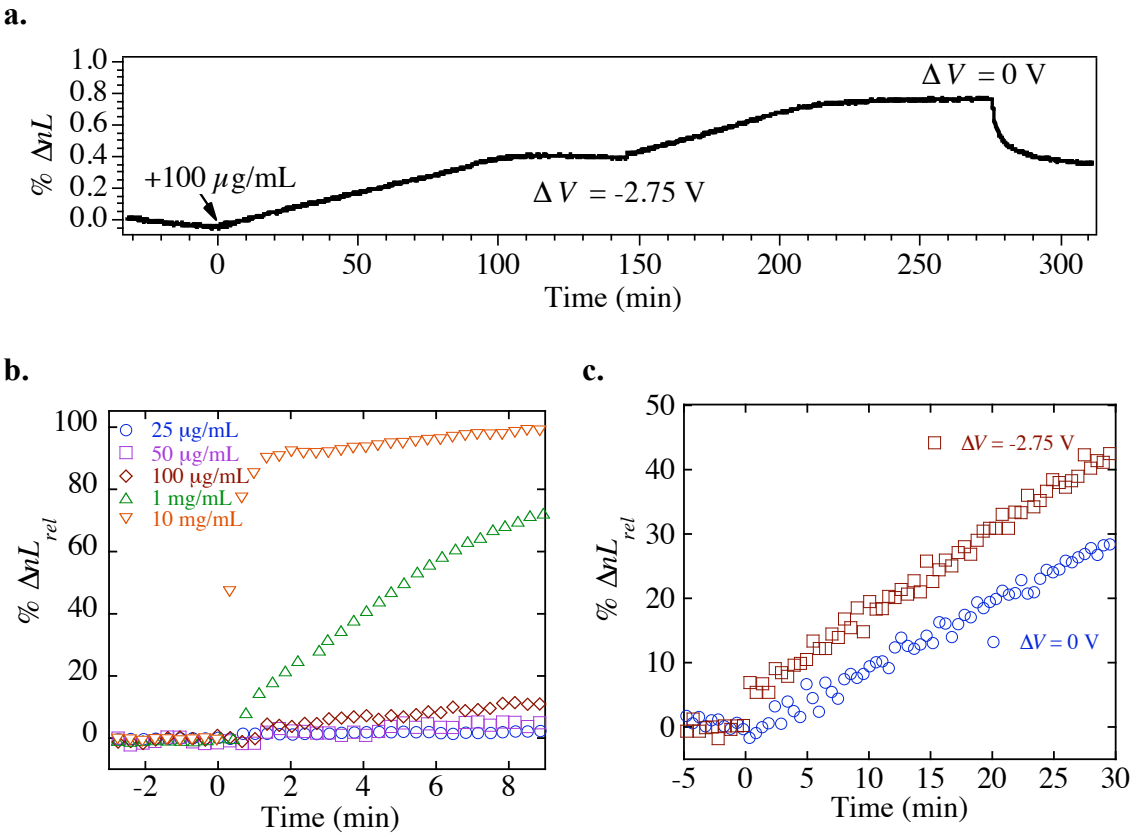

Figure 7.4 Temporal optical responses of carbonized pSi sensors upon application of bias in the presence of lysozyme. **a,** Optical response, % ΔnL_{rel}, as a function of time. Lysozyme (100 μg/mL) was introduced at time t = 0s. At t = 140 min, ΔV was switched from 0 to -2.75 V. At t = 280 min, ΔV was switched back to 0. **b,** Expanded view of % ΔnL_{rel} vs time, showing the temporal response of the film upon application of a step in applied bias in the presence of the indicated concentrations of lysozyme. For each trace, ΔV was switched from 0 to -2.75 V at time t = 0. **c,** Comparison of % ΔnL_{rel} vs time profiles for addition of 100 μg/mL lysozyme to the carbonized pSi chip, held at ΔV values of 0 and -2.75 V as indicated.

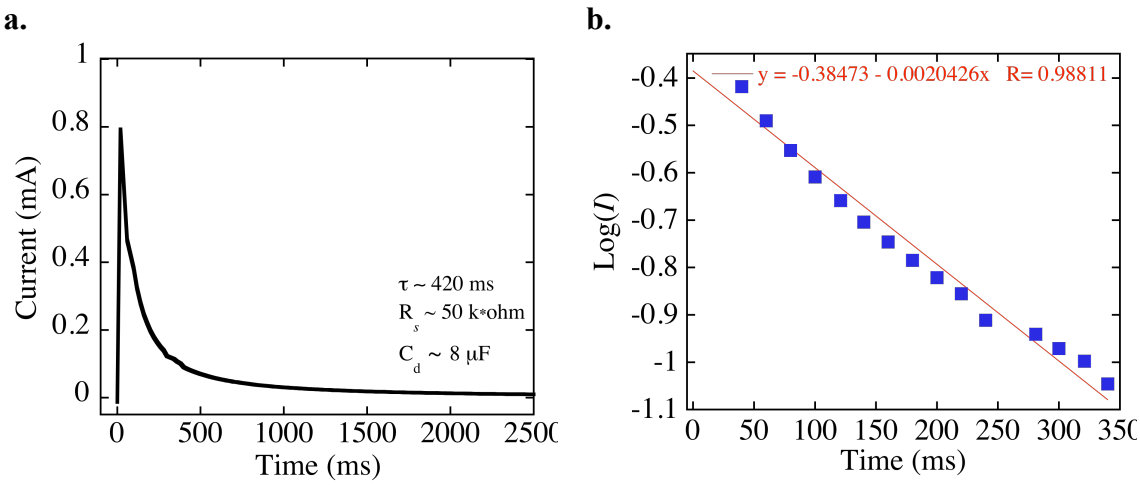

Figure 7.5 Current transient (*I vs t*) resulting from a -0.5 V non-Faradaic potential step. **a,** Current transient after application of a -0.5 V step to the pSi film. The electrolyte contained buffer at an ionic strength of 0.007 M. **b,** Natural logarithm of the current vs time trace, used to calculate interfacial (double layer) capacitance, C_d (based on $\tau = R_s * C_d$, reference [210]). Based on three replicate -0.5 V steps, the average time constant, τ was 420 ms, the resistance of the cell was 42 kΩ/cm^2, and interfacial capacitance was 8 µF/cm^2.

7.4.4 Eletroadsorption

A characteristic of electroadsorption is that the magnitude and sign of the charge on the ion exerts a strong influence on the extent of adsorption [211]; in the present case this is manifested in the magnitude of $\% \Delta nL$. Control experiments using bovine serum albumin (BSA) yielded no significant response in $\% \Delta nL$ when the value of ΔV was switched between 0 and -2.75 V. BSA carries a net negative charge at pH 6.7, and so the data are consistent with an electroadsorption phenomenon driving protein diffusion into the pores. BSA would be expected to adsorb to a pSi electrode held at a positive bias. However, the pSi samples exhibited significant corrosion at values of $\Delta V \geq 0$, and although evidence of electroadsorption of BSA is expected at positive bias values, the instability of the pSi electrode precluded quantification.

7.4.5 Ionic Strength Effect

The ionic strength of the electrolyte exerted only a minor effect on electroadsorption. The equilibrium quantity of lysozyme adsorbed at the pSi electrode increased slightly upon increasing the ionic strength (Table 7.1), and the rate at which it achieved equilibrium (at pH 6.7) was unaffected for electrolyte concentrations in the range 0.007-0.15 M (Figure 7.6). Thus the mechanism of transport of protein in the electrified pSi matrix can be attributed to diffusion along a concentration gradient that is driven by electroadsorption of protein within the electrical double layer, rather than electrical field-driven ion migration such as that observed in electrophoresis.

Table 7.1 Dependence of lysozyme concentration factor on ionic strength.*

	I = 50 mM	I = 100 mM	I = 150 mM
CF, $\Delta V = 0$ V	69	82	100
CF, $\Delta V = -2.75$ V	110	130	140

* Concentration factor CF, as defined in eq. 3 in the text. Ionic strength (I) corresponds to total electrolyte concentration in the solution. Free lysozyme concentration (in solution) was 1 mg/mL .

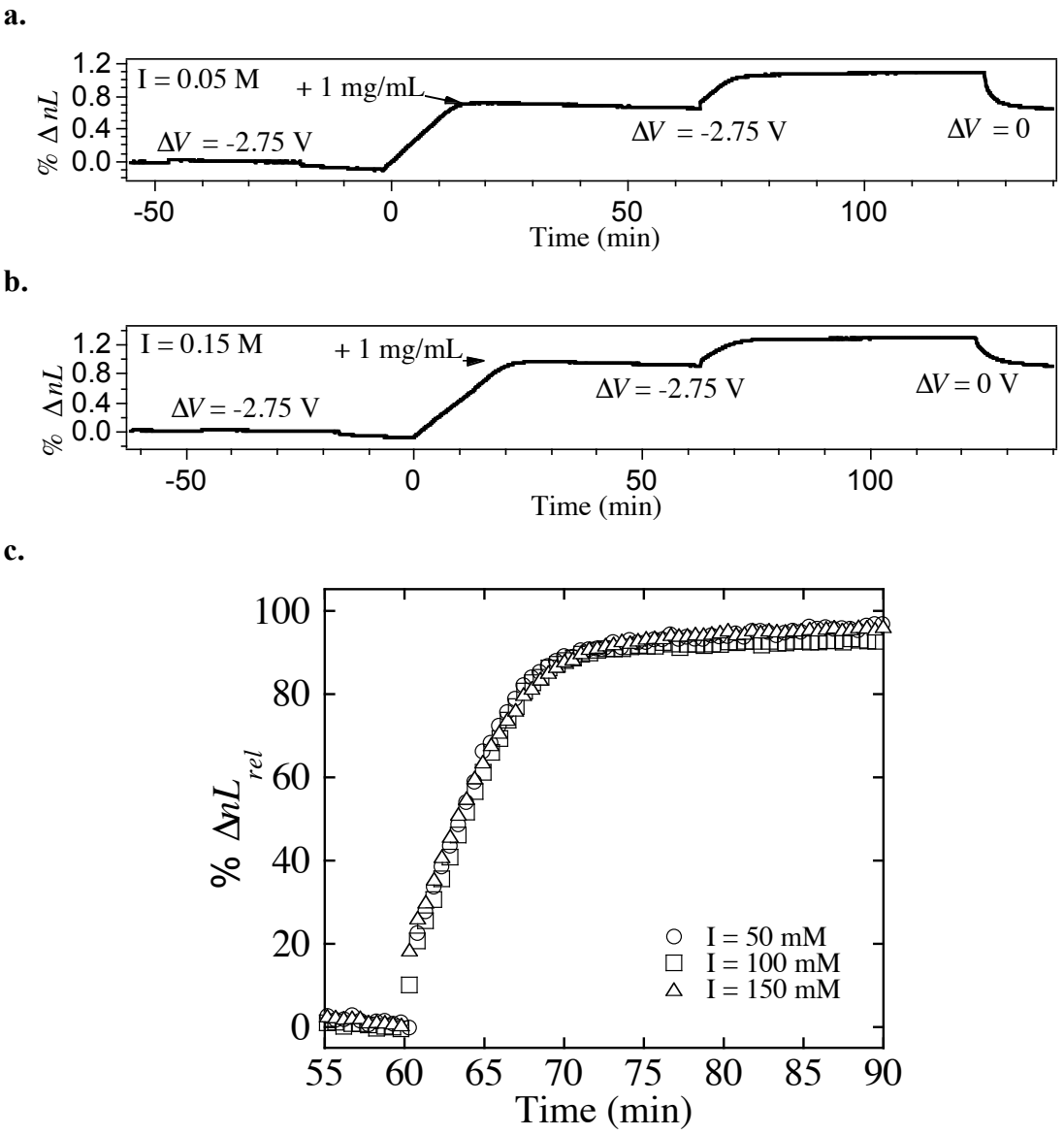

Figure 7.6 Temporal responses of optical pSi-C sensors to lysozyme with applied bias as a function of ionic strength. **a, b,** Optical response of a pSi-C sample after introduction of 1 mg/mL lysozyme at time $t = 0$ with an applied bias of -2.75 V at time ~ 60 min. At time ~ 120 min, bias was returned to 0 V, resulting in a decrease in the optical response. For both experiments, initial baseline was achieved in pH 6.7 buffer with ionic strength = 0.05 M (a) or 0.150 M (b). **c,** temporal response of the film with an applied bias ΔV = -2.75 for the indicated values of ionic strength. For this experiment, the bias ΔV = -2.75 V was applied at time $t = 0$. The y-axis label, $\% \Delta nL_{rel}$, is as defined in Eqn. 7.3 in the text.

7.4.6 Activity of Captured Protein

An important requirement of many bioassay or drug delivery applications is that the collection, concentration, and immobilization processes not denature or otherwise deactivate the biomolecule of interest. While it has been demonstrated that porous Si matrices can release antibodies [222] enzymes [171, 223-229], or other biomolecules [230] in their active form, some compositions of porous Si are known to undergo irreversible chemical reactions with drugs or other molecules [18, 231, 232]. In the present case, the enzymatic activity of lysozyme provides a functional assay of the compatibility of the carbonized pSi opto-electrochemical device with sensitive proteins. The activity of lysozyme collected in and then released from the electrified pSi matrix (ΔV = -2.75 V) was compared to the activity of as-received lysozyme and lysozyme exposed to the pSi matrix at ΔV = 0 V. Activity was quantified using a standard fluorescence-based lysozyme assay using Micrococcus lysodeikticus cells labeled with fluorescein (Figure 7.7). The activity of lysozyme was compared with a control that had not been exposed to the pSi-C film and voltage. **()** shows the detected lysozyme activity after incubation with the substrate for 30 min. Concentration of total collected lysozyme was detemined using a BCA assay prior to lysozyme activity experiments. Pearson correlation coefficient between the control and the sample released from the pSi device is ~ 99 %. In comparison to the control, lysozyme retained ~ 81% of its activity after voltage-induced loading and release of the protein from the pSi opto-electrochemical device.

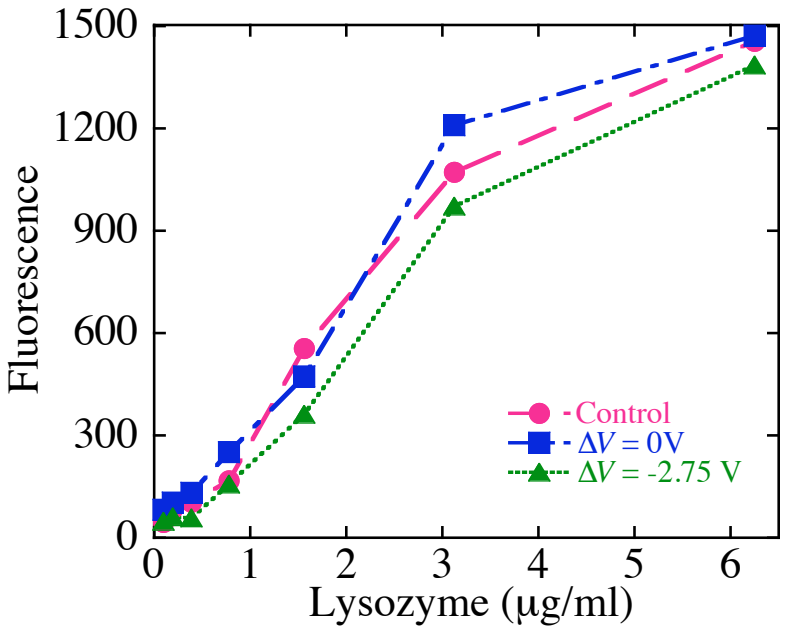

Figure 7.7 Determination of lysozyme activity after interaction with pSi opto-electrochemical device. Lysozyme activity was measured by incubating lysozyme with Micrococcus lysodeikticus cell walls labeled with fluorescein. Fluoresence is quenched in the cell wall, and the action of active lysozyme disrupts the cell walls and releases fluorescein into solution, where its fluorescence recovers. Fluorescence is thus proportional to lysozyme activity. Here, the fluorescence was measured after 30 min of incubation with the lysozyme solution samples. Three different samples are compared: control (as-received), lysozyme that had been exposed to the carbonized porous silicon sample at $\Delta V = 0$V, and lysozyme that had been loaded into pSi at an applied bias of ΔV = -2.75 V for 120 min and then released into free solution. Concentration of lysozyme (x-axis) determined independently by BCA assay. Lysozyme retains ~ 81 % activity after the experiment.

7.5 Conclusions

A unique aspect of the present work is that it demonstrates the first example of a porous interferometric biosensor that utilizes electroadsorption for analyte capture. Whereas electroadsorption is a well-established means to concentrate analytes (including biologicals) on electrode surfaces [211, 233-235], application of the method to label-free optical biosensing has been limited by a lack of transparent porous conductors that are stable in relevant aqueous media. The system demonstrated here was not applicable to negatively charged molecules due to a lack of stability of the carbonized pSi sensor under positive bias conditions, although this is not a fundamental limitation of the carbon electrode [236-239], and more stable carbonization chemistries for porous Si have recently emerged [240] that may be applicable to voltage dependent diffusion and adsorption experiments. A significant advantage of carbonaceous surfaces is their compatibility with biological systems [241-245], which is manifested in the present case in the observed retention of the functional activity of the protein lysozyme.

Chapter seven, in part or in full, is a reprint (with co-author permission) of the material as it appears in the following publication: Chen, M. Y.; Klunk, M.; Diep, V.; Sailor, M.J., Electric Field Assisted Protein Transport, Capture, and Interferometric Sensing in Carbonized Porous Silicon Films. *Advanced Materials*, *accepted.* The author of this dissertation is the primary author of this manuscript.

8 References

1. Lieberzeit, P. A.; Dickert, F. L., Rapid Bioanalysis with Chemical Sensors: Novel Strategies for Devices and Artificial Recognition Membranes. *Anal. Bioanal. Chem.* **2008,** *391*, 1629-1639.

2. Branton, D.; Deamer, D. W.; Marziali, A.; Bayley, H.; Benner, S. A.; Butler, T.; Ventra, M. D.; Garaj, S.; Hibbs, A.; Huang, X.; Jovanovich, S. B.; Krstic, P. S.; Lindsay, S.; Ling, X. S.; Mastrangelo, C. H.; Meller, A.; Oliver, J. S.; Pershin, Y. V.; Ramsey, J. M.; Riehn, R.; Soni, G. V.; Tabard-Cossa, V.; Wanunu, M.; Wiggin, M.; Schloss, J. A., The Potential and Challenges of Nanopore Sequencing. *Nature Nanotech.* **2008,** *26* (10), 1146-1153.

3. Howorka, S.; Siwy, Z., Nanopore analytics: sensing of single molecules. *Chemical Society Reviews* **2009,** *38*, 2360-2384.

4. Abgrall, P.; Nguyen, N. T., Nanofluidic Devices and Their Applications. *Anal. Chem.* **2008,** *80*, 2326-2341.

5. Arrigan, D. W. M., Nanoelectrodes, Nanoelectrode Arrays and Their Applications. *Analyst* **2004,** *129*, 1157-1165.

6. Shi, J.; Votruba, A. R.; Farokhzad, O. C.; Langer, R., Nanotechnology in Drug Delivery and Tissue Engineering: From Discovery to Applications. *Nano Lett.* **2010,** *10* (9), 3223-3230.

7. Wang, J., Nanomaterial-Based Amplified Transduction of Biomolecular Interactions. *Small* **2005,** *1* (11), 1036-1043.

8. West, J. L.; Halas, N. J., Engineered Nanomaterials for Biophotonics Applications: Improving Sensing, Imaging, and Therapeutics. *Annu. Rev. Biomed. Eng.* **2003,** *5*, 285-292.

9. Copper, M. A., Optical Biosensors in Drug Discovery. *Nature Rev.* **2002,** *1*, 515-528.

10. Wilson, G. S.; Gifford, R., Biosensors for Real-Time In Vivo Measurements *Biosen. Bioelec.* **2005,** *20*, 2388-2403.

11. Copper, M. A., Label-Free Screening of Bio-Molecular Interactions. *Anal. Bioanal. Chem.* **2003,** *377*, 834-842.

12. Vo-Dinh, T.; Cullum, B., Biosensors and Biochips: Advances in Biological and Medical Diagnostics. *Fresenius J. Anal. Chem.* **2000,** *366*, 540-551.

13. Hughes, M. P., Strategies for Dielectrophoretic Separation in Laboratory-on-a-Chip Systems. *Electrophoresis* **2002,** *23*, 2569-2582.

14. Andrew, J. S.; Anglin, E. J.; Wu, E. C.; Chen, M. Y.; Cheng, L.; William R, F.; Sailor, M. J., Sustained release of a monoclonal antibody from electrochemically prepared mesoporous silicon oxide. *Adv. Funct. Mater.* **2010,** *20* (23), 4168-4174.

15. Wu, E. C.; Park, J.-H.; Park, J.; Segal, E.; Cunin, F.; Sailor, M. J., Oxidation-Triggered Release of Fluorescent Molecules or Drugs from Mesoporous Si Microparticles. *Acs Nano* **2008,** *2* (11), 2401-2409.

16. Li, X.; John, J. S.; Coffer, J. L.; Chen, Y.; Pinizzotto, R. F.; Newey, J.; Reeves, C.; Canham, L. T., Porosified Silicon Wafer Structures Impregnated With Platinum Anti-Tumor Compounds: Fabrication, Characterization, and Diffusion Studies. *Biomed. Microdev.* **2000,** *2* (4), 265-272.

17. Leong, W. Y.; Loni, A.; Canham, L. T., Electrically enhanced erosion of porous Si material in electrolyte by pH modulation and its application in chronotherapy. *Phy. Stat. Sol. (a)* **2007,** *204* (5), 1486-1490.

18. Salonen, J.; Kaukonen, A. M.; Hirvonen, J.; Lehto, V.-P., Mesoporous Silicon in Drug Delivery Applications. *J. Pharm. Sci.* **2008,** *97* (2), 632-653.

19. Collins, B. E.; Dancil, K.-P.; Abbi, G.; Sailor, M. J., Determining Protein Size using an Electrochemically Machined Pore Gradient in Silicon. *Adv. Funct. Mater.* **2002,** *12* (3), 187-191.

20. Karlsson, L. M.; Tengvall, P.; Lundström, I.; Arwin, H., Penetration and Loading of Human Serum Albumin in Porous Silicon Layers with Different Pore Sizes and Thicknesses. *J. Colloid Interface Sci.* **2003,** *266*, 40-47.

21. Sohn, H.; Lètant, S.; Sailor, M. J.; Trogler, W. C., Detection of Fluorophsphonate *J. Am. Chem. Soc.* **2000,** *122*, 5399-5400.

22. Content, S.; Trogler, W. C.; Sailor, M. J., Detection of Nitrobenzene, DNT and TNT Vapors by Quenching of Porous Silicon Photoluminescence. *Chem. Europ. J.* **2000,** *6*, 2205-2213.

23. Orosco, M. M.; Pacholski, C.; Miskelly, G. M.; Sailor, M. J., Protein-coated Porous Silicon Photonic Crystals for Amplified Optical Detection of Protease Activity. *Adv. Mater.* **2006,** *18*, 1393-1396.

24. Orosco, M. M.; Pacholski, C.; Sailor, M. J., Real-Time Monitoring of Enzyme Activity in a Mesoporous Silicon Double Laye. *Nature Nanotech.* **2009,** *4*, 255-258.

25. Schwartz, M. P.; Alvarez, S. D.; Sailor, M. J., A Porous SiO2 Interferometric Biosensor for Quantitative Determination of Protein Interactions: Binding of Protein A to Immunoglobulins Derived from Different Species. *Anal. Chem.* **2007,** *79*, 327-334.

26. Meade, S. O.; Chen, M. Y.; Sailor, M. J.; Miskelly, G. M., Multiplexed DNA Detection using Spectrally Encoded Porous SiO2 Photonic Crystal Particles. *Anal. Chem.* **2009,** *81* (7), 2618-2625.

27. Striemer, C. C.; Gaborski, T. R.; McGrath, J. L.; Fauchet, P. M., Charge- and Size-based Separation of Macromolecules using Ultrathin Silicon Membranes. *Nature* **2007,** *445* (7129), 749-753.

28. Rong, G.; Weiss, S. M., Biomolecule Size-Dependent Sensitivity of Porous Silicon Sensors. *Phys. Stat. Sol. A-Appl. Mat.* **2009,** *206* (6), 1365-1368.

29. Wen, J.; Arakawa, T.; Philo, J. S., Size-Exclusion Chromatography with On-Lin Light-Scattering, Absorbance, and Refractive Index Detectors for Studing Proteins and Their Interactions. *Anal. Biochem.* **1996,** *240*, 155-166.

30. Barth, H. G.; Boyes, B. E.; Jackson, C., Size Exclusion Chromatography and Related Separation Techniques. *Anal. Chem.* **1998,** *70*, 251R-278R.

31. Wu, R. a.; Hu, L.; Wang, F.; Ye, M.; Zou, H., Recent Development of Monolithic Stationary Phases with Emphasis on Microscale Chromatographic Separation. *J. Chromatogr. A* **2008,** *1184*, 369-392.

32. Shi, J.; Votruba, A. R.; Garokhzad, O. C.; Langer, R., Nanotechnology in Drug Delivery and Tissue Engineering: From Discovery to Applications. *Nano Lett.* **2010,** *10* (9), 3223-3230.

33. Poole, C. F.; Poole, S. K., Foundations of Retention in Partition Chromatography. *J. Chromatogr. A* **2009,** *1216*, 1530-1550.

34. Ahuja, S., *Chromatography and Separation Science*. Academic Press: San Diego, 1990; Vol. 4.

35. Parker, F.; Peterson, N. F., Quantitative Analysis of Phospholipids and Phospholipid Fatty Acids from Silica Gel Thin-Layer Chromatograms. *J. Lip. Res.* **1965,** *6*, 455-460.

36. Sandberg, D. H.; Sjovall, J.; Sjovall, K.; Turner, D. A., Mearsurement of Human Serum Bile Acids by Gas-Lipid Chromatography. *J. Lip. Res.* **1965,** *6*, 182-192.

37. Aviv, H.; Leder, P., Purification of Biologically Active Globin Messenger RNA by Chromatography on Oligothymidylic Acid-Cellulose. *Proc. Nat. Acad. Sci.* **1972,** *69* (6), 1408-1412.

38. Dugo, P.; Cacciola, F.; Kumm, T.; Dugo, G.; Mondello, L., Comprehensive Multidimensional Liquid Chromatography: Theory and Applications. *J. Chromatogr. A* **2008,** *1184*, 353-368.

39. Hjerten, S.; Zhu, M. D., Adaptation of the Equipment for High-Performance Electrophoresis to Isoelectric Focusing. *J. Chromatogr.* **1985,** *346*, 265-270.

40. Cohen, A. S.; Karger, B. L., High-Performance Sodium Dodecyl-Sulfate Polyacrylamide-Gel Capillary Electrophoresis of Peptides and Proteins. *J. Chromatogr.* **1987,** *397*, 409-417.

41. Jorgenson, J. W.; Lukacs, K. D., Zone Electrophoresis in Open-Tubular Glass-Capillaries. *Anal. Chem.* **1981,** *53* (8), 1298-1302.

42. Watzig, H.; Degenhardt, M.; Kunkel, A., Strategies for Capillary Electrophoresis: Method Development and Validation for Pharmaceutical and Biological Applications. *Electrophoresis* **1998,** *19*, 2695-2752.

43. Leon, P. A. A. I.-d.; Zharov, I., Size-Selective Molecular Transport Through Silica Colloidal Nanopores. *Chem. Comm.* **2011,** *47*, 553-555.

44. Liu, S.; Pu, Q.; Gao, L.; Korzeniewski, C.; Matzke, C., From Nanochannel-Induced Proton Conduction Enhancement to a Nanochannel-Based fuel Cell. *Nano Lett.* **2005,** *5* (7), 1389-1393.

45. Miller, S. A.; Young, V. Y.; Martin, C. R., Electroosmotic Flow in Template-Prepared Carbon Nanotube Membranes. *J. Am. Chem. Soc.* **2001,** *123*, 12335-12342.

46. Hou, X.; Guo, W.; Jiang, L., Biomimetic Smart Nanopores and Nanochannels. *Chem. Soc. Rev.* **2011**.

47. Choi, Y.; Baker, L. A.; Hillebrenner, H.; Martin, C. R., Biosensing with Conically Shaped Nanopores and Nanotubes. *Phy. Chem. Chem. Phys.* **2006,** *8*, 4976-4988.

48. Bayley, H.; Cremer, P. S., Stochastic Sensors Inspired by Biology. *Nature* **2001,** *413*, 226-230.

49. Li, J.; Stein, D.; McMullan, C.; Braton, D.; Aziz, M. J.; Golovchenko, J. A., Ion-beam sculpting at nanometre length scales. *Nature* **2001,** *412*, 166-169.

50. Wanunu, M.; Meller, A., Chemically-Modified Solid State Nanopores. *Nano Lett.* **2007,** *7*, 1580-1585.

51. Siwy, Z.; Trofin, L.; Kohli, P.; Baker, L. A.; Trautmann, C.; Martin, C. R., Protein Biosensors based on Biofunctionalized Conical Gold Nanotubes. *J. Am. Chem. Soc.* **2005,** *127* (14), 5000-5001.

52. Han, J.; Fu, J.; Schoch, R. B., Molecular Sieving using Nanofilters: Past, Present, and Future. *Lab Chip* **2008,** *8*, 23-33.

53. Wynia, G. S.; Windhorst, G.; Post, P. C.; Maris, F. A., Development and Validation of a Capillary Electrophoresis Method within a Pharmaceutical Qulity Control Environment and Comparison with High-Performance Liquid Chromatography. *J. Chromatogr. A* **1997,** *773*, 339-350.

54. Görg, A.; Obermaier, C.; Boguth, G.; Harder, A.; Scheibe, B.; Wildgruber, R.; Weiss, W., The Current State of Two-Dimenstional Electrophoresis with Immibilized pH Gradients. *Electrophoresis* **2000,** *21*, 1037-1053.

55. Albrecht, T., A New Look for Nanopore Sensing. *Nature Nanotech.* **2011,** *6*, 195.

56. Fan, X.; White, I. M.; Shopova, S. I.; Zhu, H.; Suter, J. D.; Sun, Y., Sensitive Optical Biosensors for Unlabeled Targets: A Review. *Anal. Chim. Acta.* **2008,** *620*, 8-26.

57. Nakamura, H.; Karube, I., Current research activity in biosensors: review. *Anal Bioanal Chem* **2003,** *377*, 446-468.

58. Nakamura, H.; Karube, I., Current Research Activity in Biosensors: Review. *Anal. Bioanal. Chem.* **2003,** *377*, 446-468.

59. Lechuga, L. M., *Biosensors and Modern Biospecific Analytical Techniques*. Elsevier: 2005.

60. Piehler, J.; Brecht, A.; Gauglitz, G.; Zerlin, M.; Maul, C.; Thiericke, R.; Grabley, S., Label-Free Monitoring of DNA-Ligand Interaction. *Anal. Biochem.* **1997,** *249* (1), 94-102.

61. Piehler, J.; Brandenburg, A.; Brecht, A.; Wagner, E.; Gauglitz, G., Characterization of Grating Couplers for Affinity-based Pesticide Sensing. *App. Opt.* **1997,** *36* (25), 6554-6562.

62. Polzius, R.; DieBel, E.; Bier, F. F.; Bilitewski, U., Real-Time Observation of Affinity Reactions Using Grating Couplers: Determination of the Detection Limit and Calculation of Kinetic Rate Constants. *Anal. Biochem.* **1997,** *248* (2), 269-276.

63. Bernard, A.; Bosshard, H. R., Real-time Monitoring of Antigen-Antibody Recognition on a Metal Oxide Surface by an Optical Grating Coupler Sensor. *Eur. J. Biochem.* **1995,** *230* (2), 416-423.

64. Taylor, A. D.; Yu, Q.; Chen, S.; Homola, J.; Jiang, S., Comparison of E. coli o157: H7 Preparation Methods Used for Detection with Surface Plasmon Resonance Sensor. *Sen. Act. B* **2005,** *107*, 202-208.

65. Nelson, B. P.; Grimsrud, T. E.; Liles, M. R.; Goodman, R. M.; Corn, R. M., Surface Plasmon Resonance Imaging Measuremens of DNA and RNA Hybridization Adsorption onto DNA Microarrays. *Anal. Chem.* **2001,** *73* (1), 1-7.

66. Dahlin, A. B.; Tegengeldt, J. O.; Hook, F., Improving the Instrumental Resolution of Sensor Based on Localized Surface Plamon Resonance. *Anal. Chem.* **2006,** *78* (13), 4416-4423.

67. Henzie, J.; Lee, M. H.; Odom, T. W., Multiscale Patterning of Plamonic Metamaterials. *Nature Nanotech.* **2007,** *2007* (2), 9.

68. Haynes, C. L.; Duyne, R. P. V., Nanosphere Lithography: A Versatile Nanofabrication Too for Stuides of Size-Dependent Nanoparticle Optics. *J. Phy. Chem. B* **2001,** *105* (24), 5599-5611.

69. Fromm, D. P.; Sundaramurthy, A.; Schuck, P. J.; Moerner, W. E., Gap Dependent Optical Coupling of Single Bowtie Nanoantennas Resonant in the Visible. *Nano. Lett.* **2004,** *4* (5), 956-961.

70. Homola, J., Surface Plasmon Resonance Sensors for Detection of Chemical and Biological Species. *Chem. Rev.* **2008,** *108* (2), 462-493.

71. Xu, R. N.; Fan, L.; Reiser, M. J.; El-Shourbagy, T. A., Recent Advances in High-Thoughput Quantitative Bioanalysis by LC-MS/MS. *J. Pharm. Biomed. Anal.* **2007,** *44*, 342-355.

72. Zhang, X.; Guo, Q.; Cui, D., Recent Advances in Nanotechnology Applied to Biosensors. *Senors* **2009,** *9*, 1033-1053.

73. Bukasov, R.; Shumaker-Parry, J. S., Highly Tunable Infrared Extinction Properties of Gold Nanocrescents. *Nano Lett.* **2007,** *7* (5), 1113-1118.

74. Agüí, L.; Yáñez-Sedeño, P.; Pingarrón, J. M., Role of Carbon Nanotubes in Electroanalytical Chemistry: A Review. *Anal. Chim. Acta.* **2008,** *622*, 11-47.

75. Nikitin, P. I.; Vetoshko, P. M.; Ksenevich, T. I., New Type of Biosensor Based on Magnetic Nanoparticle Detection. *J. Mag. and Mag. Mater.* **2007,** *311*, 445-449.

76. Nikitin, M. P.; Zdobnova, T. A.; Lukash, S. V.; Stremovsky, O. A.; Deyev, S. M., Protein-assisted Self-Assumbly Multifunctional Nanoparticles. *Proc. Nat. Acad. Sci.* **2010,** *107*, 5827-5833.

77. Liu, J.; Lee, J. H.; Lu, Y., Quantum Dot Encoding of Aptamer-Linked Nanostructures for One-Pot Simutaneous Detection of Multiple Analytes. *Anal. Chem.* **2007,** *79*, 4120-4125.

78. Cao, Y.-C.; Huang, Z.-L.; Liu, T.-C.; Wang, H.-Q.; Zhu, X.-X.; Wang, Z.; Zhao, Y.-D.; Liu, M.-X.; Luo, Q.-M., Preparation of Silica Encapsulated Quantumm Dot Ecoded Beads for Multiplexed Assay and its Properties. *Anal. Biochem.* **2006,** *351*, 193-200.

79. Canham, L. T., Si Quantum Wire Array Fabrication by Electrochemical and Chemical Dissolution. *Appl. Phys. Lett.* **1990,** *57* (10), 1046-1048.

80. Lehmann, V.; Gosele, U., Porous Silicon Formation: a Quantum Wire Effect. *Appl. Phys. Lett.* **1991,** *58* (8), 856-858.

81. Sohn, J.; Letant, S.; Sailor, M. J.; Trogler, W. C., Detection of Fluorophosphonate Chemical Warefare Agents by Catalytic Hydrolysis with a Porous Silicon Interferometer. *J. Am. Chem. Soc.* **2000,** *122*, 5399-5400.

82. Schmedake, T. A.; Cunin, F.; Link, J. R.; Sailor, M. J., Standoff Detection of Chemicals using Porous Silicon "Smart" Dust Paticles. *Adv. Mater.* **2002,** *14*, 1270-1272.

83. Letant, S. E.; Hart, B. R.; Kane, S. R.; Hadi, M. Z.; Shields, S. J.; Renolds, J. G., Enzyme Immobilization on Porous Silicon Surfaces. *Adv. Mater.* **2004,** *16*, 689-693.

84. Chan, S.; Fauchet, P. M.; Li, Y.; Rothberg, L. J.; Miller, B. L., Porous Silicon Microcavities for Biosensing Applications. *Phy. Stat. Sol. (a)* **2000,** *182*, 541-546.

85. Janshoff, A.; Dancil, K.-P. S.; Steinem, C.; Greiner, D. P.; Lin, V. S.-Y.; Gurtner, C.; Motesharei, K.; Sailor, M. J.; Ghadiri, M. R., Macroporous p-Type Silicon Fabry-Perot Layers. Fabrication, Characterization, and Application in Biosensing. *J. Am. Chem. Soc.* **1998,** *120*, 12108-12116.

86. Sailor, M. J.; Link, J. R., "Smart dust": nanostructured device in a grain of sand. *Chem. Commun.* **2005**, 1375-1383.

87. Canham, L., *Properties of Porous Silicon* Institution of Engineering and Technology: London, 1997; Vol. 18.

88. Zhang, X. G., Morphology and Formation Mechanism of Porous Silicon. *J. Electro. Soc.* **2004,** *151* (1), c69-c80.

89. Buriak, J. M., Organometallic Chemistry on Silicon and Germanium Surfaces. *Chem. Rev.* **2002,** *102* (5), 1271-1308.

90. Meade, S. O.; Yoon, M. S.; Ahn, K. H.; Sailor, M. J., Porous Silicon Photonic Crystals as Encoded Microcarriers. *Adv. Mater.* **2004,** *16*, 1811-1814.

91. Lehmann, V., *Electrochemistry of Silicon: Instrumentation, Science, Materials, and Applications*. Wiley-VCH Verlag GmbH: 2002.

92. Foll, H.; Christopherson, M.; Carstensen, J.; Haase, G., Formation and Application of Porous Siilcon. *Mater. Sci. Eng. R* **2002,** *39*, 93-141.

93. Salior, M. J., Color Me. Sensitive: Amplification and Discrimination in Photonic Silicon Nanostructure. *Acs Nano* **2007,** *1* (4), 248-252.

94. Pacholski, C.; Sartor, M.; Sailor, M. J.; Cunin, F.; Miskelley, G. M., Biosensing using Porous Silicon Double-Layer Interfereometers:Reflective Interferometric Fourier Transform Spectroscopy. *J. Am. Chem. Soc.* **2005,** *127*, 11636-11645.

95. Berger, M. G.; Arens-Fischer, R.; Thoenissen, M.; Krueger, M.; Billat, S.; Lueth, K.; Hilbrich, S.; Theiss, W.; Grosse, P. In *Dielectric Filters Made of Porous Silicon: Advanced Performancce by Oxidation and New Layer Structures*, E-MRS 96 Spring Meeting, Symposium L: New Developments in Porous Silicon: Relation with Other Nanostructure Porous Materials, 1996; pp 237-240.

96. Quyang, H.; Chrostophersen, M.; Viard, R.; Miller, B. L.; Fauchet, P. M., Macroporous Silicon Microcavities for Macromolecule Detection. *Adv. Funct. Mater.* **2005,** *15*, 1851-1859.

97. Meade, S. O.; Sailor, M. J., Microfabrication of Freestanding Porous Silicon Particles Containing Spectral Codes. *Phys. Stat. Sol. - Rap. Res. Lett.* **2007,** *1*, R71-R73.

98. Ruminski, A. M.; Moore, M. M.; Sailor, M. J., Humidity-Compensating Sensor Fot Volatile Organic Compounds using Stacked Porous Silicon Photonic Crystals. *Adv. Funct. Mater.* **2008,** *18*, 3418-3426.

99. Buriak, J. M., Organometallic Chemistry on Silicon and Germanium Surfaces. *Chem. Rev.* **2002,** *102* (5), 1272-1308.

100. Ruminski, A. M.; King, B. H.; Salonen, J.; Snyder, J. L.; Sailor, M. J., Porous Silicon-Based Optical Microsensors for Volative Organic Analytes: Effect of Surface Chemsitry on Stability and Specificity. *Adv. Funct. Mater.* **2010,** *20* (17), 2874-2883.

101. Berger, M. G.; Arens-Fischer, R.; Thoenissen, M.; Krueger, M.; Billat, S.; Lueth, K.; Hilbrich, S.; Theiss, W.; Grosse, P., Dielectric Filters Made of Porous Silicon: Advanced Performancce by Oxidation and New Layer Structures. *Thin Sol. Films* **1997,** *297*, 237-240.

102. Wu, E. C.; Andrew, J. S.; Cheng, L. C.; Freeman, W. R.; Pearson, L.; Sailor, M. J., Real-time Monitoring of Sustained Drug Release using the Optical Properties of Porous Silicon Photonic Crystal Particles. *Biomaterials* **2011,** *32* (7), 1957-1966.

103. Nicewarner-Pena, S. R.; Freeman, R. G.; Reiss, B. D.; He, L.; Pena, D. J.; Walton, I. D.; Cromer, R.; Keating, C. D.; Natan, M. J., Submicrometer Metallic Barcodes. *Science* **2001,** *294*, 137-141.

104. Wilson, R.; Cossins, A. R.; Spiller, D. G., Encoded Microcarriers for High-Throughput Multiplexed Detection. *Angew. Chem. Int. Ed.* **2006,** *45* (37), 6104-6117.

105. Han, M.; Gao, X.; Su, J. Z.; Nie, S., Quantum-dot-tagged Microbeads for Multiplexed Optical Coding of Biomolecles. *Nat. Biotech.* **2001,** *19*, 631-635.

106. Ferguson, J. A.; Steemers, F. J.; Walt, D. R., High-Density Fiber-Optic DNA Random Microsphere Array. *Anal. Chem.* **2000,** *72* (22).

107. Liu, J.; Lee, J. H.; Lu, Y., Quantum Dot Encoding of Aptamer-Linked Nanostructures for One-Pot Simultaneous Detection of Multiple Analytes. *Anal. Chem.* **2007,** *79* (11), 4120-4125.

108. Li, Y. Y.; Kim, P.; Sailor, M. J., Painting a Rainbow on Silicon - A Simple Method to Generate a Porous Silicon Band Filter Gradient. *Phy. Stat. Sol. (a)-Appl. Mat.* **2005,** *202* (8), 1616-1618.

109. Pacholski, C.; Yu, C.; Miskelly, G. M.; Godin, D.; Sailor, M. J., Reflective Interferometric Fourier Transform Spectroscopy: A Self-Compensating Label-Free Immunosensor Using Double-layers of Porous SiO2. *J. Am. Chem. Soc.* **2006,** *128*, 4250-4252.

110. Haimi, E.; Lindroos, V. K.; Nowak, R., A First Step in Prediction of Nanoscale Structure of Porous Silicon From Processing Parameters. *J. Nanosci. Nanotech.* **2001,** *1* (2), 201-206.

111. Gaburro, Z.; Oton, C. J.; Bettotti, P.; Negro, L. D.; Prakash, G. V.; Cassznelli, M.; Pavesi, L., Interferometric Method for Monitoring Electrochemical Etching of THing Films. *J. Electro. Soc.* **2003,** *150* (6), 381-384.

112. Vallet-Regi, M.; Balas, F.; Arcos, D., Mesoporous Materials for Drug Delivery. *Angew. Chem. Int. Ed.* **2007,** *46*, 7548-7558.

113. Song, J. H.; Sailor, M. J., Chemical Modification of Crystalline Porous Silicon Surfaces. *Comments Inorg. Chem.* **1998,** *21* (1-3), 69-84.

114. Buriak, J. M., Organometallic Chemistry on Silicon Surfaces: Formation of Functional Monolayers Bound Through Si-C Bonds. *Chem. Comm.* **1999,** *12*, 1051-1060.

115. Sorokin, L. M.; Grigor'ev, L. V.; Kalmykov, A. E.; Sokolov, V. I., Structural Properties and Current Transport in a Nanocomposite Formed on a Silicon Surface by Oxidation of the Porous Layer. *Phy. Sol. Stat.* **2005,** *47* (7), 1365-1371.

116. Ikegami, T.; Tomomatsu, K.; Takubo, H.; Horie, K.; Tanaka, N., Separation Efficiencies in Hydrophilic Interaction Chomatography. *J. Chromatogr. A* **2008,** *1184*, 474-503.

117. Pacholski, C.; Sartor, M.; Sailor, M. J.; Cunin, F.; Miskelly, G. M., Biosensing Using Porous Silicon Double-Layer Interferometers: Reflective Interferometric Fourier Transform Spectroscopy. *J. Am. Chem. Soc.* **2005,** *127*, 11636-11645.

118. Oillic, C.; Mur, P.; Blanquet, E.; Delapierre, G.; Vinet, F.; Billon, T., DNA Microarrays on Silicon Nanostructures: Optimization of the Multilayer Stack for Fluorescence Detection. *Biosen. Bioelec.* **2006,** *22* (9), 2086-2092.

119. Jarvis, K. L.; Barnes, T. J.; Badalyan, A.; Pendleton, P.; Prestidge, C. A., Impact of Thermal Oxidation on the Adsorptive Properties and Structure of Porous Silicon Particles. *J. Phy. Chem. C* **2008,** *112*, 9717-9722.

120. Gregg, S. J.; Sing, K. S. W., *Adsorption, Surface Area and Porosity*. 2nd ed.; Academic Press Inc.: London, 1982; p 112.

121. Brunauer, S.; Emmett, P. H.; Teller, E., Adsorption of gases in multimolecular layers. *J. Am. Chem. Soc.* **1938,** *60*, 309-319.

122. Broekhof, J. C.; Deboer, J. H., Studies on Pore Systems in Catalysts .9. Calculation of Pore Distributions from Adsorption Branch of Nitrogen Sorption Isotherms in Case of Open Cylindrical Pores .a. Fundamental Equations. *J. Catal.* **1967,** *9* (1), 8.

123. Salem, M. S.; Sailor, M. J.; Sakka, T.; Ogata, Y. H., Electrochemical Preparation of a Rugate Filter in Silicon and its Deviation from the Ideal structure. *J. Appl. Phys.* **2007,** *101*.

124. Pirasteh, P.; Charrier, J.; Soltani, A.; Haesaert, S.; Haji, L.; Godon, C.; Errien, N., The Effect of Oxidation on Phyiscal Properties of Porous Silicon Layers for Optical Applications. *Appl. Surf. Sci.* **2006,** *253*, 1999-2002.

125. Astrova, E. V.; Tolmachev, V. A., Effective refractive index and compositin of oxidized porou silicon films. *Mat. Sci. Eng.* **2000,** *B69-70*, 142-148.

126. Fan, J. B.; Chee, M. S.; Gunderson, K. L., Highly Parallel Genomic Assays. *Nat. Rev. Genet.* **2006,** *7* (8), 632-644.

127. Bruchez, M.; Moronne, M.; Gin, P.; Weiss, S.; Alivisatos, A. P., Semiconductor Nanocrystals as Fluorescent Biological Labels. *Science* **1998,** *281* (5385), 2013-2016.

128. Chan, W. C.; Nie, S., Quantum Dot Bioconjugates for Ultrasensitive Nonisotropic Detection. *Science* **1998,** *281*, 2016-2018.

129. Fenniri, H.; Ding, L.; Ribbe, A. E.; Zyrianov, Y., Barcoded Resins: A New Concept for Polymer-Supported Combinatorial Library Self-Deconvolution. *J. Am. Chem. Soc.* **2001,** *123* (33), 8151-8152.

130. Moon, J. A.; Putnam, M. A.; Perbost, M.; Quinn, J. J.; Trounsine, M. Diffraction Grating-Based Encoded Particles for Multiplexed Experiments. 2005/0227252, 2005.

131. Gunderson, K. L.; Kruglyak, S.; Graige, M. S.; Garcia, F.; Kermani, B. G.; Zhao, C.; Che, D.; Dickinson, T.; Wickham, E.; Bierle, J.; Doucet, D.; Milewski, M.; Yang, R.; Siegmund, C.; Haas, J.; Oliphant, A.; Fan, J.-B.; Barnard, S.; Chee, M. S., Decoding Randomly Ordered DNA Arrays. *Geonme. Res.* **2004,** *14*, 870-877.

132. Zhao, Y.; Zhao, X.; Sun, C.; Zhu, R.; Gu, Z., Encoded Silica Colloidal Crystal Beads as Supports for Potential Multiplex Immunoassay. *Anal. Chem.* **2008,** *80*, 1598-1605.

133. Cunin, F.; Schmedake, T. A.; Link, J. R.; Li, Y. Y.; Koh, J.; Bhatia, S. N.; Sailor, M. J., Biomolecular Screening with Encoded Porous Silicon Phontonic Crystals. *Nature Mater.* **2002,** *1*, 39-41.

134. Steinberg, G.; Stromsborg, K.; Thomas, J.; Barker, D.; Zhao, C., Strategies for Covalent Attachment of DNA to Beads. *Biopolymers* **2004,** *73*, 597-605.

135. Meade, S. O.; Yoon, M. S.; Ahn, K. H.; Sailor, M. J., Porous silicon photonic crystals as encoded microcarriers. *Adv. Mater.* **2004,** *16* (20), 1811-1814.

136. Empedocles, S. A.; Watson, A. R. Two-dimensional spectral imaging system. 6759235, 2004.

137. Cunin, F.; Schmedake, T. A.; Link, J. R.; Li, Y. Y.; Koh, J.; Bhatia, S. N.; Sailor, M. J., Biomolecular screening with encoded porous silicon photonic crystals. *Nature Mater.* **2002,** *1*, 39-41.

138. Mansfield, J. R.; Gossage, K. W.; Hoyt, C. C.; Levenson, R. M., Autofluorescence Removal, Multiplexing, and Automated Analysis Methods for In-Vivo Fluorescence Imaging. *J. Biomed. Opt.* **2005,** *10* (4), 41207-1-41207-9.

139. Moghimi, S. M.; Hunter, A. C.; Murray, J. C., Nanomedicine: Current Status and Future Prospects. *FASEB* **2005,** *19*, 311-330.

140. Moghimi, S. M.; Hunter, A. C.; Murray, J. C., Long-circulating and target specific nanoparticles: theory to practice. *Pharmacol. Rev.* **2001,** *53*, 283-318.

141. Panyam, J.; Labhasetwar, V., Biodegradable Nanoparticles for Drug and Gene Delivery to Cells and Tissues. *Adv. Drug Delivery Rev.* **2003,** *55*, 329-347.

142. Discher, D. E.; Eisenberg, A., Polymer Vesicles. *Science* **2002,** *297*, 967-973.

143. Gill, I.; Ballesteros, A., Bioencapsulaion within synthetic polymers(part 1): sol-gel encapsulated biologicals. *TIBTECH* **2000,** *18*, 282-296.

144. Gregoriadis, G., Engineering Liposomes for Drug Delivery: Progress and Problems. *Trend in Biotech.* **1995,** *13* (12), 527-537.

145. Canham, L. T., Bioactive silicon structure fabrication through nanoetching techniques. *Adv. Mater.* **1995,** *7* (12), 1033-1037.

146. Canham, L. T.; Reeves, C. L.; King, D. O.; Branfield, P. J.; Crabb, J. G.; Ward, M. C. L., Bioactive Polycrytalline Silicon. *Adv. Mater.* **1996,** *8* (10), 850-852.

147. Canham, L. T.; Reeves, C. L.; Loni, A.; Houlton, M. R.; Newey, J. P.; Simons, A. J.; Cox, T. I., Calcium phosphate nucleation on porous silicon: factors influencing kinetics in acellular simulated body fluids. *Thin Sol. Films* **1997,** *297* (1-2), 304-307.

148. Canham, L. T.; Reeves, C. L.; Newey, J. P.; Houlton, M. R.; Cox, T. I.; Buriak, J. M.; Stewart, M. P., Derivatized mesoporous silicon with dramatically improved stability in simulated human blood plasma. *Adv. Mater.* **1999,** *11* (18), 1505-1507.

149. Li, X.; Coffer, J. L.; Chen, Y. D.; Pinizzotto, R. F.; Newey, J.; Canham, L. T., Transition metal complex-doped hydroxyapatite layers on porous silicon. *J. Am. Chem. Soc.* **1998,** *120* (45), 11706-11709.

150. Du, L.; Liao, S.; Khatib, H. A.; Stoddart, J. F.; Zink, J. I., Controlled-Access Hollow Mechanized Silica Nanocontainers. *J. Am. Chem. Soc.* **2009,** *131*, 15136-15142.

151. Gemeinhart, R. A.; Chen, J.; Park, H.; Park, K., *J. Biomater. Sci. Polym. Ed.* **2000,** *11*.

152. Segal, E.; Perelman, L. A.; Cunin, F.; Renzo, F. D.; Devoisselle, J.-M.; Li, Y. Y.; Sailor, M. J., Confinement of Thermoresponsive Hydrogels in Nanostructure Porous Silicon Dioxide Templates. *Adv. Funct. Mater.* **2007,** *17*, 1153-1162.

153. Wu, J.; Sailor, M. J., Chitosan hydrogel-capped porous SiO2 as a pH responsive Nano-valve for triggered release of insulin. *Adv. Funct. Mater.* **2009,** *19*, 733-741.

154. Emami, J.; Hamishehkar, H.; Najafabadi, A. R.; Gilani, K.; Minaiyan, M.; Mahdavi, H.; Nokhodchi, A., A novel approach to prepare insulin loaded poly(lactic-co-glycolic acid) microcapsules and the protein stability study. *J. Pharm. Sci.* **2009,** *98* (5), 1712-1731.

155. Segal, E.; Perelman, L. A.; Cunin, F.; Renzo, F. D.; Devoisselle, J.-M.; Li, Y. Y.; Sailor, M. J., Confinement of Thermoresponsive Hydrogels in Nanostructured Porous Silicon Dioxide Templates. *Adv. Funct. Mater.* **2007,** *17*, 1153–1162.

156. Giger, K.; Vanam, R. P.; Seyrek, E.; Dubin, P. J., Supression of insulin aggregation by heparin. *Biomacromolecules* **2008,** *9*, 2338-2344.

157. Jiang, G.; Qiu, W.; DeLuca, P. P., Preparation and in Vitro/inVivo Evaluation of Insulin-Loaded Poly(Acryloyl-Hydroxyethyl Starch)-PLGA Composite Microspheres. *Pharma. Res.* **2003,** *20* (3), 452-459.

158. Sluzky, V.; Tamada, J. A.; Klibanov, A. M.; Langer, R., Kinetic of insulin aggregation in aqueous solution upon agitation in the presence of hydrophobic surfaces. *Proc. Natl. Acad. Sci.* **1991,** *88*, 9377-9381.

159. Sluzky, V.; Klibanov, A. M.; Langer, R., Mechanism of insulin aggregation and stabilization in agitated aqueous solutions. *Biotech. Bioeng.* **1992,** *40*, 895-903.

160. Coffer, J. L.; Montchamp, J. L.; Aimone, J. B.; Weis, R. P., Routes to calcifled porous silicon: implications for drug delivery and biosensing. *Phys. Status Solidi A-Appl. Res.* **2003,** *197* (2), 336-339.

161. Tasciotti, E.; Liu, X.; Bhavane, R.; Plant, K.; Leonard, A. D.; Price, B. K.; Cheng, M. M.; Decuzzi, P.; Tour, J. M.; Robertson, F.; Ferrari, M., Mesoporous Silicon Particles as a Multistage Delivery System for Imaging and Therapeutic Applications. *Nat. Nanotech.* **2008,** *3*, 151-157.

162. Segal, E.; Perelman, L. A.; Cunin, F.; Renzo, F. D.; Devoisselle, J.-M.; Li, Y. Y.; Sailor, M. J., Confinement of thermoresponsive hydrogels in nanostructured porous silicon dioxide templates. *Adv. Funct. Mater.* **2007,** *17*, 1153-1162.

163. Parks, G. A., Isoelectric points of solid oxides, solide hydroxides, and aqueous hydroxo complex systems. *Chem. Rev.* **1965,** *65* (2), 177-198.

164. Deen, W. M., Hindered transport of large molecules in liquid-filled pores. *AIChE* **1987,** *33* (9), 1409-1425.

165. Song, S. H.; McIntyre, S. S.; Shah, H.; Veldhuis, J. D.; Hayes, P. C.; Butler, P. C., Direct measurement of pulsatile insulin secretion from the portal vein in human subjects. *J. Clin. Endocrinol. Metab.* **2000,** *85*, 4491-4499.

166. Saleh, O. A.; Sohn, L. L., An Artificial Nanopore for Molecular Sensing. *Nano Letters* **2003,** *3* (1), 37-38.

167. Basore, J. R.; Lavrik, N. V.; Baker, L. A., Single-Pore Membranes Gated by Microelectromagnetic Traps. *Adv. Mater.* **2010**, 1-5.

168. Tokarev, I.; Minko, S., Stimuli-Responsive porous hydrogels at interfaces for molecular filtration, separation, controlled release, and gating in capsules and membranes. *Adv. Mater.* **2010**, 1-17.

169. Schoch, R. B.; Bertsch, A.; Renaud, P., pH-Controlled Diffusion of Proteins with Different pI Values Across a Nanochannel on a Chip. *Nano Lett.* **2006,** *6* (3), 543-547.

170. Lin, V. S.-Y.; Motesharei, K.; Dancil, K. S.; Sailor, M. J.; Ghadiri, M. R., A Porous Silicon-Based Optical Interferometric Biosensor. *Science* **1997,** *278* (5339), 840-843.

171. Orosco, M. M.; Pacholski, C.; Sailor, M. J., Real-time Monitoring of Enzyme Activity in a Mesoporous Silicon Double Layer. *Nature Nanotech.* **2009,** *4*, 255 - 258.

172. Kosmulski, M., Surface Charge and Zeta Potential of Silica in Mixtures of Organic Solvents and Water. In *Adsorption on Silica Surfaces*, Papirer, E., Ed. Marcel Dekker: New York, 2000; Vol. 90, pp 363-364.

173. Yu, S.; Lee, S. B.; Martin, C. R., Electrophoretic protein transport in gold nanotube membranes. *Anal. Chem.* **2003,** *75* (6), 1239-1244.

174. Ku, J.-R.; Stroeve, P., Protein Diffusion in Charged Nanotubes: On-off Behavior of Molecular Transport. *Langmuir* **2004,** *20* (5), 2030-2032.

175. Janshoff, A.; Dancil, K.-P. S.; Steinem, C.; Greiner, D. P.; Lin, V. S.-Y.; Gurtner, C.; Motesharei, K.; Sailor, M. J.; Ghadiri, M. R., Macroporous p-type silicon Fabry-Perot layers. Fabrication, characterization, and applications in biosensing. *J. Am. Chem. Soc.* **1998,** *120* (46), 12108-12116.

176. Schwartz, M. P.; Yu, C.; Alvarez, S. D.; Migliori, G.; Godin, D.; Lin, C.; Sailor, M. J., Using an Oxidized Porous Silicon Interferometer for Determining of Relative Protein Binding Affinity through Non-Covalent Capture Probe Immobilization. *Phy. Stat. Sol. (a)* **2007,** *5*, 1444-1448.

177. Parks, G. A., Isoelectric Points of Solid Oxides Solid Hydroxides and Aqueous Hydroxo Complex Systems. *Chem. Rev.* **1965,** *65*, 177-198.

178. Perelman, L. A.; Pacholski, C.; Li, Y. Y.; VanNieuwenzhe, M. S.; Sailor, M. J., pH-Triggered Release of Vancomycin from Protein-Capped Porous Silicon Films. *Nanomedicine* **2008,** *3* (1), 31-43.

179. Tay, L.; Rowell, N. L.; Poitras, D.; Fraser, J. W.; Lockwood, D. J.; Boukherroub, R., Bovine Serum Albumin Adsorption on Passivated Porous Silicon Layers. *Canadian Journal of Chemistry-Revue Canadienne De Chimie* **2004,** *82* (10), 1545-1553.

180. Gaspari, M.; Cheng, M. M. C.; Terracciano, R.; Liu, X. W.; Nijdam, A. J.; Vaccari, L.; di Fabrizio, E.; Petricoin, E. F.; Liotta, L. A.; Cuda, G.; Venuta, S.; Ferrari, M., Nanoporous Surfaces as Harvesting Agents for Mass Spectrometric Analysis of Peptides in Human Plasma. *J. Proteome Res.* **2006,** *5* (5), 1261-1266.

181. Terracciano, R.; Gaspari, M.; Testa, F.; Pasqua, L.; Tagliaferri, P.; Cheng, M. M. C.; Nijdam, A. J.; Petricoin, E. F.; Liotta, L. A.; Cuda, G.; Ferrari, M.; Venuta, S., Selective Binding and Enrichment for Low-Molecular Weight Biomarker Molecules in

Human Plasma after Exposure to Nanoporous Silica Particles. *Proteomics* **2006,** *6* (11), 3243-3250.

182. Squire, P. G.; Moser, P.; Okonski, C. T., Hydrodynamic Properties of Bovine Serum Albumin Monomer and Dimer. *Biochem.* **1968,** *7* (12), 4261-4272.

183. Radola, B. J., Isoelectric Focusing in Layers of Granulated Gels.1. Thin-Layer Isoelectric Focusing of Proteins. *Biochim. Biophys. Acta* **1973,** *295*, 412-428.

184. Fermi, G.; Perutz, M. F.; Shaanan, B.; Fourme, R., The Crystal Structure of Human Deoxyhaemoglobin at 1.74 A Resolution. *J. Mol. Biol.* **1984,** *175*, 159-174.

185. Conway-Jacobs, A.; Lewin, L. M., Isoelectric Focusing in Acrylamide Gels - Use of Amphoteric Dyes as Internal Markers for Determination of Isoelectric Points. *Anal. Biochem.* **1971,** *43* (2), 394-400.

186. Kendrew, J. C.; Bodo, G.; Dintzis, H. M.; Parrish, R. G.; Wyckoff, H.; Phillips, D. C., A Three-Dimensional Model of the Myoglobin Molecules Obtained by X-ray Analysis. *Nature* **1958,** *181*, 662-666.

187. Vesterberg, O.; Svensson, H., Isoelectric Fractionation, Analysis, and Characterization of Ampholytes in Natural pH Gradients. *Acta Chem. Scand.* **1966,** *20* (3), 820-834.

188. Heller, M. J., DNA Microarray Technology: Devices, Systems, and Applications. *Annu. Rev. Biomed. Eng.* **2002,** *4*, 129-153.

189. Zhu, H.; Bilgin, M.; Snyder, M., Proteomics. *Annu. Rev. Biochem.* **2003,** *72*, 783-812.

190. Barnes, D. W.; Mousetis, L.; Amos, B.; Silnutzer, J., Glass-Bead Affinity Chromatography of Cell Attachment and Spreading-Promoting Factors of Human Serum. *Anal. Biochem.* **1984,** *137*, 196-204.

191. Pacholski, C.; Perelman, L. A.; VanNieuwenhze, M. S.; Sailor, M. J., Small Molecule Detection by Reflective Interferometric Fourier TransformSpectroscopy (RIFTS). *Phys. Status Sol. A* **2009,** *206* (6), 1318-1321.

192. Drysdale, J. W.; Righetti, P.; Bun, H. F., The Separation of Human and Animal Hemoglobins by Isoelectric Focusing in Polyacrylamide Gel. *BiochiA. Biophys. Acta* **1971,** *229*, 42-50.

193. Dancil, K.-P. S.; Greiner, D. P.; Sailor, M. J., A porous silicon optical biosensor: detection of reversible binding of IgG to a protein A-modified surface. *J. Am. Chem. Soc.* **1999,** *121* (34), 7925-7930.

194. Bird, R. B.; Stewart, W. E.; Lightfoot, E. N., *Transport Phenomena*. 2 ed.; John Wiley and Sons: 2002.

195. Crank, J., *The Mathematics of Diffusion*. 2 ed.; Oxford University Press: Clarendon, 1975.

196. Gaigalas, A. K.; Hubbard, J. B.; McCurley, M.; Woo, S., Diffusion of Bovine Serum Albumin in Aqueous Solutions. *J. Phys. Chem.* **1992,** *96*, 2355-2359.

197. Chen, W.; Wu, Z.-Q.; Xia, X.-H.; Xu, J.-J.; Chen, H.-Y., Anomalous Diffusion of Electrically Neutral Molecules in Charged Nanochannels. *Angew. Chem. Int. Ed.* **2010,** *49*, 7943-7947.

198. Jiang, X.; Mishra, N.; Turner, J. N.; Spencer, M. G., Diffusivity of Sub-1,000 Da Molecules in 40 nm Silicon-Based Alumina Pores. *Micro. Nanoflu.* **2008,** *5*, 695-701.

199. Johnson, E. M.; Berk, D. A.; Jain, R. K.; Deen, W. M., Hindered Diffusion in Agarose Gels: Test of Effective Medium Model. *Biophys. J.* **1996,** *70*, 1017-1026.

200. Hellriegel, C.; Kirstein, J.; Brauchle, C.; Latour, V.; Pigot, T.; Olivier, R.; Lacombe, S.; Brown, R.; Guieu, V.; Payrastre, C.; Izquierdo, A.; Mocho, P., Diffusion of Single Streptocyanine Molecules in the Nanoporous Network of Sol-Gel Glasses. *J. Phys. Chem. B* **2004,** *108*, 14699-14709.

201. Yang, Z.; Galloway, J. A.; Yu, H., Protein Interactions with Poly(ethylene glycol) Self-Assembled Monolayers on Glass Substrates: Diffusion and Adsorption. *Langmuir* **1999,** *15*, 8405-8411.

202. Baker, N. A.; Joseph, S.; Holst, M. J.; McCammon, J. A., Electrostatic of Nanosystems: Application to Microtubules and the Ribosome. *Proc. Natl. Acad. Sci.* **2001,** *98* (18), 10037-10041.

203. Ouyang, H.; Christophersen, M.; Viard, R.; Miller, B. L.; Fauchet, P. M., Macroporous Silicon Microcavities for Macromolecule Detection. *Adv. Funct. Mater.* **2005,** *15*, 1851-1859.

204. Hohenester, E.; Mauer, P.; Timpl, R., Crystal Structure of a Pair of Follistatin-Like and EF-hand Calcium-Binding Domains in BM-40. *Embo. J.* **1997,** *16*, 3778-3786.

205. Israelachvili, J. N., *Intermolecular and Surface Forces*. 2nd ed.; Academic Press: London, 1991.

206. Gurtner, C.; Edman, C. F.; Formosa, R. E.; Heller, M. J., Photoelectrophoretic Transport and Hybridization of DNA Oligonucleotides on Unpatterned Silicon Substrates. *J. Am. Chem. Soc.* **2000,** *122* (36), 8589-8594.

207. Wanunu, M.; Meller, A., Chemically-modified solid state nanopores. *Nano. Lett.* **2007,** *7* (1580-1585).

208. Choi, Y.; Baker, L. A.; Hillebrenner, H.; Martin, C. R., Biosensing with conically shaped nanopores and nanotubes. *Phys. Chem. Chem. Phys.* **2006,** *8*, 4976-4988.

209. Han, J.; Fu, J.; Schoch, R. B., Molecular sieving using nanofilters: past, present and future. *Lab Chip* **2008,** *8*, 23-33.

210. Bard, A. J.; Faulkner, L. R., *Electrochemical Methods: Fundamentals and Applications*. John Wiley & Sons: New York, 1980; p 501-516.

211. Wandlowski, T.; Lampner, D.; Lindsay, S. M., Structure and stability of cytosine adlayers on Au(111): An in-situ STM study. *J. Electroanal. Chem.* **1996,** *404* (2), 215-226.

212. Rothena, A.; Mathota, C., Immunoelectroadsorption: The fundamentals of the immunoelectroadsorption method. *Immunochemistry* **1969,** *6* (2), 241-251.

213. Bjorklund, R. B.; Arwin, H.; Johansson, I.; Skoeld, R., Ellipsometric and reflectance study of electroadsorption from a water-based metalworking fluid onto gold surfaces. *Langmuir* **1992,** *8* (2), 571–576.

214. Brown, G. M.; Ferrell, T. L.; Thundat, T. G. Photoelectrochemical molecular comb. U.S. Patent #7,090,757, August 15, 2006, 2006.

215. Pacholski, C.; Sartor, M.; Sailor, M. J.; Cunin, F.; Miskelly, G. M., Biosensing using porous silicon double-layer interferometers: reflective interferometric Fourier transform spectroscopy. *J. Am. Chem. Soc.* **2005,** *127* (33), 11636-11645.

216. Sailor, M. J., Color Me Sensitive: Amplification and Discrimination in Photonic Silicon Nanostructures. *ACS Nano* **2007,** *1* (4), 248-252.

217. Salonen, J.; Bjorkqvist, M.; Laine, E.; Niinisto, L., Stabilization of porous silicon surface by thermal decomposition of acetylene. *Appl. Surf. Sci.* **2004,** *225* (1-4), 389-394.

218. Sciacca, B.; Alvarez, S. D.; Geobaldo, F.; Sailor, M. J., Bioconjugate functionalization of thermally carbonized porous silicon using a radical coupling reaction. *Dalton Trans.* **2010,** *39*, 10847-10853.

219. Wetter, L. R.; Deutsch, H. F., Immunological studies on egg white proteins: IV. immunochemical and physcial studies of lysozyme. *J. Biol. Chem.* **1951,** *192*, 237-242.

220. White, E. T.; Tan, W. H.; Ang, J. M.; Tait, S.; Litster, J. D., The density of a protein crystal. *Powd. Tech.* **2007,** *179*, 55-58.

221. Jones, F. T., Optical and crystallographic properties of lysozyme choloride. *J. Am. Chem. Soc.* **1946,** *68* (5), 854-857.

222. Andrew, J. S.; Anglin, E. J.; Wu, E. C.; Chen, M. Y.; Cheng, L.; Freeman, W. R.; Sailor, M. J., Sustained Release of a Monoclonal Antibody from Electrochemically Prepared Mesoporous Silicon Oxide. *Adv. Funct. Mater.* **2010,** *20*, 4168–4174.

223. Maia, M. D. D.; de Vasconcelos, E. A.; Maia, P.; Maciel, J. D.; Cajueiro, K. R. R.; da Silva, M. D.; da Silva, E. F.; Dutra, R. A. F.; Freire, V. N.; de Lima, J. L., Immobilization of urease on vapour phase stain etched porous silicon. *Process Biochem.* **2007,** *42* (3), 429-433.

224. Kilian, K. A.; Böcking, T.; Gaus, K.; Gal, M.; Gooding, J. J., Peptide-Modified Optical Filters for Detecting Protease Activity. *ACS Nano* **2007,** *1* (4), 355-361.

225. Thomas, J. C.; Pacholski, C.; Sailor, M. J., Delivery of Nanogram Payloads Using Magnetic Porous Silicon Microcarriers. *Lab Chip* **2006,** *6* (6), 782 - 787.

226. DeLouise, L. A.; Miller, B. L., Enzyme immobilization in porous silicon: quantitative analysis of the kinetic parameters for glutathione-S-transferases. *Anal. Chem.* **2005,** *77*, 1950-1956.

227. DeLouise, L. A.; Kou, P. M.; Miller, B. L., Cross-Correlation of Optical Microcavity Biosensor Response with Immobilized Enzyme Activity. Insights into Biosensor Sensitivity. *Anal. Chem.* **2005,** *77* (10), 3222-3230.

228. Létant, S. E.; Hart, B. R.; Kane, S. R.; Hadi, M. Z.; Shields, S. J.; Reynolds, J. G., Enzyme immobilization on porous silicon surfaces. *Adv. Mater.* **2004,** *16* (8), 689-693.

229. DeLouise, L. A.; Miller, B. L., Quantatitive assessment of enzyme immobilization capacity in porous silicon. *Anal. Chem.* **2004,** *76* (23), 6915-6920.

230. Wu, E. C.; Andrew, J. S.; Cheng, L.; Freeman, W. R.; Pearson, L.; Sailor, M. J., Real-time Monitoring of Sustained Drug Release using the Optical Properties of Porous Silicon Photonic Crystal Particles. *Biomaterials* **2011,** *32*, 1957-1966.

231. Laaksonen, T.; Santos, H.; Vihola, H.; Salonen, J.; Riikonen, J.; Heikkila, T.; Peltonen, L.; Kumar, N.; Murzin, D. Y.; Lehto, V.-P.; Hirvonen, J., Failure of MTT as a Toxicity Testing Agent for Mesoporous Silicon Microparticles. *Chem. Res. Toxicol.* **2007,** *20* (12), 1913-1918.

232. Wu, E. C.; Andrew, J. S.; Buyanin, A.; Kinsella, J. M.; Sailor, M. J., Suitability of porous silicon microparticles for the long-term delivery of redox-active therapeutics. *Chem. Commun.* **2011,** *in press: DOI: 10.1039/c1cc10993f.*

233. Ban, A.; Schafer, A.; Wendt, H., Fundamentals of electrosorption on activated carbon for wastewater treatment of industrial effluents. *J. Appl. Electrochem.* **1998,** *28* (3), 227-236.

234. Koresh, J.; Soffer, A., Stereoselectivity in Ion Electroadsorption and in Double-Layer Charging of Molecular-Sieve Carbon Electrodes. *J. Electroanal. Chem.* **1983,** *147* (1-2), 223-234.

235. Salitra, G.; Soffer, A.; Eliad, L.; Cohen, Y.; Aurbach, D., Carbon electrodes for double-layer capacitors - I. Relations between ion and pore dimensions. *J. Electrochem. Soc.* **2000,** *147* (7), 2486-2493.

236. Feng, J. J.; Xu, J. J.; Chen, H. Y., Direct electron transfer and electrocatalysis of hemoglobin adsorbed on mesoporous carbon through layer-by-layer assembly. *Biosens. Bioelectron.* **2007,** *22* (8), 1618-1624.

237. Liu, G. Z.; Gooding, J. J., An interface comprising molecular wires and poly(ethylene glycol) spacer units self-assembled on carbon electrodes for studies of protein electrochemistry. *Langmuir* **2006,** *22* (17), 7421-7430.

238. Wisniewski, N.; Reichert, M., Methods for reducing biosensor membrane biofouling. *Colloid Surf. B-Biointerfaces* **2000,** *18* (3-4), 197-219.

239. Liu, J. Y.; Cheng, L.; Li, B. F.; Dong, S. J., Covalent modification of a glassy carbon surface by 4-aminobenzoic acid and its application in fabrication of a polyoxometalates-consisting monolayer and multilayer films. *Langmuir* **2000,** *16* (19), 7471-7476.

240. Kelly, T. L.; Gao, T.; Sailor, M. J., Carbon and Carbon/Silicon Composites Templated in Microporous Silicon Rugate Filters for the Adsorption and Detection of Organic Vapors. *Adv. Mater.* **2011,** *on line* (DOI: 10.1002/adma.201004142).

241. Wightman, R. M., Probing cellular chemistry in biological systems with microelectrodes. *Science* **2006,** *311* (5767), 1570-1574.

242. Maehashi, K.; Katsura, T.; Kerman, K.; Takamura, Y.; Matsumoto, K.; Tamiya, E., Label-free protein biosensor based on aptamer-modified carbon nanotube field-effect transistors. *Anal. Chem.* **2007,** *79* (2), 782-787.

243. Hrapovic, S.; Liu, Y. L.; Male, K. B.; Luong, J. H. T., Electrochemical biosensing platforms using platinum nanoparticles and carbon nanotubes. *Anal. Chem.* **2004,** *76* (4), 1083-1088.

244. Sotiropoulou, S.; Chaniotakis, N. A., Carbon nanotube array-based biosensor. *Anal. Bioanal. Chem.* **2003,** *375* (1), 103-105.

245. Liu, S. Q.; Ju, H. X., Reagentless glucose biosensor based on direct electron transfer of glucose oxidase immobilized on colloidal gold modified carbon paste electrode. *Biosens. Bioelectron.* **2003,** *19* (3), 177-183.